Investigating applications of Protein Charge Transfer Spectra (ProCharTS) in peptides and proteins

A Thesis Submitted in Partial Fulfillment of the

Requirements for the Degree of

Doctor of Philosophy

By

Alka Singh

Roll No. 176106023

Department of Biosciences and Bioengineering
Indian Institute of Technology Guwahati
Guwahati, Assam- 781039, India

August 2025

INDIAN INSTITUTE OF TECHNOLOGY

GUWAHATI, Assam, India

Department of Biosciences and Bioengineering

STATEMENT

I do hereby declare that the matter embodied in this thesis is the result of investigations carried out by me in the Department of Biosciences and Bioengineering, Indian Institute of Technology Guwahati, India, under the guidance of Prof. Rajaram Swaminathan.

In keeping with the general practice of reporting scientific observations, due acknowledgements have been made wherever the work described is based on the findings of other investigators.

Alka Singh

IIT Guwahati — Alka Singh

August, 2025

INDIAN INSTITUTE OF TECHNOLOGY

GUWAHATI, Assam, India

Department of Biosciences and Bioengineering

CERTIFICATE

It is certified that the work described in this thesis, entitled "***Investigating applications of Protein Charge Transfer Spectra (ProCharTS) in peptides and proteins",*** done by **Alka Singh** for the award of the degree of Doctor of Philosophy is an authentic record of the results obtained from the research work carried out under my supervision in the Department of Biosciences and Bioengineering, Indian Institute of Technology Guwahati, India, and this work has not been submitted elsewhere for a degree.

IIT Guwahati
August, 2025

Prof. Rajaram Swaminathan
Department of BSBE
IIT Guwahati

Dedicated to my Family

Acknowledgements

I am extremely delighted to be in this position in my life after all the hard work and sacrifices. I have put through in the eight years of my Ph.D. life at IIT Guwahati. I don't think I would have made it possible without the help of the people mentioned hereafter, and thus, I would like to express my sincere gratitude to all of them.

First and foremost, I want to express my deepest respect and sincere gratitude to my supervisor Prof. R. Swaminathan for giving me the opportunity to undertake Ph.D. in his research group and for having faith in me. His constant moral support, enthusiasm in research, and motivation during the tough times helped me immensely. I would like to thank him for his scientific insights into the domain of work related to this thesis. He has been a great mentor who encouraged me never to be afraid to try new research ideas, bring the best out of me, and make me a better researcher. I am indebted to him for guiding me in the right direction whenever I needed it the most.

I would also like to extend my sincere gratitude to the Doctoral Committee members, Dr. Rajkumar P. Thummer, Dr. Naveen Gupta and Prof Lal Mohan Kundu, for their encouragement, critical assessment of my Ph.D. work and valuable suggestions, which helped me a lot to troubleshoot the problems I had to face in my Ph.D. Besides my Doctoral Committee, I am extremely grateful to Prof. Bhubaneswar Mandal and his student, Altaf Hussain Kawa for helping me out in circular dichroism spectroscopy used in my PhD work.

I thank the past and present HODs of the Department of Biosciences and Bioengineering (BSBE), Prof. Latha Rangan, Prof Rakhi Chaturvedi, and Prof. Utpal Bora for their valuable support.

I would like to thank Dr. Vinay K. Nandicoori from National Institute of Immunology Delhi, and Prof. Mireille M. A. E. Claessens, University of Twente, The Netherlands for providing the ERK2 and alpha synuclein plasmid constructs, respectively.

My sincere thanks to the BSBE department for letting me use the DCIF facilities, and the staff members for being highly cooperative. Thanks to Central Instruments Facility for letting me use Mass spectrometry (MALDI). I would even like to thank North East Centre for Biological Sciences and Healthcare Engineering (NECBH) for letting me use UV-Vis Spectrophotometer. Thanks to IIT Guwahati for all the facilities and the Ministry of Human Resource Development (MHRD), India, for the financial support.

Thanks to Subansiri Hostel administration and staff members, as the hostel life will hold a special place in my heart.

Next, I wish to express my sincere thanks to my lab seniors Dr. Saumya Prasad, Dr. Shrutidhara Biswas, Dr. Mohd. Ziauddin Ansari, Dr. Amrendra Kumar, Dr. Dileep Ahari, Dr. Anurag Priyardarshi, Dr. Sanjana, Dr Shah Ekramul Alom and Dr. Heeramoni for their enormous help and suggestion during my Ph.D. I would like to express my deep sense of gratitude to all my juniors Subhajit, Abheek, Harikrishna, Simangka, Nuzelu, Himanshi, Rashmi, Sahil, Kartik, Naveen, Sakshi, Chetan, Koustav, Rasanpreet and Bhagirathi.

I would especially like to thank my friends Satakshi, Pragya, Ekramul, Abheek, Darshana, Swati, Nayan, Heeramoni, Arman, Alok and Prateek for making my stay at IIT Guwahati a memorable one. I would even like to thank my off-campus friends Priya, Raksha, Nishtha, and Yogesh for making the PhD journey even more smooth.

My Ph.D. endeavour could not have been completed without the never-ending love and endless support from my family. I would like to express my deepest gratitude to my family for their unwavering support throughout this PhD journey. To my beloved grandfather, whose wisdom and quiet strength have always inspired me, your legacy of perseverance lives on in everything I do. I am grateful to my late grandmother for her unending love and emotional support since my childhood. I would like to thank my parents, who have sacrificed their happiness for me and motivated me in every stage of my life. Your support made a significant difference, and I am sincerely grateful for your role in helping me reach this milestone. I would also like to extend my heartfelt thanks to my in-laws, whose understanding, encouragement, and kindness have meant so much to me. To my sister-in-law, Ankita, for being there in all the challenging situations.

To my brother, Anurag and sister-in- law, Sunidhi, thank you for always believing in me and reminding me to keep pushing forward, even during the most challenging times. Thank you to my little nephew, Aryaveer who brought so much happiness into our lives.

To my best friend, Pranjali, thank you for being my anchor through the highs and lows. Your friendship, late-night pep talks, and unwavering belief in me kept me grounded and reminded me of who I am beyond the academic world. I am incredibly lucky to have you in my life.

Although it is not possible to pen down the names of each individual people, I would like to thank each one of them for helping me and having trust in me

Finally, my deepest thanks to my husband, Maj Shrawan Kumar Pandey, who has been the most important person in my life in helping me get to this point. His constant support, motivation and help during every difficult phase of my life is overwhelming and cannot be expressed in a few words. His unconditional love has been a constant source of motivation throughout my entire life. He has truly been the best friend and the most valued person in my life.

Last but not the least, I am thankful to Almighty God for his continuous blessing.

Alka Singh *August 2025*

List of Abbreviations

ANS	8-Anilinonaphthalene-1-sulfonic acid
ThT	Thioflavin T
CD	Circular Dichroism
ProCharTS	Protein Charge Transfer Spectra
DTT	1,4-Dithiothreitol
SDS-PAGE	Sodium dodecyl sulfate-polyacrylamide gel electrophoresis
TFA	Trifluoroacetic acid
UV-Vis	Ultraviolet-Visible
MALDI	Matrix-assisted laser desorption ionization
CT	Charge Transfer
ET	Electron Transfer
E. Coli	Escherichia Coli
SEC	Size Exclusion Chromatography
IPTG	Isopropyl β-D-1-thiogalactopyranoside
FRET	Förster Resonance Energy Transfer
GdnHCl	Guanidine Hydrochloride
SEC	Size Exclusion Chromatography
DLS	Dynamic Light Scattering
AFM	Atomic Force Microscopy
Ni-NTA	Nickel-Nitrilotriacetic Acid
PBS	Phosphate Buffered Saline

List of Figures:

Thesis Abstract

Spectroscopic methods, including electronic absorption and fluorescence, are essential tools for exploring protein structures and their functional dynamics. Traditionally, these techniques have focused on intrinsic chromophores such as aromatic amino acids like tryptophan (Trp), tyrosine (Tyr), and phenylalanine (Phe) which naturally absorb and emit light in the UV-Visible spectrum. These residues provide insights into the protein's local environment and conformational changes. However, the introduction of extrinsic fluorescent probes, while useful, can sometimes perturb the native structure of proteins, prompting a shift towards label-free, intrinsic alternatives.

Recent research has unveiled that proteins devoid of aromatic residues can still exhibit significant UV-Visible absorption and fluorescence. Remarkably, the synthetic monomeric protein α_3C, lacking aromatic amino acids, displays absorption in the 250–800 nm range and emits deep-blue fluorescence upon UV excitation. This unexpected optical behavior is attributed to charge transfer interactions between charged amino acid residues, particularly lysine (Lys) and glutamate (Glu). These interactions involve electron donors (e.g., carboxylate groups of Glu) and acceptors (e.g., protonated amine groups of Lys or the peptide backbone), leading to photoinduced electron transfer and subsequent charge recombination, which is responsible for the observed luminescence. This phenomenon has been termed Protein Charge Transfer Spectra (ProCharTS). Time-dependent density functional theory (TDDFT) calculations based on molecular dynamics simulations support this mechanism, highlighting the role of specific charge interactions in the absence of traditional chromophores. The discovery of ProCharTS not only broadens our understanding of protein photophysics but also offers a novel, label-free approach to monitor protein folding, aggregation, and interactions, especially in systems rich in charged residues.

In summary, the identification of ProCharTS underscores the potential of intrinsic, non-aromatic chromophores in protein spectroscopy, paving the way for new methodologies in studying protein dynamics without the need for external labels.

This thesis explores the application of Protein Charge Transfer Spectra (ProCharTS) as a label-free method to monitor critical molecular events such as protein phosphorylation, aggregation, and unfolding.

Chapter 3 presents an investigation into ProCharTS absorbance and luminescence in both phosphorylated and unphosphorylated peptide pairs, LG7, LG7 P, KK9, and KK9 $(P)_2$, as well as in the highly charged proteins alpha-casein and beta-casein. Alpha-casein and beta-casein consist of 214 and 224 amino acids, with charged residue contents of approximately 26.6 % and 20.08 %, respectively. These proteins are well-known phosphoproteins, abundant in charged residues, making them ideal candidates for studying charge transfer phenomena. Significant differences in ProCharTS absorbance and luminescence were observed between phosphorylated and unphosphorylated peptides, and between phosphorylated and dephosphorylated casein proteins. These findings suggest that ProCharTS can sensitively detect changes in phosphorylation states. The higher extinction coefficients observed in proteins, compared to peptides, indicate that the presence of proximal charged residues facilitates electron transfer, regardless of the specific types of charged amino acids involved. These features highlight the potential of ProCharTS as a non-invasive, label-free technique for detecting protein phosphorylation and studying protein dynamics.

Chapter 4 explores the application of Protein Charge Transfer Spectra (ProCharTS) in monitoring protein aggregation, focusing on alpha synuclein and human lysozyme (HuL). Protein aggregation often leads to the formation of new intermolecular contacts among charged amino acid side chains, enhancing the density of these interactions. This increase facilitates photoinduced electron transfer, resulting in elevated ProCharTS absorbance and luminescence. A progressive enhancement in ProCharTS signals was observed with the aging of alpha synuclein and HuL aggregates. This trend aligns with findings from conventional assays such as Thioflavin T (ThT), which also demonstrated increased fluorescence upon aggregation. Circular Dichroism (CD) spectroscopy further corroborated these observations, indicating structural transitions associated with aggregation. Importantly, ProCharTS exhibited heightened sensitivity in detecting early-stage oligomeric aggregates compared to traditional probes like ThT and CD. The extinction coefficients of aged aggregates were significantly higher than those of monomeric forms, underscoring the role of charged residue interactions in intrinsic luminescence. These findings position ProCharTS as a potent, label-free tool for monitoring protein aggregation dynamics.

Chapter 5 delves into the utility of ProCharTS in detecting protein unfolding, using HuL and extracellular signal-regulated kinase 2 (ERK2) as model systems. Both proteins are natively folded and rich in charged amino acids. Unfolding disrupts the proximity of charged side

chains, diminishing the efficiency of charge transfer interactions and, consequently, reducing ProCharTS absorbance and luminescence. Chemical denaturation experiments revealed a marked decrease in ProCharTS signals, with absorbance diminishing between 325–800 nm and luminescence declining upon excitation at 340 and 355 nm. These changes were consistent with results from CD spectroscopy, tryptophan fluorescence, and ANS fluorescence assays, validating the sensitivity of ProCharTS in capturing unfolding events.

Collectively, these studies highlight the versatility of ProCharTS in monitoring critical protein dynamics, including phosphorylation, aggregation, and unfolding. Its label-free nature and sensitivity to charged residue interactions make it particularly advantageous for studying proteins lacking aromatic chromophores, such as intrinsically disordered proteins (IDPs). ProCharTS thus emerges as a valuable tool for probing structural transitions and oligomerization processes in a broad spectrum of protein.

Table of Contents

CHAPTER 1:

INTRODUCTION AND REVIEW OF LITERATURE

1.1 Introduction

Proteins are fundamental to living systems, and understanding their structure-function relationships is a key focus in biophysics. Spectroscopic techniques such as absorption and fluorescence provide valuable tools for studying protein structural changes [Zaccai et al.,1017]. Optical properties arising from extrinsic fluorescent dyes and intrinsic chromophores such as aromatic amino acids, prosthetic groups, and peptide bonds have been extensively investigated in this context [Lakowicz, 2006]. However, the existence of additional intrinsic chromophores in proteins remains an open question. Exploring such novel intrinsic probes could enable non-invasive detection of biophysical processes and enhance spectroscopic analysis within the UV-Visible range (200–800 nm). This forms the central theme of my thesis. Below, I outline recent advancements in this field and the specific objectives of my research.

1.2 Conventional chromophores in proteins

When molecules absorb high-energy electromagnetic radiation, their electrons transition from lower to higher molecular orbitals. In biological macromolecules like proteins, these electronic transitions predominantly occur within the ultraviolet (200 - 400 nm) and visible (400 - 800 nm) regions of the electromagnetic spectrum. However, absorbance measurements below 200 nm can be confounded by water's strong absorption below 170 nm, leading researchers to focus on wavelengths above 200 nm for clearer insights [Quickenden et al., 1979]. In the study of biological macromolecules, particularly proteins, ultraviolet-visible (UV-Vis) spectroscopy is a fundamental tool for probing structural and conformational characteristics. Due to strong absorbance by water below 200 nm, analyses are typically conducted at wavelengths above this threshold to minimize interference [Serdyuk et al., 2007]. Proteins possess several intrinsic chromophores that are pivotal in spectroscopic analyses to elucidate their structural and functional attributes. These chromophores include peptide bonds, aromatic amino acids, prosthetic groups, and coenzymes. Below is an overview of these key chromophores:

1.2.1 Peptide bond

The peptide bond contains both delocalized π electrons and localized non-bonding electrons. The π electrons are spread across the nitrogen (N), carbon (C), and oxygen (O) atoms, which imparts partial double-bond character and enforces planarity within the bond structure. In contrast, the non-bonding electrons remain localized as lone pairs on the oxygen atom. Peptide bonds in proteins exhibit two primary electronic transitions in the far-ultraviolet (UV) region: the π→π* and n→π* transitions.

- **π→π*:** This transition involves the excitation of delocalized π electrons across the carbonyl (C=O) and amide (N–H) groups of the peptide bond. It results in a strong absorption peak around 190 nm, with a high molar absorptivity (ε_max) of approximately 7000 $M^{-1}cm^{-1}$ [Chang, 2005].

- **n→π*:** This transition entails the excitation of non-bonding (n) electrons, primarily from the oxygen atom in the carbonyl group, to the π* antibonding orbital. It produces a weaker absorption band between 210 - 220 nm, with an ε_max of about 100 $M^{-1}cm^{-1}$ [Chang, 2005].

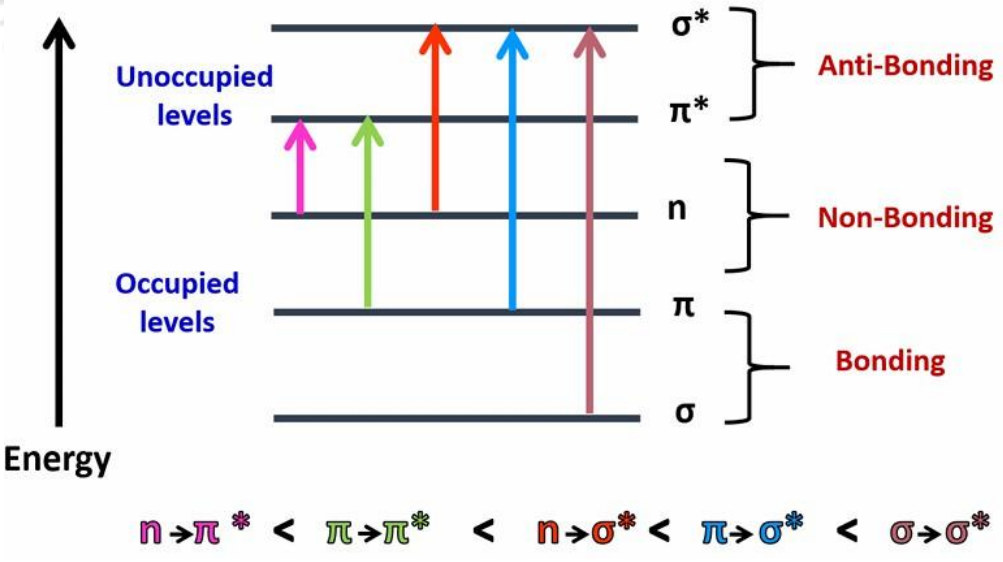

Figure 1.1: Electronic energy levels and transitions (Adapted from Pavia and Lampman, 2009)

The intensity and position of these absorption bands are sensitive to the protein's secondary structure. For instance, α-helical conformations typically exhibit lower absorbance

compared to β-sheet or random coil structures, due to differences in hydrogen bonding and electronic environments [Wetlaufer, 1963]. While peptide bond absorption at 220 nm has been utilized for protein quantification, caution is necessary. Other amino acid residues, such as histidine, cysteine, and methionine, also absorb in the far-UV region. Histidine shows significant absorbance between 190 - 220 nm but negligible beyond 230 nm. Cysteine and methionine absorb in the far-UV, and their oxidized form, cystine, exhibits absorbance extending into the near UV region [Wetlaufer, 1963]. Notably, cystine has an ε max of approximately 50 $M^{-1}cm^{-1}$ at 290 nm, contributing to the absorbance of proteins rich in disulfide bonds. These considerations are crucial when interpreting UV absorption spectra for protein analysis, as overlapping absorbance from various residues can influence the accuracy of structural and concentration assessments.

1.2.2 Aromatic amino acids

In proteins, ultraviolet (UV) absorbance is primarily attributed to the aromatic amino acids tryptophan (Trp), tyrosine (Tyr), and phenylalanine (Phe) due to their conjugated π-electron systems. These systems facilitate π→π* electronic transitions, resulting in significant absorbance in the near-UV region (wavelengths longer than 230 nm) [Cantor and Schimmel, 1980] (Figure 1.2). Among these, tryptophan exhibits the most substantial absorbance, primarily due to its indole side chain. It has two notable absorption peaks: one around 220 nm with a molar extinction coefficient (ε) of approximately 36,000 $M^{-1}\cdot cm^{-1}$, and another at 280 nm with ε = 5,500 $M^{-1}\cdot cm^{-1}$ [Bent et al., 1975; Creed, 1984]. Tyrosine also contributes to protein UV absorbance, with a peak at 275 nm (ε = 1,490 $M^{-1}\cdot cm^{-1}$) and another at 222 nm (ε = 9,000 $M^{-1}\cdot cm^{-1}$) [Antosiewicz et al., 2016]. Phenylalanine, while less prominent, displays absorbance with two peaks: one around 257 nm (ε = 200 $M^{-1}\cdot cm^{-1}$) [Bent et al., 1975; Wetlaufer, 1963] and another near 205 nm (ε = 9,600 $M^{-1}\cdot cm^{-1}$).

The absorbance properties of tyrosine are highly pH-dependent, more so than those of other aromatic amino acids [Antosiewicz et al., 2016]. At alkaline pH levels, the phenolic hydroxyl group in tyrosine's side chain undergoes deprotonation, forming a tyrosinate anion [Cantor and Schimmel, 1980]. This ionization leads to a red shift in the absorbance spectrum, altering the optical properties of tyrosine residues. Tryptophan and phenylalanine also exhibit pH-dependent absorbance changes, though to a lesser extent compared to tyrosine. These

variations are attributed to alterations in the local environment and solvent interactions affecting the π→π* electronic transitions within their aromatic rings [Cantor and Schimmel, 1980]. This sensitivity of aromatic amino acid absorbance to environmental conditions is leveraged in monitoring protein folding and unfolding processes.

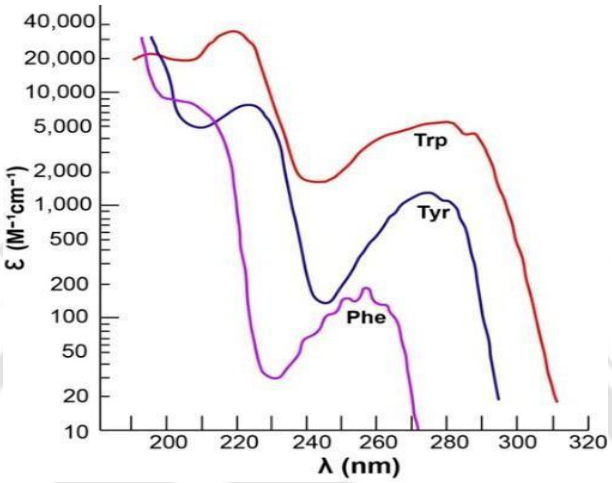

Figure 1.2: Absorption spectra of aromatic amino acids in the near and far UV region (Adapted from Biophysical Chemistry, Part II, 1980) [Cantor and Schimmel, 1980].

Beyond these aromatic residues, other amino acids contribute to UV absorbance at lower wavelengths. Histidine, cysteine, and methionine exhibit absorbance between 185–220 nm and 230–240 nm, respectively [Wetlaufer, 1963]. Additionally, cystine (the oxidized dimer form of cysteine) shows absorbance bands at longer wavelengths, between 250–270 nm, with $\varepsilon = 300\ M^{-1}\cdot cm^{-1}$ [Otey and Greenstein, 1954]. These absorbance characteristics are instrumental in spectrophotometric methods for protein quantification, particularly measurements at 280 nm, which are predominantly influenced by the presence of tryptophan and tyrosine residues.

1.3 Charge Transfer complexes

Beyond the aromatic amino acids previously discussed, proteins also exhibit absorbance due to charge-transfer (CT) chromophores, which involve the movement of electrons from donor to acceptor groups. These CT interactions are pivotal in various biological processes, such as photosynthesis and cellular respiration, where electron transfer is essential. In photosynthetic organisms, for instance, CT transitions occur between chlorophyll molecules, facilitating the conversion of light energy into chemical energy [King et al., 2001]. Similarly,

in the electron transport chain of respiration, metalloproteins like cytochromes and iron-sulfur proteins utilize CT mechanisms to transfer electrons efficiently [Lodish et al., 2000]. Metalloproteins often exhibit two primary types of CT transitions: ligand-to-metal charge transfer (LMCT) and metal-to-ligand charge transfer (MLCT) [Balzani et al., 2007]. These transitions are characterized by their intense absorption bands in the UV-Visible spectrum, making them easily detectable through spectroscopic methods. For example, blue copper proteins, such as plastocyanin and azurin, display strong absorption due to LMCT transitions, contributing to their distinctive coloration and functional properties [Crosby et al., 1975]. Additionally, proteins containing heme groups, like cytochromes and myoglobin, showcase CT interactions between the iron center and surrounding ligands. These interactions are crucial for their roles in oxygen transport and electron transfer.

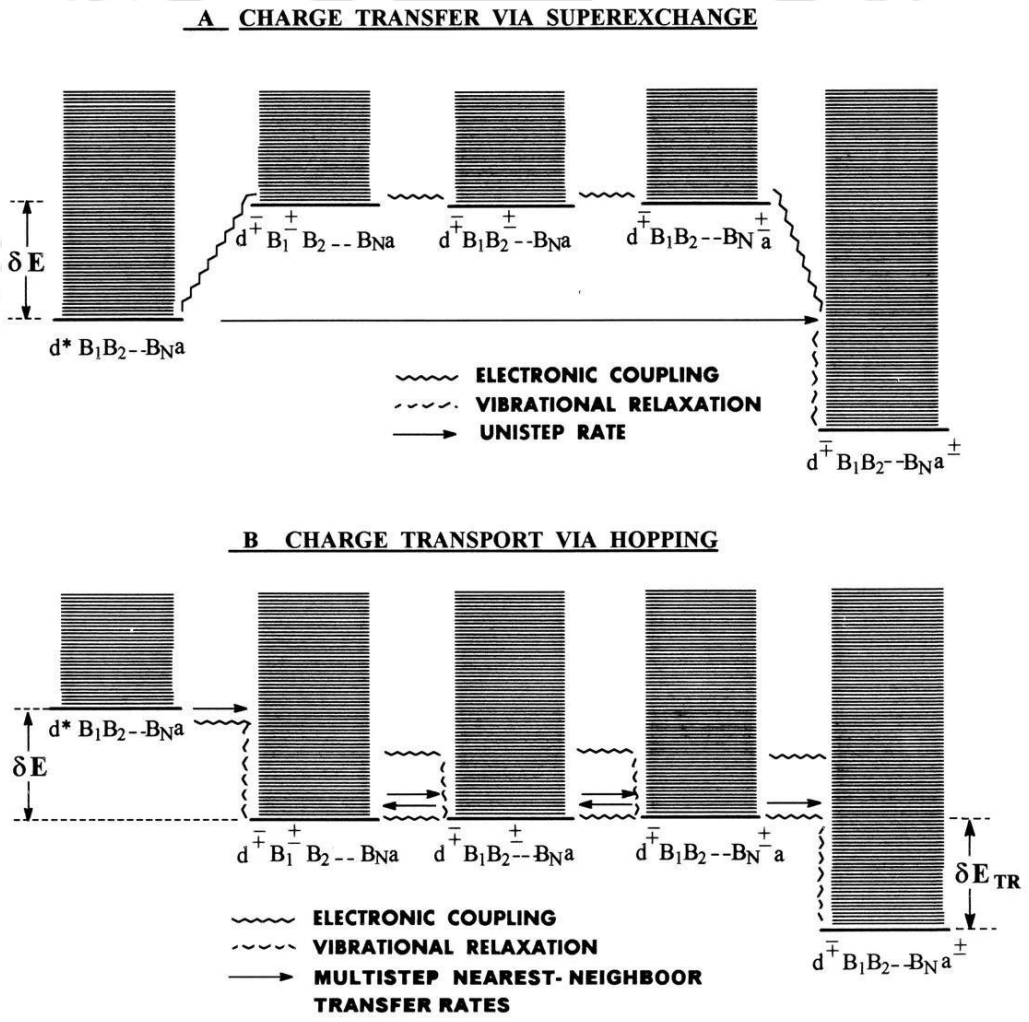

Figure 1.3: Vibronic level scheme for the two distinct charge migration mechanisms in DNA. (A) Unistep charge transfer via superexchange. (B) Multistep charge transport via hopping

and trapping (Jortner et al., 1998).

Similar to the metal-centered CT, proteins can also exhibit CT interactions between amino acid residues. Tyrosine and tryptophan residues can form CT pairs, facilitating long-range electron transfer within proteins. Such interactions are observed in enzymes like ribonucleotide reductase, where a tyrosine - tryptophan dyad mediates high-potential electron transfer reactions [Pagba et al., 2015]. These processes can occur via mechanisms like super-exchange [Polo et al., 2005] or multistep hopping [Jortner et al., 1998], depending on the protein's conformation and the spatial arrangement of residues (Figure 1.3).

Furthermore, the protein's secondary structure, particularly α-helices, can influence CT efficiency. Electron transfer rates have been found to correlate with the dipole moment direction of α-helices, with faster rates observed along the dipole direction. This suggests that the protein's structural features play a significant role in modulating CT processes (Figure 1.4) [Arikuma et al., 2010; Kai et al., 2008].

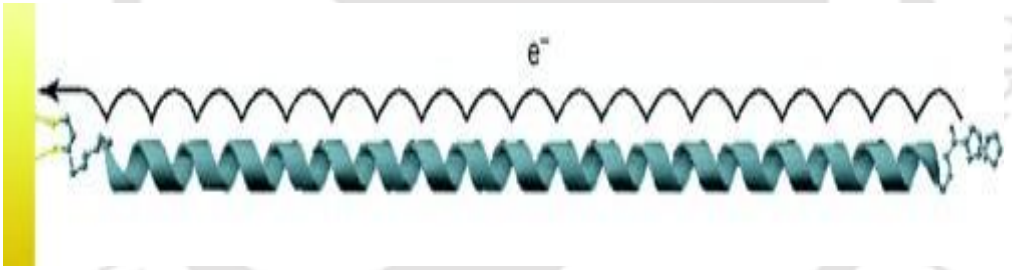

Figure 1.4: Take the stepping stones: Electrons are exchanged between both termini of α-helical peptide self-assembled monolayers (SAMs) on gold by a hopping mechanism with the amide groups as hopping sites (Arikuma et al. 2010).

In summary, charge-transfer interactions, both metal-centered and between amino acid residues, are integral to protein function, influencing processes from energy conversion to enzymatic activity. Understanding these interactions provides deeper insights into the molecular mechanisms underpinning vital biological functions.

1.4 Non-conventional chromophores in proteins

Most of the chromophores discussed earlier are either inherent to apoproteins, such as

peptides and aromatic amino acids or are metal complexes. However, in the 21st century, several studies have reported unusual UV-Visible absorption spectra above 315 nm, sometimes extending up to 800 nm, in aqueous solutions of charged amino acids like S/R-Lysine [Ryzhkina et al., 2018], L-Lysine-HCl (Figure 1.5) [Homchaudhuri et al., 2001], and poly-L-lysine-HCl [Homchaudhuri et al, 2004]. Similar absorbance patterns have also been observed in a variety of amino acids [Chen et al., 2018; Stephens et al., 2020] and other solutes [Chai et al., 2008], although the specific chromophores responsible for these spectra remain unidentified.

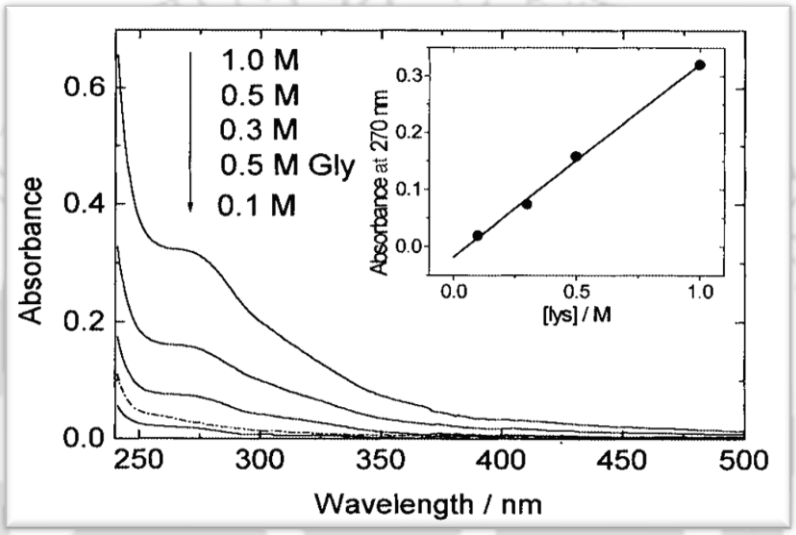

Figure 1.5: Absorption spectra of L-lysine monohydrochloride from 0.1 – 1.0 M in 0.1 M NaH_2PO_4, pH 7 at room temperature (Homchaudhuri et al., 2001).

In contrast to absorption, intrinsic luminescence has recently attracted significant interest. This phenomenon has been reported not only in proteins but also in a range of biopolymers, nucleic acids, and carbohydrates. Numerous studies have documented intrinsic fluorescence or deep-blue/blue luminescence from monomeric [Kumar et al., 2020] and oligomeric proteins [Guptasarma et al., 2008; Bhattacharya et al., 2017]], protein crystals [Shukla et al., 2004], and amyloid aggregates [Chan et al., 2013; Tikhonova et al., 2018]. Likewise, dendrimers (such as PAMAM), various small molecules [Konopka et al., 2018], and both synthetic and natural polymers lacking traditional fluorophores have also been found to exhibit this type of luminescence.

1.5 Protein Charge Transfer Spectra

So far, we have explored the phenomenon of charge transfer and its presence across the biological spectrum from simple peptides to complex protein networks, and from base hopping in nucleic acids to the vital mechanisms of enzymes. As outlined in Section 1.4, there has been a significant surge in interest in studying non-conventional chromophores derived from various biopolymers.

To further investigate the role of lysine side chains and other charged amino acids, our group conducted studies using a monomeric synthetic protein, α3C [Tommos et al., 2013]. This protein lacks aromatic amino acids but is rich in charged residues, particularly lysine and glutamate. Structurally, α3C consists of a three-helix bundle and comprises 67 amino acids, of which approximately 54% are charged, including 17 lysines, 17 glutamates, and 2 arginines.

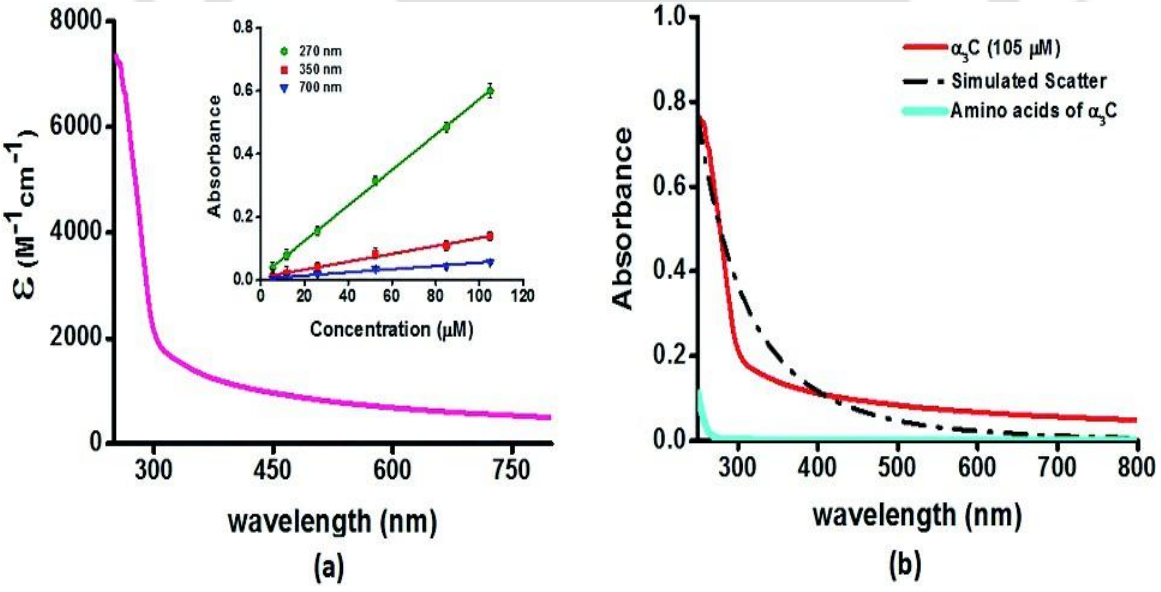

Figure 1.6: Panel (a) shows the absorption spectrum (250–800 nm) of α3C in water. Inset shows a linear concentration dependence of absorbance at different wavelengths. Panel (b) shows the comparison of absorption spectrum (250–800 nm) of the intact α3C protein with that of a solution mixture of constituent amino acids in α3C. The concentration of individual amino acids is adjusted to match that of present in 105 μM α3C. Simulated scatter is shown as dots and dashes (Prasad et al., 2017).

α3C exhibits a broad absorption spectrum extending from 250 to 800 nm. Despite lacking aromatic amino acids, it shows strong absorption in the 250–300 nm range, followed by a broad absorption tail that continues beyond 300 nm up to 800 nm (Figure 1.6 a). This broad tail was not attributed to artifacts such as light scattering or increased extinction coefficients due to intermolecular interactions. Therefore, the observed absorption spectrum is believed to originate from monomeric α3C molecules, with charged residues playing a key role. Furthermore, the three-dimensional structure of the protein appears to be essential for facilitating interactions between the charged side chains, as a mixture of the individual amino acids present in the protein shows only negligible absorption in the same spectral region (Figure 1.6).

The excess charge on the side chains of charged amino acids can polarize the frontier molecular orbitals, leading to the formation of well-defined Donor–Bridge–Acceptor (D-B-A) groups. Donor (D) groups possess filled orbitals, while acceptor (A) groups feature empty frontier orbitals. Time-dependent density functional theory (TDDFT) calculations from molecular dynamics (MD) simulation snapshots on these systems have revealed the presence of charge-transfer (CT) transitions between the donor and acceptor groups. These CT transitions are responsible for the unusual absorption spectra observed in proteins rich in charged residues. This distinct absorption profile, arising from CT transitions, has been termed ProCharTS (Protein Charge Transfer Spectra) [Prasad et al., 2017]. These CT transitions are classified into two main types: peptide backbone to side-chain (PBS) CT transitions and side-chain to side-chain (SS) CT transitions.

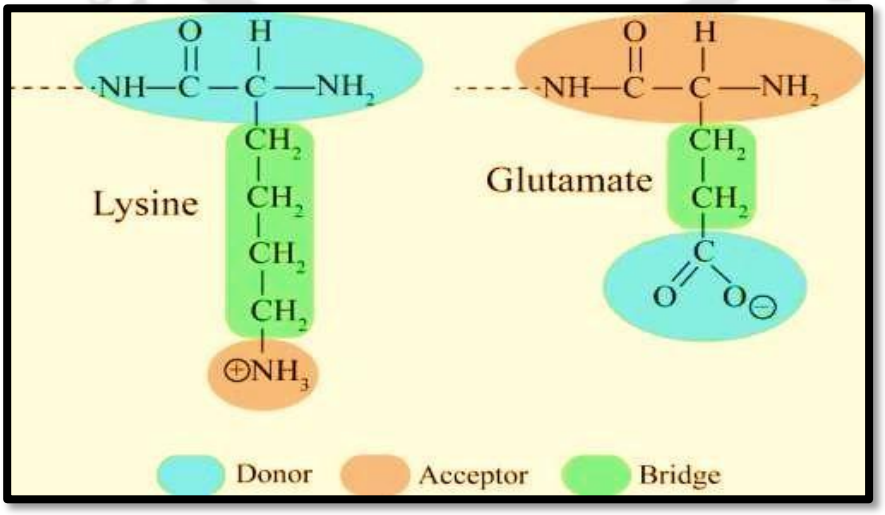

Figure 1.7: The colored segments represent the Donor (D), Acceptor (A), and Bridge (B) components for the PBS CT transitions in polypeptides. (Adapted from Mandal et al., 2018).

PBS CT transitions are low-energy processes that can be described in terms of the ground-state dipole moments of the chromophores involved. In these transitions, photo-induced electron transfer occurs either from the polypeptide backbone to the NH_3^+ group in lysine, or from the COO^- group in glutamate to the polypeptide backbone, mediated through the connecting carbon chain. This carbon chain, linking the polypeptide backbone to the charged head group of Glu or Lys side chains, serves as the bridge in the D–B–A system (Figure 1.7) [Mandal et al., 2018].

In the glutamate-to-backbone transition, the COO^- group acts as the electron donor, and the backbone as the acceptor. Conversely, in the lysine-to-backbone transition, the polypeptide backbone donates an electron, while the NH_3^+ head group serves as the acceptor (Figure 1.8).

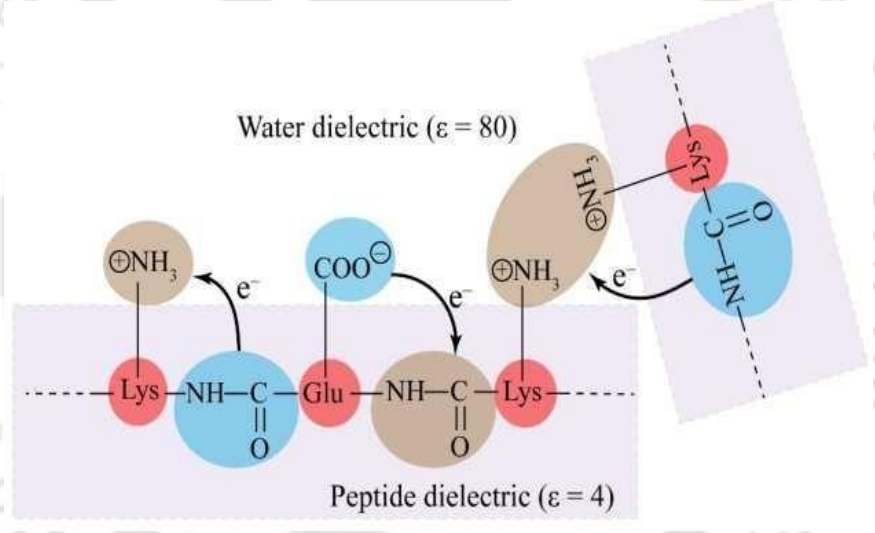

Figure 1.8: Schematic representing the Peptide Backbone - Sidechain (PBS) charge transfer transitions. Close interactions between sidechains with like charges lead to more delocalized A states and lower the CT transition energy (Adapted from Prasad et al., 2017).

In SS CT transitions, electrons are transferred directly from the glutamate side chain (COO^-) to the lysine side chain (NH_3^+), making glutamate the donor and lysine the acceptor (Figure 1.9). In these cases, the bridge (B) component is variable and highly dependent on the local environment, including the solvent and protein structure. The bridge may consist of varying numbers of water molecules or intervening side-chain groups, depending on the spatial

proximity between the donor and acceptor residues.

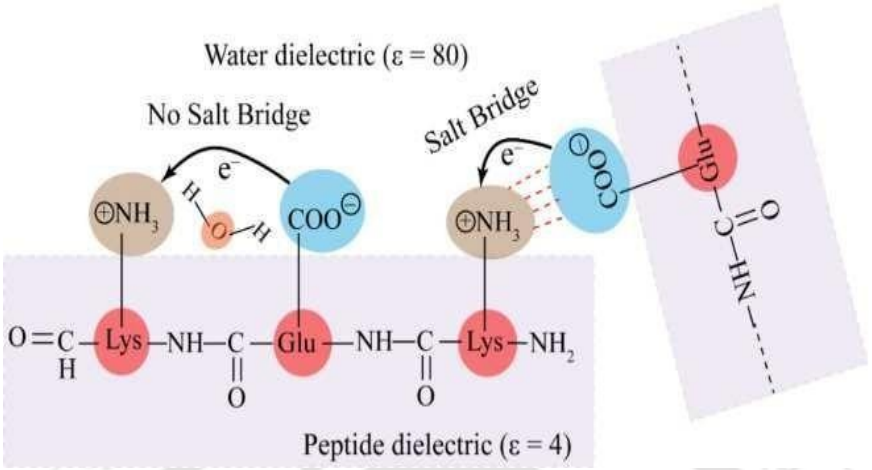

Figure 1.9: Schematic representing the Sidechain - Sidechain (SS) charge transfer transitions. (Adapted from Prasad et al., 2017).

The three-dimensional folding among proteins can bring side chain head groups of amino acids that are distant in the sequence into close spatial proximity, significantly influencing charge transfer (CT) transitions. When pairs of charged side chains such as Glu-Glu, Lys-Lys, or Glu-Lys, are situated near each other, they can modulate the relative stabilities of the ground state (Ψ_G) and the excited state (Ψ_E), depending on their separation distance. In cases where like-charged residues (Lys-Lys or Glu-Glu) are brought close together, electrostatic repulsion occurs. This repulsion destabilizes the ground state (Ψ_G), while the excited state (Ψ_E) may become stabilized due to the increased likelihood of electron transfer to the Lys amino or from the Glu carboxylate pairs. As a result, the energy gap between the HOMO and LUMO levels reduces, thereby enhancing the probability of Peptide Backbone to Side Chain Charge Transfer (PBS-CT) transitions (Figure 1.8, right). For instance, reducing the distance between a Lys-Lys pair from 6–7.5 Å to 3–4 Å decreases the HOMO-LUMO energy gap from 4.5 ± 0.8 eV to 3.4 ± 0.2 eV (Figure 1.10). A similar effect is observed for Glu-Glu pairs.

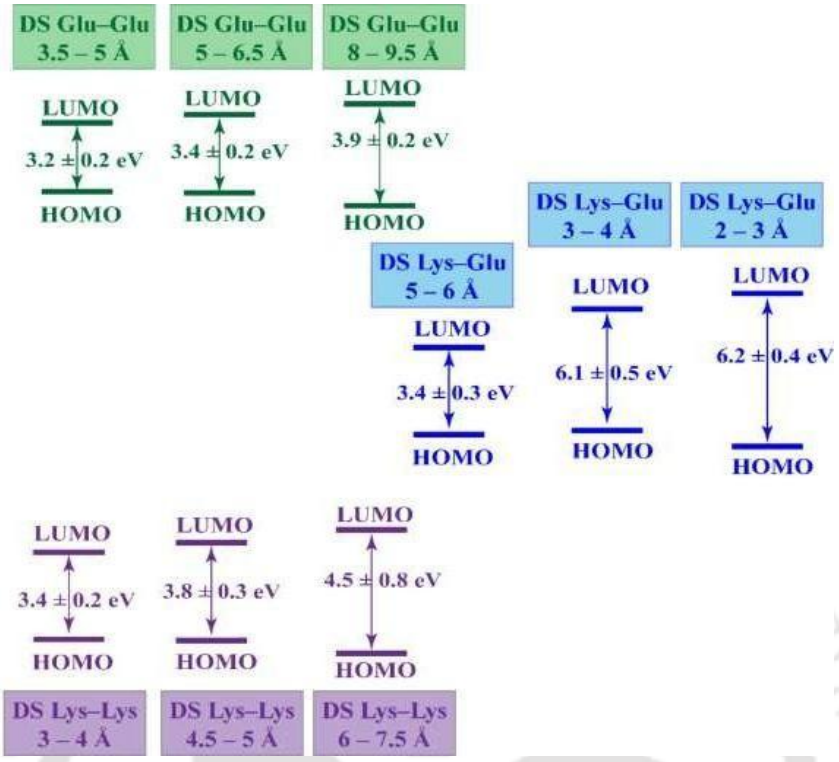

Figure 1.10: Average ground-state HOMO-LUMO gaps for different pairs calculated from 100 MD snapshots are presented. Here, different HOMO-LUMO gaps for the Lys-Lys, Glu-Glu and Lys-Glu are compared as a function of proximal distance between them. DS stands for Distally Separated. (Adapted from Prasad et al., 2017).

Conversely, when Glu and Lys side chains are in close proximity, favorable electrostatic interactions such as salt bridge formation stabilize the ground state (Ψ_G) (favorable electrostatics) and destabilize the excited state (Ψ_E) (neutralization of charge). This increases the HOMO-LUMO energy gap (Figure 1.10). However, when the Glu-Lys side chains are farther apart, the ground-state stabilization and excited-state destabilization diminish, resulting in a reduced energy gap. This reduction can enhance Side Chain to Side Chain Charge Transfer (SS-CT) transitions (Figure 1.9). For example, increasing the separation between a Glu-Lys pair from 2–3 Å to 5–6 Å lowers the HOMO-LUMO gap from 6.2 ± 0.4 eV to 3.4 ± 0.3 eV (Figure 1.10).

Building on the understanding of how distance influences charge transfer (CT) transitions, a more comprehensive analysis was conducted using TDDFT-simulated absorption spectra. These spectra were generated for three charged residue pairs: Lys-Lys, Glu-Glu, and Lys-

Glu across a range of increasing distances between interacting side chains (Figure 1.11). For both Lys-Lys and Glu-Glu interactions, the absorption spectra revealed low-energy transitions. In the case of the Lys-Lys pair (Figure 1.11; 1a–3a), the absorption extended up to 550 nm under strong interaction conditions, 500 nm for intermediate interactions, and 350 nm for weak interactions.

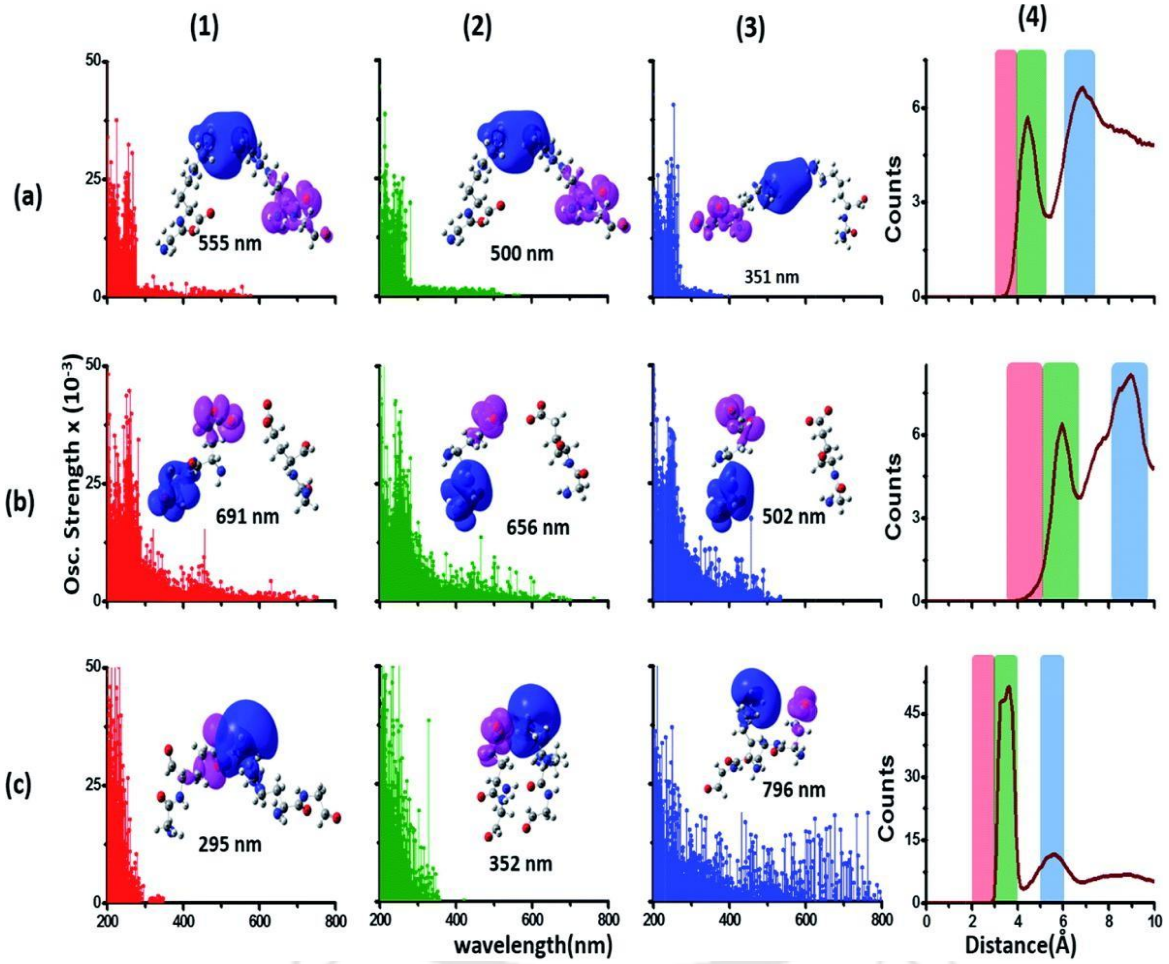

Figure 1.11: Simulated absorption spectra (wavelength vs. oscillator strength) for distally separated Lys–Lys (a1–a3), Glu–Glu (b1–b3), and Lys–Glu (c1–c3). Each panel displays spectra from 100 amino acid structures extracted from 100 ns MD trajectories of α3C. The distance between the Lys–Lys (Row a), Glu-Glu (Row b) and Lys-Glu (Row c) head groups for which the CT transitions are displayed are chosen from the corresponding color-coded regions of the RDF (radial distribution function) plots in last column. Precisely the distance is indicated in Figure 1.15. In each absorption spectra panel (a1–a3, b1–b3 and c1–c3) difference density plots show regions with decrease in electron density (pink lobes) and regions with increase in electron density (blue lobes) on Lys/Glu fragments for the lowest energy transitions in that panel. (Adapted from Prasad et al., 2017).

Similarly, the Glu-Glu pair (Figure 1.11; 1b–3b) displayed absorption extending up to 690 nm for strong interactions, 650 nm for intermediate, and 500 nm for weak interactions.

In contrast, the Lys-Glu pair exhibited an inverse relationship between interaction strength and CT spectral range. Weakly interacting Lys-Glu pairs showed prominent transitions extending up to 800 nm (Figure 1.11; 3c), while in cases of strong and intermediate interactions (Figure 1.11; 1c and 2c), the transitions were confined to around 350 nm. This restriction in spectral extension is attributed to the formation of salt bridges between the oppositely charged residues, which neutralizes the charge and limits CT transitions as discussed earlier.

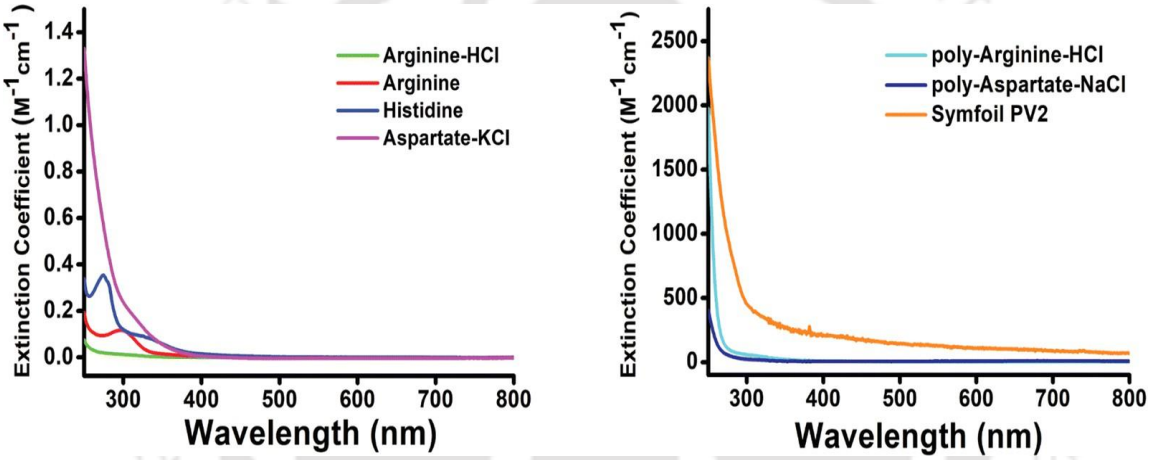

Figure 1.12: Absorption spectra with molar extinction coefficient for different amino acids, homo-polypeptides, and Symfoil PV2. The extinction coefficient for amino acids is plotted against wavelength in the left panel, whereas the same for homo-polypeptides and Symfoil PV2 is shown in the right panel (Alom et al., 2023).

In addition to lysine and glutamate, similar charge-transfer (CT) transitions have also been observed with other charged amino acids such as arginine, aspartate and histidine (Figure 1.12) [Alom et al., 2023] as well as with phosphorylated residues including phosphorylated serine (pSer), threonine (pThr), and tyrosine (pTyr) [Mandal et al., 2018].

ProCharTS absorbance has been effectively used to analyze conformational changes in proteins resulting from variations in pH and temperature. It has shown potential as a valuable

tool for monitoring the aggregation of Human Egg White Lysozyme (HEWL) [Ansari et al. 2018]. Additionally, ProCharTS absorbance has also been applied to detect protein DNA binding [Priyadarshi et al., 2024], capsid formation [Alom et al., 2024] and protein unfolding [Priyadarshi et al., 2023].

1.5.1 Protein Charge Transfer Spectra (ProCharTS) luminescence

Numerous monomeric proteins rich in charged residues have been reported to exhibit luminescence when excited by near-UV light in the 325–400 nm range [Kumar et al., 2020]. The proteins examined included both natively folded examples, such as HSA and α3C, and intrinsically disordered proteins, such as fragments of the human c-Myc PEST region and DHN1. Common characteristics of the observed luminescence included similar steady-state emission and excitation spectra, moderate to low quantum yields, and large Stokes shifts. The increase in integrated luminescence intensity with protein concentration was found to correlate with the density of proximal charged amino acid contacts within the 3D structure of the proteins. Additionally, the proteins displayed comparable mean luminescence lifetimes (ranging from 0.4 to 2.9 ns) and exhibited multi-exponential luminescence decay kinetics. These consistent photophysical properties across various proteins suggest a shared luminescence mechanism. It is hypothesized that charge recombination luminescence may underlie this novel photophysical behavior.

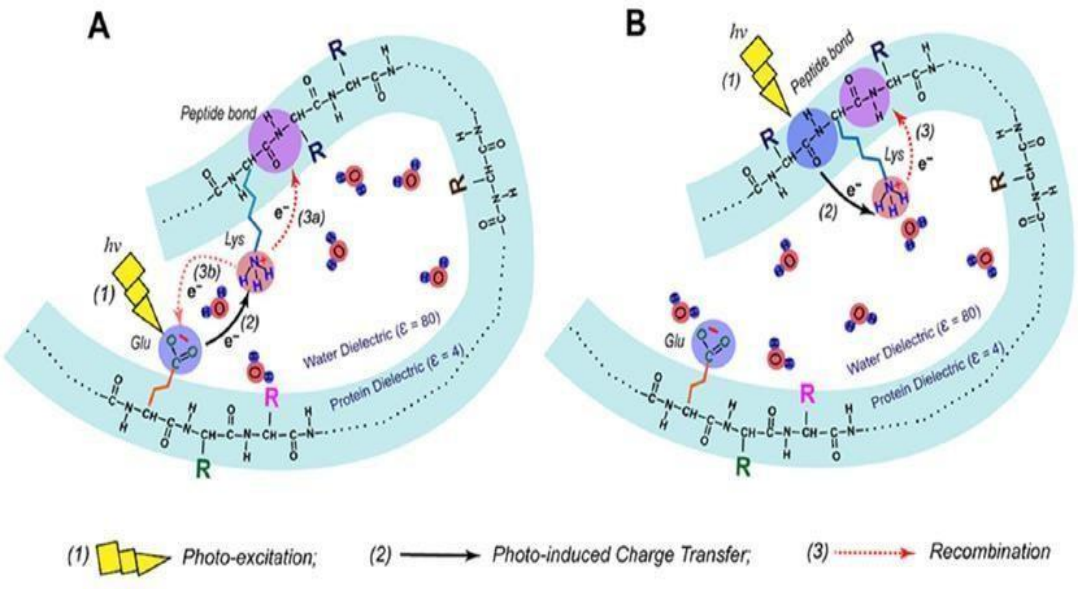

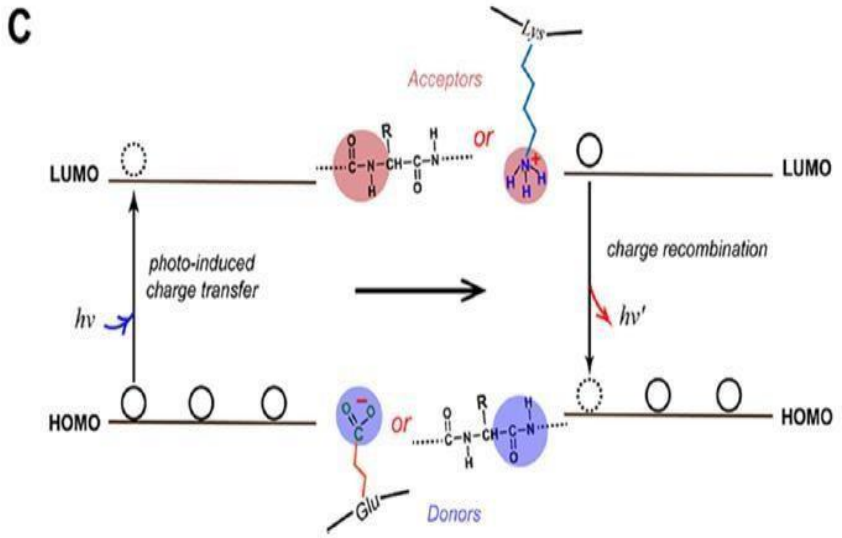

Figure 1.13: Schematic illustrating charge recombination luminescence. (Adapted from Kumar et al., 2020).

The generation of charge recombination luminescence (Figure 1.13) involves three key processes: (1) photo-excitation, (2) photo-induced charge transfer, and (3) charge recombination. Following photo-excitation, an electron can be transferred from a donor site such as a Glu side chain or peptide bond to an acceptor site like a peptide bond or Lys side chain. This is followed by charge recombination, which may occur within the same LUMO-HOMO pair or between nearby HOMO-LUMO pairs. The efficiency of this recombination process directly influences the quantum yield. It has been proposed that the high density of closely positioned charged amino acid side chains in human serum albumin (HSA) enhances the molar absorptivity, thereby increasing luminescence intensity.

1.6 Theoretical evidence of ProCharTS in phosphorylated amino acids

Post-translationally modified amino acids include di-anionic (doubly protonated) forms of phosphorylated serine (Ser), threonine (Thr), and tyrosine (Tyr) residues at physiological pH. The spectral characteristics of these di-anionic species can be more directly compared to those of singly charged amino acids such as glutamate (Glu) and aspartate (Asp) [Mandal et al., 2018].

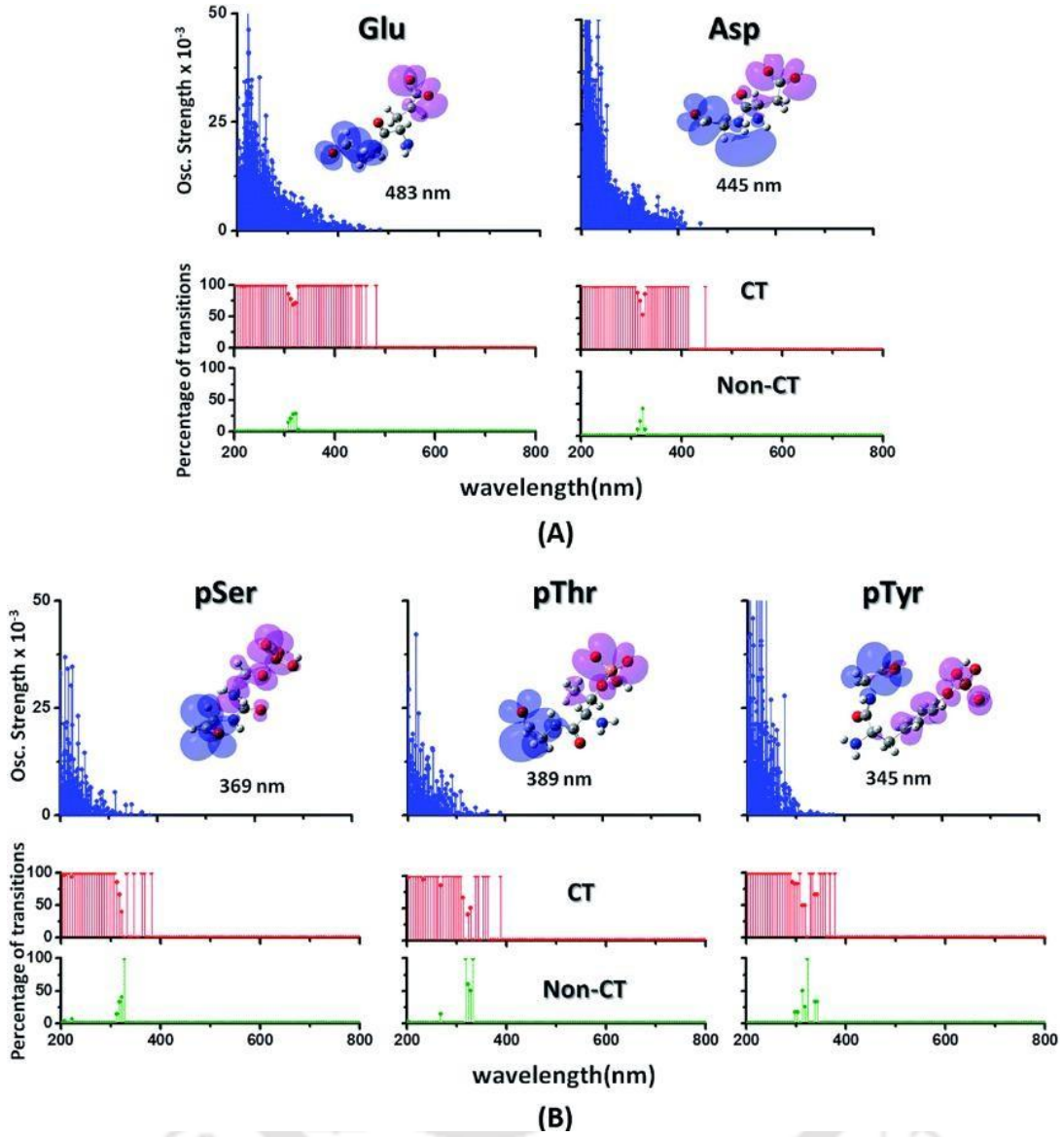

Figure 1.14: Simulated absorption spectra (wavelength vs. oscillator strength) for the anionic amino acid monomers. The top panels show spectra for (A) 100 conformations of the Glu and Asp amino acids sampled from a 1 μs MD trajectory of ubiquitin and for (B) 10 different conformations of pSer, pThr and pTyr taken from crystal and NMR structures from the Protein Data Bank. Each amino acid fragment has an extended backbone capped with hydrogen atoms. The lower panels in (A) and (B) show the assignment of transitions in the spectra to CT vs. non-CT transitions across the absorption profile. Difference density plots (the pink lobes represent hole density and the blue lobes represent electron density after photoexcitation) for the lowest energy transitions for each spectrum are shown in the insets of the top panels in (A) and (B). (Adapted from Mandal et al., 2018).

The calculated spectra (Figure 1.14) for the phosphorylated residues pSer, pThr, and pTyr

all fall below 400 nm, with the lowest energy transitions occurring at 369 nm, 389 nm, and 345 nm, respectively. The difference density plots corresponding to these lowest energy transitions in each case reveal distinct separation between the photoexcited hole and electron densities, localized on the phosphate group and the peptide backbone, respectively. This spatial separation confirms that these are phosphate-to-backbone charge transfer (PBS-CT) transitions.

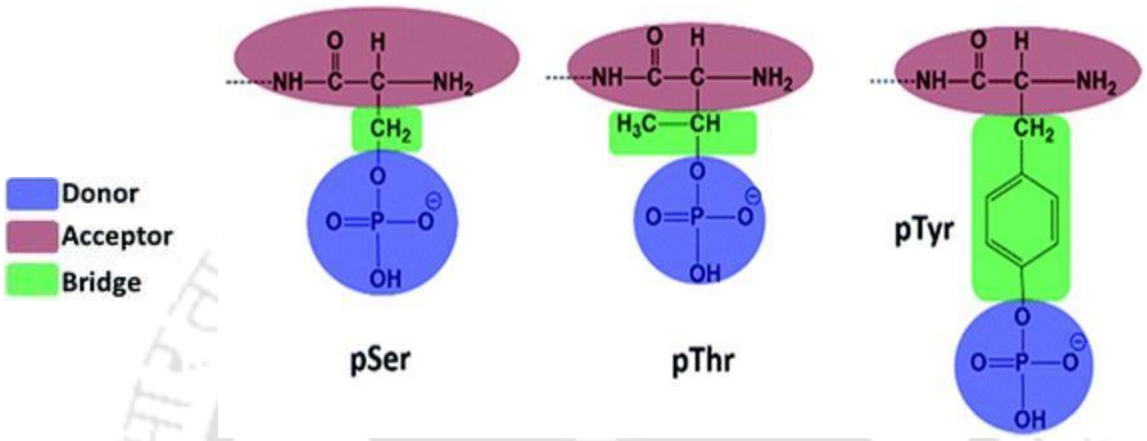

Figure 1.15: Phosphorylated amino acids considered in this study. The colored segments indicate the electronic donor (D)–bridge (B)–acceptor (A) segments for the PBS-CT transitions expected in these systems (Adapted from Mandal et al., 2018).

In phosphorylated amino acids, while the A (peptide backbone) and D (phosphate group) units remain consistent, the B (alkyl chain) units vary (Figure 1.15). Both pSer and phosphothreonine (pThr) possess B units with σ-character, leading to similar ground-state energy gaps, which correspond to their comparable spectral features. Conversely, the chromophore of phosphotyrosine (pTyr) has a B unit with π-character. This results in significant delocalization across the phosphate group and the aromatic ring of tyrosine, forming an extended D state.

Although, the average ground-state energy gap of pTyr is similar to those of pSer and pThr, its lowest energy gap is 0.4–0.5 eV lower (Figure 1.16). Interestingly, the lowest-energy peptide backbone-sidechain charge transfer (PBS-CT) transition for pTyr is 0.2–0.4 eV higher than those observed for pSer and pThr, highlighting the complexities in comparing PBS-CT excitation energies across systems with different B units.

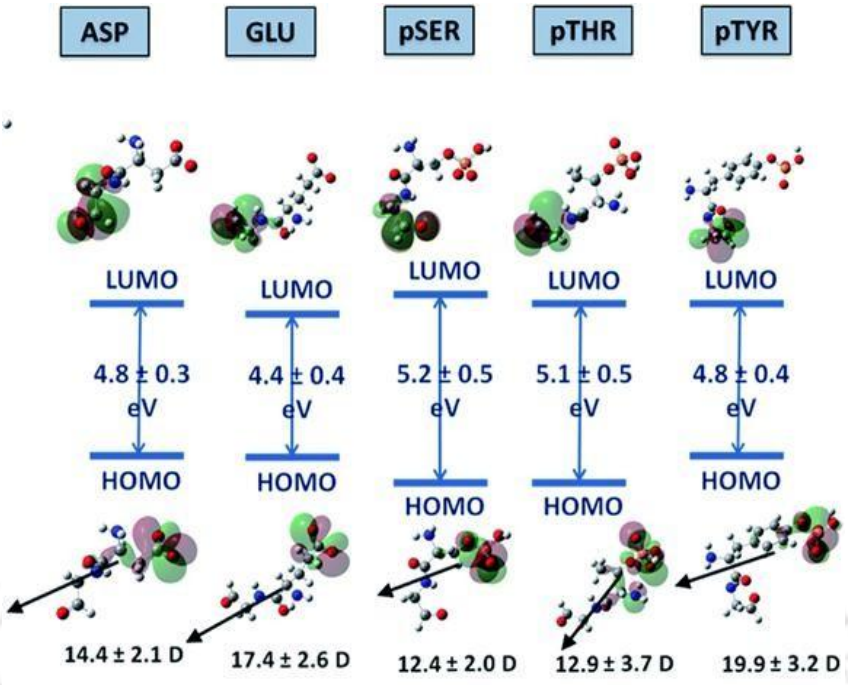

Figure 1.16: Average ground state HOMO–LUMO gaps and dipole moment values along with their standard deviation from 100 conformations of all of the anionic amino acids. The representative molecular structures at the top and bottom of the energy gap diagrams are identical, showing HOMO (bottom structures) and LUMO (top structures) contours plotted with an isovalue of 0.02. Ground state dipole vectors (arrows going from the negative end to the positive end on the bottom structures) for each system are also shown. (Adapted from Mandal et al., 2018).

Furthermore, the pTyr spectrum exhibits more intense transitions within the 200–300 nm range compared to other phosphorylated residues, with charge transfer transitions dominating the spectral range above 200 nm (Figure 1.14). Therefore, ProCharTS can be used as a tool to monitor phosphorylation leading to structural changes in the protein.

1.7 Charge Transfer in Aggregation

Protein crystals, including crystals of γ-B crystallin, hen egg white lysozyme (HEWL), and six others, have been observed to emit blue light when excited with near-ultraviolet (UV) wavelengths [Shukla et al., 2004]. Notably, this emission occurs even in the absence of aromatic amino acids, as demonstrated by a γ-crystallin 14-mer lacking such residues, which

still exhibited similar luminescence. Although the emission from this 14-mer peptide in solution was weaker, it remained significant. The emitted light was found to be photo-bleachable and could be quenched by potassium iodide (KI), indicating that the emission is due to fluorescence rather than Raman scattering. These findings suggest that the fluorescence arises from peptide bond electrons, which become delocalized through the formation of intra- and intermolecular hydrogen bonds, leading to aggregation-induced emission (AIE). This phenomenon aligns with the broader concept of AIE, where certain molecules exhibit enhanced fluorescence upon aggregation due to restricted intramolecular motions and increased electron delocalization. In the context of proteins, the aggregation and hydrogen bonding of peptide backbones can facilitate such electron delocalization, resulting in observable fluorescence even in the absence of traditional chromophores like aromatic amino acids.

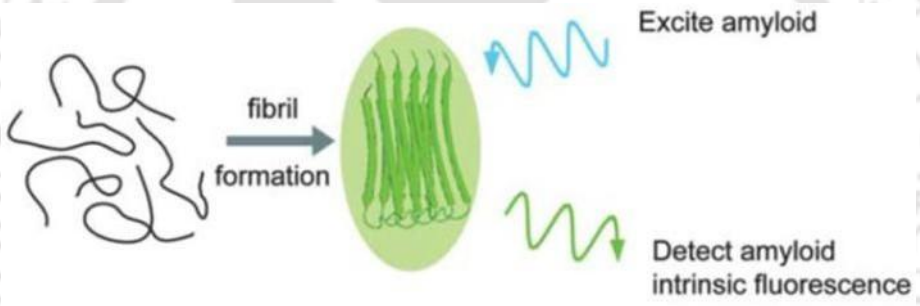

Figure 1.17: Illustration of intrinsic fluorescence from amyloid fibrils. (Adapted from Chan et al., 2013).

Blue emission naturally occurring upon near-UV excitation has also been observed from fibrils of five amyloidogenic proteins (Aβ42, Aβ40, Aβ33-42, K18 Tau, and I59T lysozyme) [Chan et al., 2013]. The novel luminescence was proposed as a potential method for label-free detection of protein aggregation (Figure 1.17).

The origin of deep blue luminescence remains quite elusive. Possible sources of this intrinsic fluorescence include proton transfer within fibrils of aggregated proteins through hydrogen bonding [Pinotsi, 2016], as illustrated in Figure 1.18; or chemical modifications of amino acids caused by oxidation [Tikhonova et al., 2018]. Additionally, the carbonyl double bonds present in proteins such as HEWL, BSA, and β-lactoglobulin have also been proposed as the chromophores responsible for this blue luminescence [Niyagoda et al., 2017], indicating a

role for charge transfer involving these carbonyl groups.

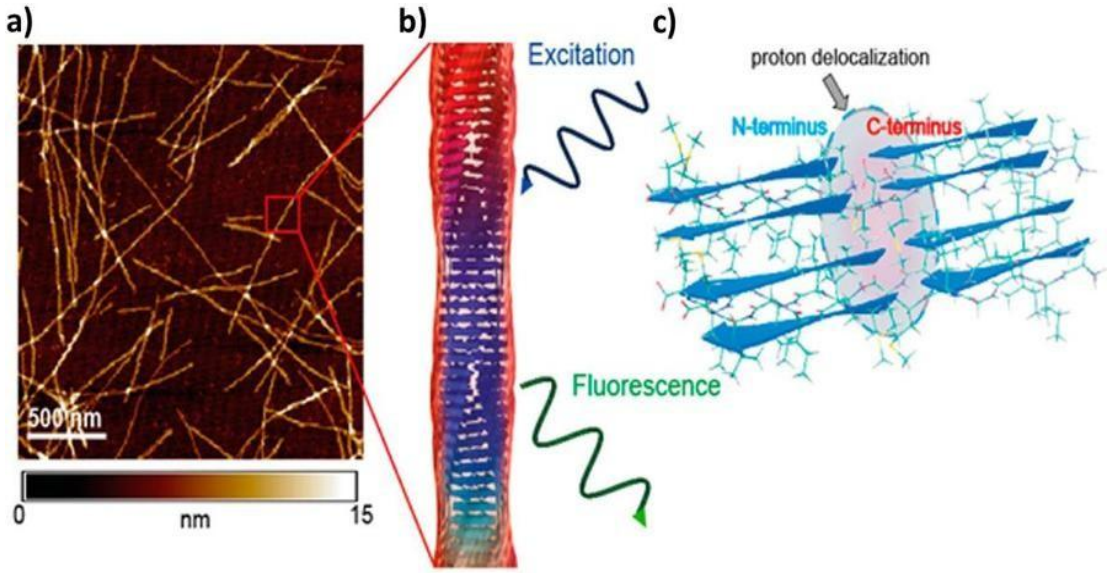

Figure 1.18: Structural arrangements of Aβ (AIIGLM). (a) AFM image (b) Schematic view of the 3D peptide arrangement in a protein fibril stacked by β-strands. (c) Cross-section of the magnified section from same two adjacent protofilaments. The shaded ellipsoid depicts predicted proton transfer. (Adapted from Pinotsi et al., 2016).

Jong et al. (2019) demonstrated the involvement of charge transfer in the absorbance and luminescence observed from amyloid fibrils. They conducted spectroscopic measurements and computational studies on fibrils formed from Aβ-derived oligopeptides. Time-dependent density functional theory (TDDFT) calculations were performed on three possible dimer configurations of a protofilament: linear parallel (a), anti-parallel (b), and parallel (c), as shown in Figure 1.19(left). Charge transfer was observed at the dimer termini, with the direction, oscillator strength, and location of charge transfer corresponding to the lowest energy excitation depicted in Figure 1.19 (right). In these configurations, the electron and hole situated on the N- and C-terminus are shown in red and blue, respectively, along with the direction of charge transfer. Thus, charge transfer transitions have been reported at the termini of amyloid fibrils.

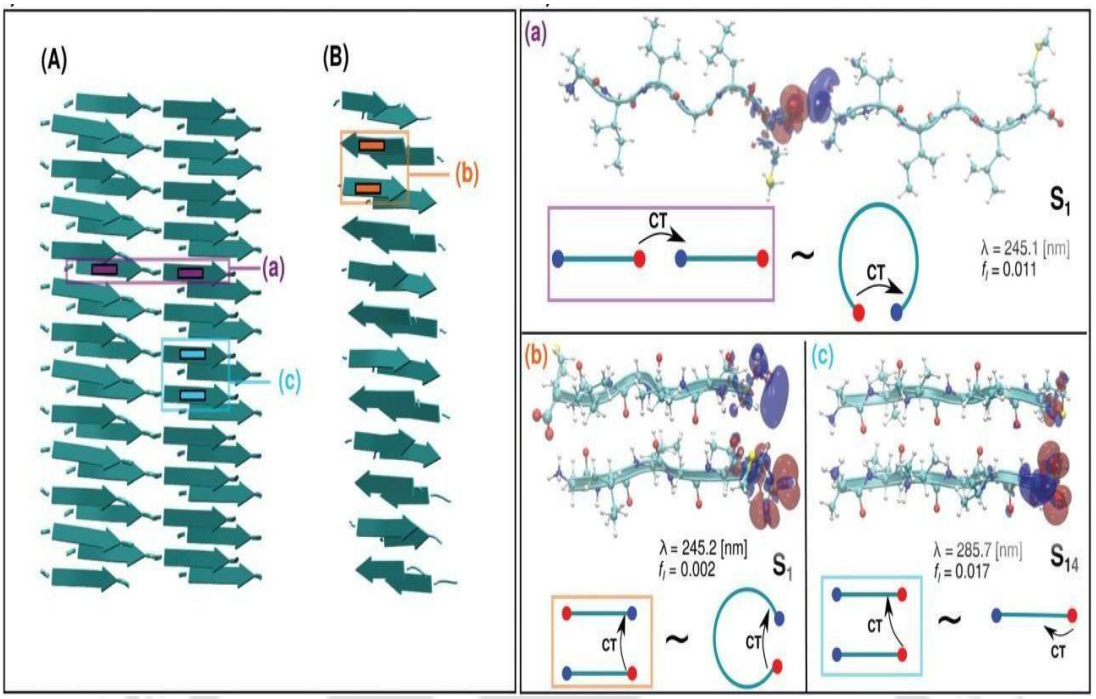

Figure 1.19: Charge transfer at the termini of amyloid fibrils formed from Aβ derived oligopeptides. (Adapted from Jong et al., 2019).

1.7.1 Monitoring Aggregation using ProCharTS

ProCharTS was utilized to monitor the aggregation behavior of hen egg-white lysozyme (HEWL) under previously established pH conditions (Figure 1.20). At different pH (pH 2, 5 and 12.2), a notable increase in ProCharTS absorption intensity was observed in the aggregates, correlating with higher initial monomer concentrations [Ansari et al., 2018]. This suggested that elevated monomer levels promote more extensive aggregation, leading to enhanced interactions among charged residues within the aggregates.

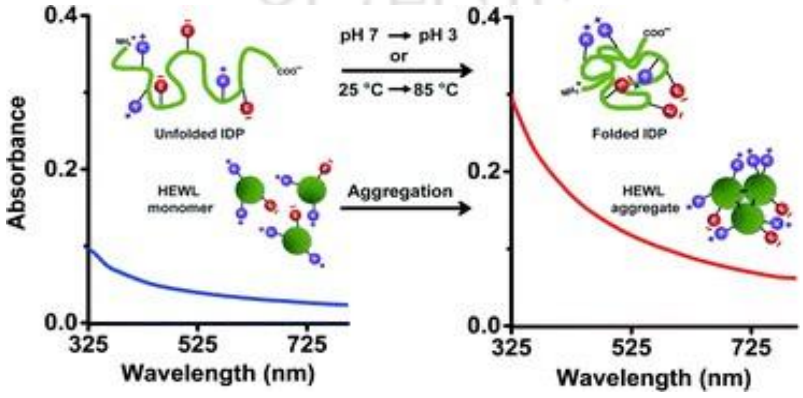

Figure 1.20: Schematic illustration of aggregation detection using ProCharTS. (Ansari et al.

2018).

Apart from this, Alom et al (2024) employed ProCharTS absorbance and luminescence measurements to detect the early stages of Aβ-derived Switch Peptide aggregation, benchmarking its performance against established techniques such as circular dichroism (CD), 1-anilinonaphthalene-8-sulfonate (ANS) fluorescence, and the Thioflavin T (ThT) assay. The findings revealed that increase in ProCharTS absorbance and luminescence effectively signaled the onset of aggregation (Figure 1.21). These changes showed strong correlation with traditional indicators, including alterations in CD spectra and enhanced ANS fluorescence, underscoring ProCharTS as a sensitive tool for monitoring early aggregation events [Alom et al., 2024].

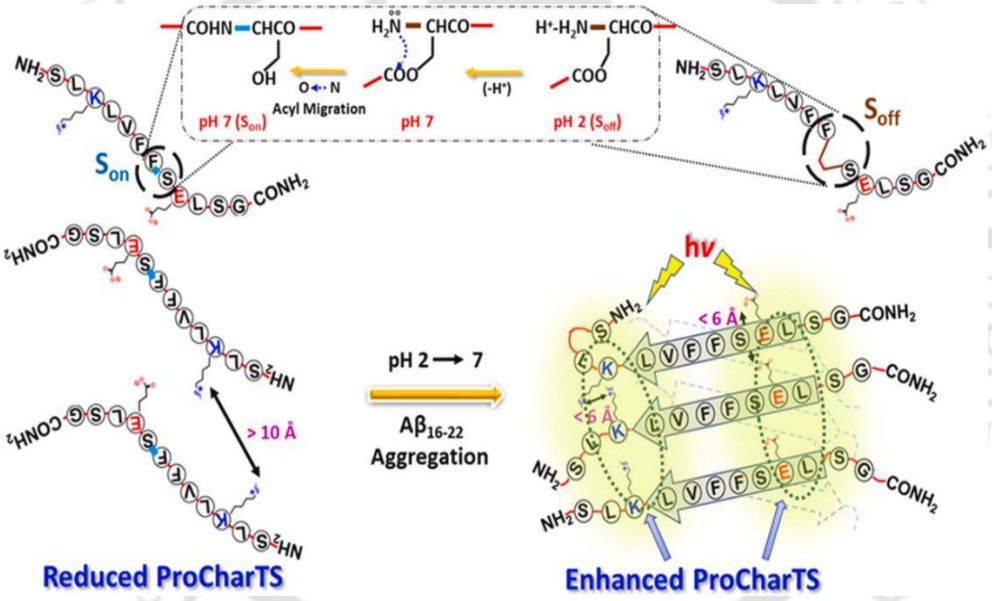

Figure 1.21: Illustration of detection of aggregation in Aβ switch peptides using ProCharTS (Adapted from Alom et al., 2024).

Hence, ProCharTS presents a promising alternative for monitoring the early stages of aggregation, despite its distinct mechanism compared to conventional techniques. Its key advantages include: (a) being a label-free and non-invasive approach that does not interfere with the aggregation process, (b) ease of use, requiring only standard instruments like a spectrophotometer and fluorimeter, and (c) high sensitivity to the initial formation of oligomers, that bring charged residues in proximity.

However, to establish ProCharTS as a robust tool for studying amyloid kinetics, further

investigations across a broader range of aggregation-prone proteins are essential. Additionally, ProCharTS can be employed to screen potential drug candidates targeting the early phases of amyloid aggregation. The intrinsic luminescence of fibrils detected via ProCharTS may also be waveguided for advanced biomedical imaging, paving the way for future applications in diagnostics and therapeutics.

1.8 Protein unfolding: A phenomenon both beneficial and fatal

The misfolding of amyloidogenic proteins is a pivotal factor in the development of neurodegenerative diseases such as Alzheimer's and Parkinson's. To date, over 35 proteins, including amyloid-β and α-synuclein, have been identified as capable of forming amyloid fibrils in humans under specific conditions. These fibrils are distinguished by their structured filaments composed of cross β-sheets formed between the main chains of constituent polypeptides [Dobson, 2003]. Among the various aggregated species, soluble oligomers (pre-fibrillar aggregates) are considered the most toxic. These oligomers can assemble into protofilaments, which subsequently aggregate to form mature amyloid fibrils. In familial forms of neurodegenerative diseases, mutations that increase the hydrophobicity of amyloid-forming proteins or render nascent proteins more susceptible to proteolysis and truncation have been identified. Consequently, within a cellular environment, a nascent polypeptide may follow multiple pathways: proper folding, degradation due to misfolding or truncation, or the formation of toxic amyloid fibrils.

Protein unfolding is a critical prerequisite for directing proteins toward the ubiquitin-mediated proteasome degradation pathway (Figure 1.21). Additionally, protein unfolding is essential for the translocation of proteins into subcellular organelles such as mitochondria [Prakash et al., 2004]. The involvement of protein unfolding in these fundamental cellular processes, as well as its role in the formation of pathogenic amyloid fibrils, underscores the importance of understanding protein misfolding and aggregation phenomena.

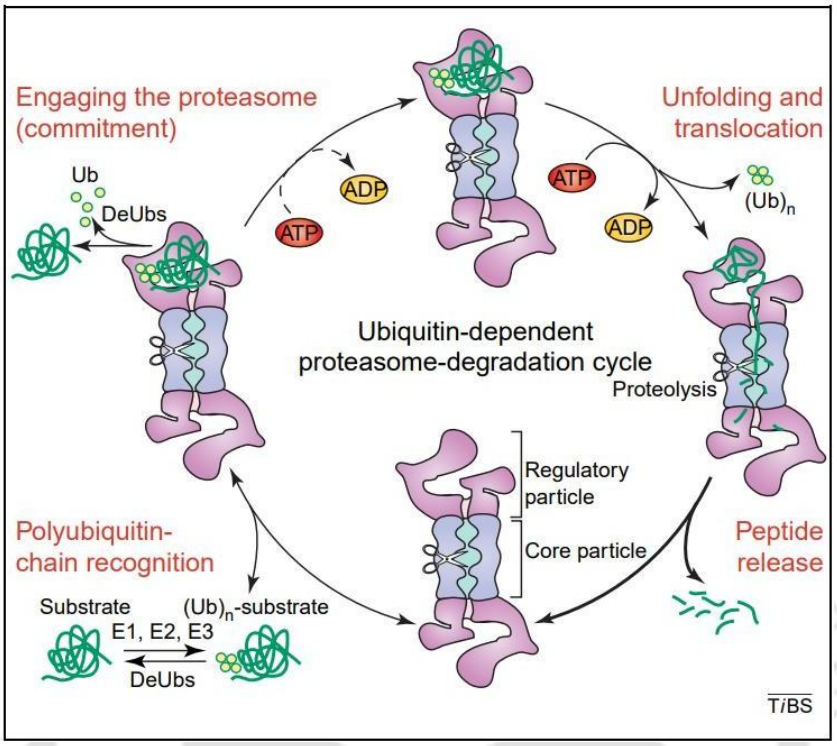

Figure 1.22: The degradation cycle of the proteasome. Polyubiquitinated (Ubn) proteins bind to the proteasome through the ubiquitin chain (bottom left). Unfolding and degradation (top right) ensue only after the substrate has engaged the proteasome through an unstructured domain or the degradation initiation site (top left). Once the substrate is engaged, it is degraded sequentially along the polypeptide chain from its degradation initiation site (bottom right). (Prakash et al., 2004).

Intrinsic chromophores like tryptophan (Trp) and tyrosine (Tyr), along with extrinsic probes such as 8-anilino-1-naphthalenesulfonate (ANS) and dansyl, serve as indirect indicators for monitoring polypeptide collapse during protein folding studies [Plaxco et al., 1996, Agashe et al., 1995]. Upon protein unfolding, Trp and dansyl exhibit decreased fluorescence intensity and a red shift in emission maxima, attributed to increased solvent exposure and relaxation effects. This red shift is indicative of the fluorophore transitioning from a hydrophobic core to a more hydrophilic environment [Lakowicz, 2006]. Additionally, such spectral changes were utilized to monitor protein unfolding. Furthermore, Trp–dansyl

Förster Resonance Energy Transfer (FRET) has been employed in previous research to demonstrate nonspecific hydrophobic collapse preceding secondary structure formation in barstar folding [Agashe et al., 1995]. An increase in Trp–dansyl FRET upon refolding of

guanidine hydrochloride-denatured acyl-CoA binding protein (ACBP) has also been used to identify early folding intermediates, underscoring the utility of extrinsic chromophores in studying protein folding dynamics [Teilum et al., 2002].

At sub-denaturing concentrations of guanidine hydrochloride (GdnHCl), human serum albumin (HSA) exhibits a molten globule-like intermediate state during unfolding [Kumar et al., 2004]. This state is characterized by increased binding of the hydrophobic dye 8-anilino-1-naphthalenesulfonate (ANS), with maximal fluorescence observed between 0.5 and 2.5 M GdnHCl, indicating exposure of hydrophobic regions (Figure 1.23) [Ahmad et al., 2005]. Despite these changes, the protein retains its native-like secondary structure, as evidenced by minimal alterations in mean residue ellipticity at 222 nm. These findings underscore the presence of a partially unfolded, yet structurally preserved, molten globule state in HSA under mild denaturing conditions.

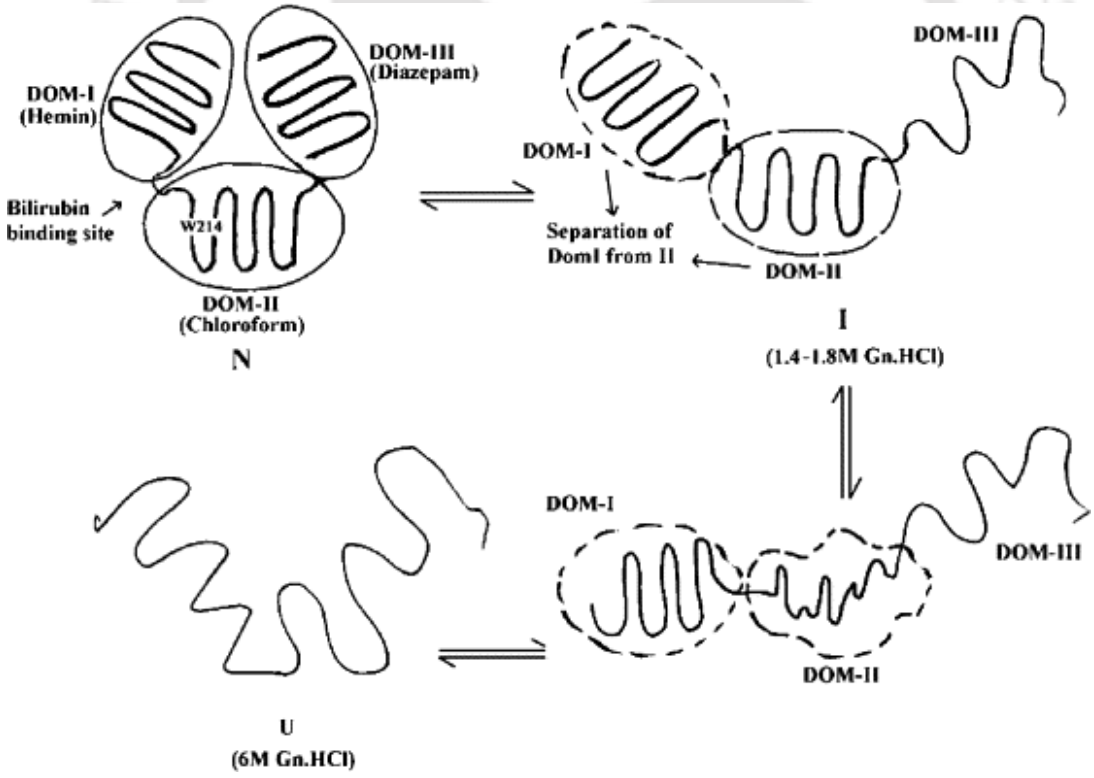

Figure 1.23: A pictorial model representing the mechanism of GdnHCl induced unfolding of HSA. (Adapted from Ahmad et al., 2005).

Linear infrared (IR) spectroscopy, particularly through the analysis of the amide I band, arising from backbone carbonyl stretching vibrations, serves as a powerful tool to investigate

protein folding dynamics on picosecond timescales. The sensitivity of this band to protein secondary structures allows for the characterization of folding intermediates. Time-resolved IR techniques, such as temperature-jump (T-jump) IR spectroscopy, have been employed to study the folding processes of structural motifs like helix–turn–helix and β-hairpins. These studies have revealed that the formation of turn regions is the rate-limiting step in the folding of these structures [Serrano et al., 2012].

Time-resolved fluorescence resonance energy transfer (TR-FRET) has been employed to monitor intermediates during apomyoglobin refolding, revealing the heterogeneity of its folding pathway. This technique allows for the detection of transient conformational states by measuring energy transfer between fluorescent probes strategically placed within the protein structure [Rischel et al., 1995].

To obtain precise information about the molecular dimensions of these transient conformations, complementary techniques such as small-angle X-ray scattering (SAXS) and dynamic light scattering (DLS) are utilized. SAXS provides insights into the overall shape and size of macromolecules in solution by measuring the scattering of X-rays at small angles, yielding parameters like the radius of gyration (Rg) [Plaxco et. al, 1996]. DLS, on the other hand, analyzes fluctuations in scattered light intensity due to Brownian motion, offering measurements of the hydrodynamic radius (Rh) of particles in solution. Together, these methods contribute to a comprehensive understanding of protein folding dynamics by characterizing the size and shape of folding intermediates.

Various techniques are available to study protein folding and unfolding processes. Conventional methods, such as chemical denaturation, thermal denaturation, and pressure-induced unfolding, each have unique sensitivities to different aspects of protein structure, leading to variations in the characterization of unfolding pathways. These differences arise due to the inherent heterogeneity in protein unfolding mechanisms and the specific structural features each method probes. Therefore, while novel techniques may provide new insights into protein dynamics, it is essential to benchmark their findings against established conventional methods to ensure consistency and accuracy in interpreting protein folding behaviors.

1.8.1 Monitoring protein unfolding using ProCharTS

Priyadarshi et al. (2023) showed that upon unfolding, proteins predominantly composed of α-helices such as human serum albumin (HSA), α_3W, and α_3C, transition into random coil conformations. This structural transformation can be effectively monitored using Protein Charge Transfer Spectroscopy (ProCharTS), which detects alterations in the proximity of charged residues within the protein's three-dimensional structure (Figure 1.24). ProCharTS absorbance increases at lower guanidine hydrochloride (GdnHCl) concentrations, indicating the early formation of molten globule-like intermediates during the unfolding process. In contrast, intrinsic fluorescence probes like tryptophan (Trp) and extrinsic probes such as dansyl are sensitive to local environmental changes, particularly solvent polarity.

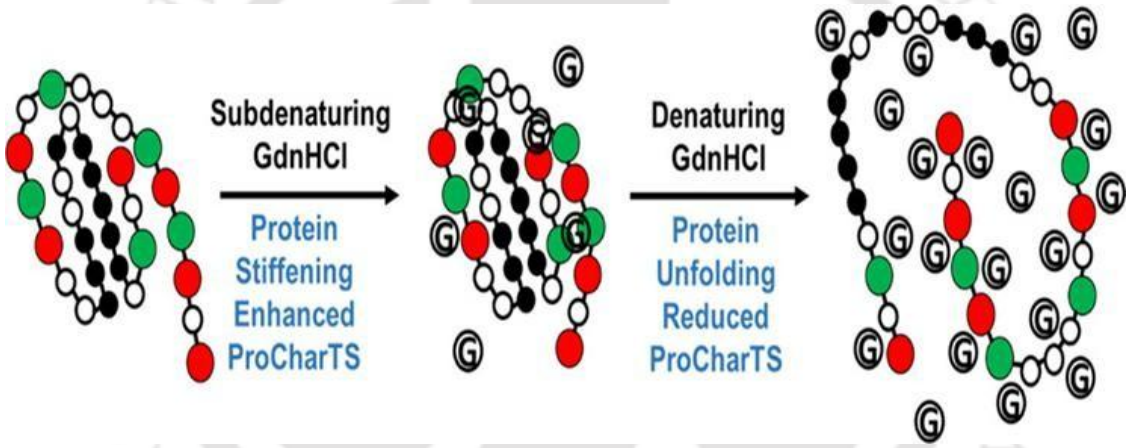

Figure 1.24: Illustration of protein stiffening at sub denaturing and protein unfolding at higher GdnHCl concentrations. Model depicting the hydrophobic amino acids as filled circles, hydrophilic amino acids as unfilled circles, negatively charged amino acids as red circles, positively charged amino acids as green circles, and GdnHCl as circles with alphabet G (Priyadarshi et al., 2023).

Protein Charge Transfer Spectroscopy (ProCharTS) is highly sensitive to the disruption of spatial proximities among charged amino acid residues, which are predominantly located on the protein surface. This sensitivity enables ProCharTS to detect early structural changes during protein unfolding, as alterations in the arrangement of these charged residues significantly affect the protein's charge transfer absorption spectra [Priyadarshi et al. 2024].

1.9 Objectives of the thesis work

Owing to the unique intrinsic absorbance and luminescence characteristics exhibited by unconventional chromophores, there is a compelling need to further explore the spectral origins of these systems and clarify the roles played by the involved chromophores. Nonetheless, the scope of our research has been limited to unconventional chromophores present in proteins. Gaining insights into these chromophores offers biophysicists a novel perspective on the optical behavior of proteins. These distinctive, label-free intrinsic probes hold promise for application not only in apoproteins but also in other protein systems, regardless of whether they exist in monomeric or oligomeric forms.

The core focus of my thesis lies in deciphering the optical properties of these unconventional chromophores and exploring their potential applications across various biophysical contexts. The primary objectives of this doctoral research are outlined below, with detailed discussions of each topic presented in the subsequent sections.

Thesis objectives:

1. **Investigating effect of Phosphorylation on Synthetic Peptides and Casein Proteins Using ProCharTS.**
2. **Investigating the Impact of Protein Aggregation on ProCharTS Using Alpha-Synuclein and Human Lysozyme proteins.**
3. **Monitoring Unfolding of proteins, ERK2 and Human Lysozyme using ProCharTS.**

1.10 Thesis at a glance

The thesis, titled "Investigating applications of Protein Charge Transfer Spectra (ProCharTS) in peptides and proteins," was undertaken to address three primary objectives. The core components of the thesis, including the literature review, experimental methodologies, and the specific aims of the research are outlined in Figure 1.25.

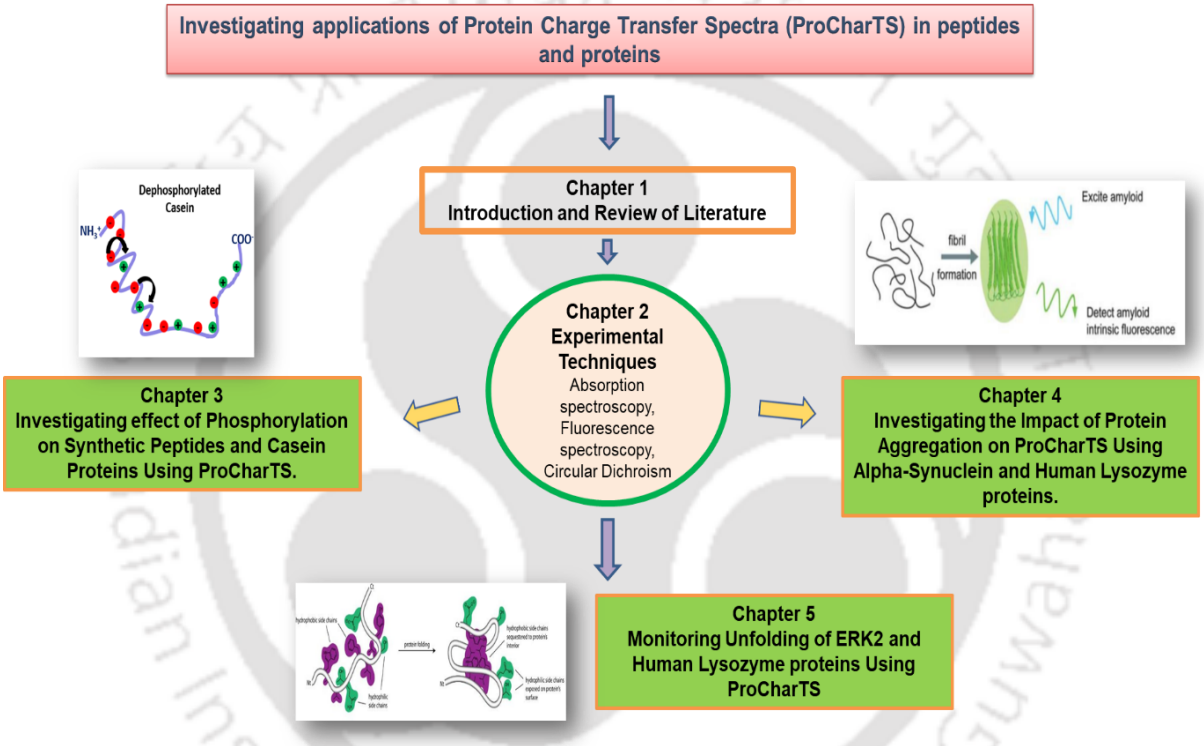

Figure 1.25: Thesis at a glance.

CHAPTER 2:

EXPERIMENTAL TECHNIQUES USED; MATERIALS AND METHODS

2.1 Experimental techniques

This section primarily outlines the key experimental techniques employed throughout the doctoral research. The core methods include UV-Visible Absorption Spectroscopy, Fluorescence Spectroscopy, Circular Dichroism, Matrix Assisted Laser Desorption/Ionization and Size Exclusion Chromatography. These techniques form the foundation of the experimental work presented in the thesis and are each briefly described under separate headings.

2.1.1 Spectroscopy

Spectroscopy refers to the study of how light interacts with matter [Cid & Bravo, 2014; Knowles, 1985]. Light, being a rapidly oscillating electromagnetic field, can perturb the charge and spin distributions within a molecule upon exposure. These perturbations may alter the molecule's electrical and magnetic properties [Hof, 2003]. Such changes are often detectable through the characteristics of the radiation emitted or transmitted by the sample. One of the most basic measurements in spectroscopy is the amount of incident light absorbed by the sample, which forms the foundation for techniques like optical absorption spectroscopy and Nuclear Magnetic Resonance (NMR) spectroscopy. In addition to absorption, the emission of radiation at wavelengths different from the excitation source can also be studied. This phenomenon underpins methods such as fluorescence, phosphorescence, and Raman scattering. Furthermore, techniques like fluorescence polarization and circular dichroism rely on analyzing the type and extent of polarization in the emitted radiation [Cantor and Schimmel, 1980].

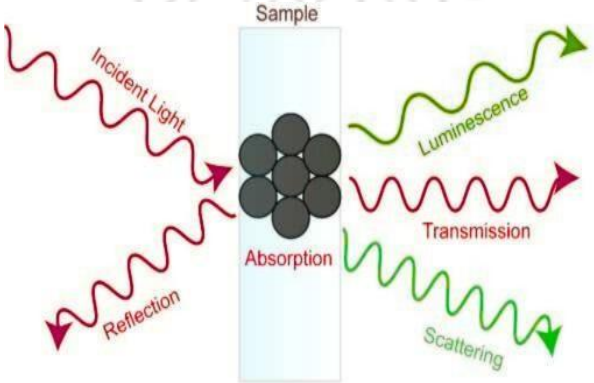

Figure 2.1: Schematic showing interaction of light with matter.

It is important to note that the energy of incident light directly influences the type of perturbation it induces within a molecule. For instance, radiation with energies ranging from 3×10^{0} to 3×10^{-2} kcal/mol is typically sufficient to alter vibrational and rotational energy levels. In contrast, energies between 10^{2} and 50 kcal/mol can affect electronic energy levels. In the context of biological systems, specific wavelengths are employed to probe distinct molecular features, each detected using an appropriate spectroscopic technique. Table 2.1 outlines various spectroscopic regions relevant to biological studies along with the corresponding techniques [Cantor and Schimmel, 1980].

Typical Wavelength (cm)	Approx. Energy (kcal mole^{-1})	Spectroscopic Region	Techniques and Applications
1×10^{-11}	3×10^{8}	γ-Ray	Mössbauer
1×10^{-8}	3×10^{5}	X-Ray	X-ray diffraction, scattering
1×10^{-5}	3×10^{2}	Vacuum UV	Electronic spectra
3×10^{-5}	1×10^{2}	Near UV	Electronic spectra
6×10^{-5}	5×10	Visible	Electronic spectra
1×10^{-3}	3×10^{0}	IR	Vibrational spectra
1×10^{-2}	3×10^{-1}	Far IR	Vibrational spectra
1×10^{-1}	3×10^{-2}	Microwave	Rotational spectra
1×10^{0}	3×10^{-3}	Microwave	Electronic paramagnetic resonance
1×10^{1}	3×10^{-4}	Radio frequency	Nuclear magnetic resonance

Table 2.1: Biologically useful spectroscopic regions. (Adapted from Cantor and Schimmel 1980).

UV-Visible absorption and fluorescence spectroscopy are commonly employed to study protein structure and function, often in conjunction with other analytical techniques such as nuclear magnetic resonance (NMR), Fourier-transform infrared (FTIR) spectroscopy, and circular dichroism (CD) spectroscopy.

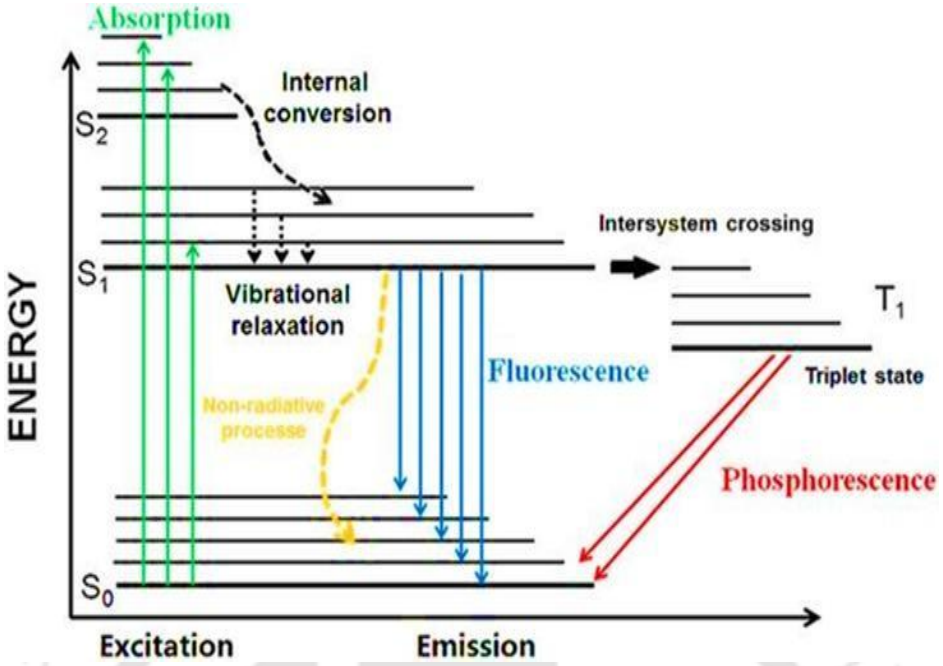

Figure 2.2: Jablonski diagram depicting the absorption and emission of light (Adapted from Lakowicz, 2013)

The absorbance and emission of UV-Visible light by a molecule can be understood using a Jablonski diagram. Figure 2.2 presents such a diagram, depicting the electronic states and their associated vibrational levels for a typical fluorophore. It illustrates the molecular events involved in photon absorption and emission. Photon absorption occurs on a femtosecond timescale and follows the Franck–Condon principle, meaning it takes place without any nuclear rearrangement. At room temperature, both absorption and emission typically originate from the lowest vibrational levels of the respective electronic states.

Following photon absorption, an electronic transition occurs from the lowest vibrational level of the ground state (S_0) to one of the vibrational levels of an excited singlet state (S_1 or S_2). Emission of light either as fluorescence (from S_1) or phosphorescence (from T_1) occurs as the molecule returns to the ground state, releasing a photon of lower energy than the one initially absorbed. In addition to these radiative processes, several non-radiative processes may take place, including internal conversion, intersystem crossing, vibrational relaxation, and fluorescence quenching.

2.1.1.1 Absorption spectroscopy

In biological studies, absorption spectroscopy typically focuses on the interaction of visible or ultraviolet radiation with biomolecules. The absorption of a photon is an extremely rapid process, occurring within approximately 10^{-15} seconds [Lakowicz, 2013]. When light is absorbed, it perturbs the energy levels of the molecule, promoting electrons from the ground state to one of the many rotational-vibrational energy levels within the first excited electronic state (S_1) [Cantor and Schimmel, 1980].

The energy gap between the electronic states S_0 and S_1 is typically around 80 kcal mol^{-1}. In contrast, the spacing between vibrational levels is approximately 10 kcal mol^{-1}, and between rotational levels, about 1 kcal mol^{-1}. Consequently, at room temperature, nearly all molecules in a solution occupy the lowest electronic state, S_0, with the lowest vibrational levels and many rotational levels being populated. Due to the quantized nature of these energy levels, molecular excitation occurs only when light of a frequency matching the energy gap between two specific energy levels is absorbed.

The total energy of a molecule is the sum of its electronic, vibrational, and rotational energy levels. Rotational energy levels are primarily relevant in the gas phase, where molecules can freely rotate. In condensed phases, rotational motion is significantly restricted, and vibrational energy levels become broadened, making them less distinct.

Absorptivity is an intrinsic property of a chromophore and remains constant at a given wavelength. When a photon of light interacts with a chromophore that possesses quantized electronic states, it can be absorbed, transferring its energy to an electron. This energy enables the electron to undergo an electronic transition, as described by:

$$E_{photon} = \Delta E_{electronic\ transition} = h\nu$$

In classical electromagnetism, the interaction energy between a dipole and an electric field is expressed as the dot product of the dipole moment vector with the electric field vector.

$$\text{Energy} = \vec{E} \cdot \vec{\mu} \qquad (2.1)$$

The dipole moment is defined as the vector sum obtained by multiplying each charge q_j by its corresponding position vector r_j , summed over all charged particles j.

$$\mu = \sum_j q_j r_j \qquad (2.1.1)$$

When molecules interact with light, their quantum states can change. For instance, a molecule initially in state 'a' may transition to a different state 'b' due to this interaction. This change arises from a redistribution of the molecule's electric charge in response to the oscillating electric field *E* of the light. The likelihood of this transition from state 'a' to state 'b' is determined by the transition dipole moment, denoted as $\mu_{ba} = \langle\psi_b|\tilde{\mu}|\psi_a\rangle$ where ψ_a and ψ_b represent the wavefunctions of the respective states. The strength of light absorption is directly related to the rate at which the molecule absorbs energy from the incident electromagnetic radiation.

Transition rate (dP_b/dt) is product of two terms and can be written as

$$dP_b/dt = B_{ab} I(\nu) \qquad (2.2)$$

Here, B_{ab} is the transition rate per unit energy density and *I (ν)* denote the energy density incident on the molecule. B_{ab} can be written as

$$B_{ab} = (2/3)\,(\pi/\hbar^2)\,|\langle\psi_b|\tilde{\mu}|\psi_a\rangle|^2 \qquad (2.3)$$

The molar extinction coefficient is related to Einstein coefficient for stimulated absorption as

$$B_{ab} = (1000c/N_0\,h)\int(\varepsilon'/\nu)\,d\nu \qquad (2.4)$$

where N_0 is Avogadro's number, c is the velocity of the light, ε' is molar extinction coefficient and ν is frequency of light.

Using the equation 2.3 and 2.4, and converting ε' to ε ($\varepsilon = \varepsilon'/2.303$), the following relationship can be obtained

$$|\langle\psi_b|\tilde{\mu}|\psi_a\rangle|^2 = 9.180 \times 10^{-3} \int(\varepsilon'/\nu)\,d\nu = D_{ab}\ (\text{debye}^2) \qquad (2.5)$$

The quantity D_{ab} represents the dipole strength, which quantifies the magnitude of the transition dipole moment between states 'a' and 'b'. Another important parameter is the oscillator strength, f_{ab} , which provides a dimensionless measure of absorption intensity by comparing it to that of an ideal three-dimensional harmonic oscillator. It serves as a useful indicator of how strongly a molecule absorbs light during the transition.

$$f_{ab} = (8\pi^2 mc/3hv)\, D_{ab} = 4.315\times10^{-9} \int \varepsilon\,(\bar{v})d\bar{v} \quad \text{(dimensionless)} \qquad (2.6)$$

Here, m denotes the mass of the electron and $\bar{v}$ is wavenumber. For strongly allowed transitions, the oscillator strength f_{ab} typically ranges between 0.1 and 1. Both f_{ab} and the dipole strength D_{ab} are essential parameters for interpreting the unique optical phenomena exhibited by polymers.

Absorbance refers to the amount of light absorbed by a sample and is commonly measured using spectroscopy, especially for quantitative analysis. A typical spectrometer setup is illustrated in Figure 2.3 below.

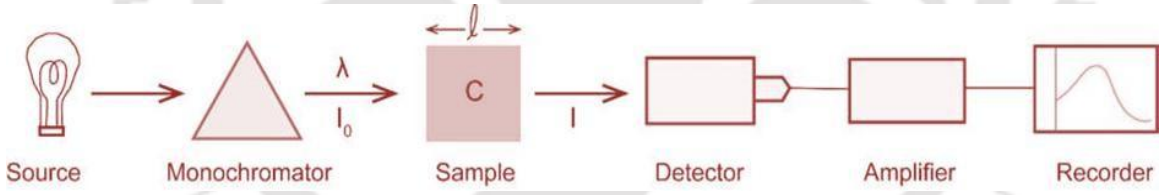

Figure 2.3: Schematics of UV-Visible spectroscopic set up. (Adapted from Cantor & Schimmel, 1980)

When the light with intensity I_o, incident on the sample in a section sufficiently thin section (dl) having total path length 'l' (in cm) with a molar extinction coefficient of ε (M^{-1} cm^{-1}) and concentration 'C', then the fraction of incident light absorbed by chromophores in the sample is given by:

$$-\frac{dI}{I} = C\varepsilon' dl \qquad (2.7)$$

Integrated the equation 2.7, we get-

$$A(\lambda) = log\frac{I_o}{I} = C\varepsilon(\lambda)l \qquad (2.8)$$

Equation 2.8 represents the Beer-Lambert Law, which states that the amount of light absorbed by a sample is directly proportional to the concentration of the absorbing species, the path length of the sample holder (cuvette), and the molar extinction coefficient.

The absorption cross-section of molecules and the extinction coefficient are closely related. Consider a thin slab of solution with a surface area *A* (in cm²) and thickness *dl*. If the solute concentration is *C*, the number of solute molecules per cm³ is $CN_0/1000$ where N_0 is Avogadro's number.

Thus, the total number of solute molecules within the slab is $CAN_0dl/1000$. Assuming each solute molecule has a radius r, the fraction of the slab's cross-sectional area occupied by these molecules is represented by f_{max}, as illustrated in Figure 2.4.

$$f_{max} = (\pi r^2 CAN_0 dl/1000)/Adl = \pi r^2 CN_0/1000 \quad (2.9)$$

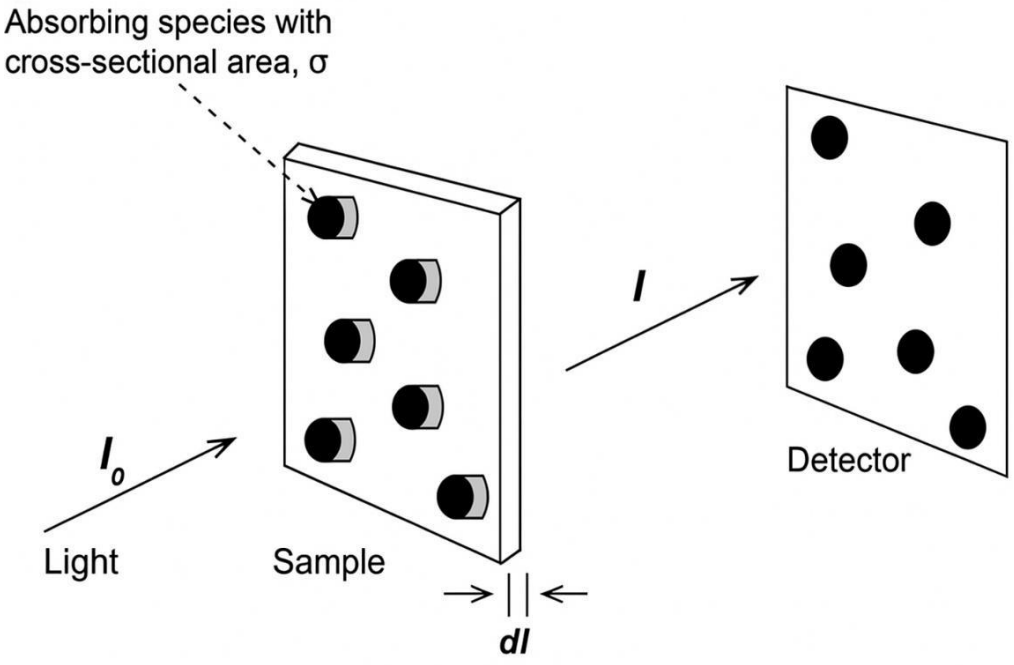

Figure 2.4: Illustration of light absorption by molecules within a very thin layer of sample. (Adapted from Cantor and Schimmel 1980).

If the probability that the sample absorbs incident light is denoted by P, then the total fraction of light absorbed can be expressed as $f_{max}P$. The corresponding contribution from each individual molecule to this absorption is then given by:

$$\sigma = P\pi r^2 \tag{2.10}$$

In this context, σ represents the molecular absorption cross-section. The fraction of light absorbed can therefore be expressed in terms of this cross-section as follows:

$$\frac{dI}{I} = (\sigma C N_0/1000)dl \tag{2.11}$$

With the above equations 2.7 and 2.8, it can easily be shown that

$$\varepsilon = (\sigma C N_0/1000)/2.303\mathrm{C} = \sigma N0/2303 \tag{2.12}$$

which can be computed to obtain σ.

$$\sigma = 3.825 \times 10^{-21}\ \varepsilon\ (\mathrm{cm}^2) \tag{2.13}$$

The equation above establishes a link between the molecular cross-section and the extinction coefficient. Additionally, it highlights that the extinction coefficient remains unaffected by the concentration of the sample.

2.1.1.2 Fluorescence Spectroscopy

Fluorescence is a relaxation process wherein a fluorophore emits ultraviolet or visible light following the absorption of incident radiation. This phenomenon corresponds to the transition of an electron from the first excited singlet state (S_1) back to the ground singlet state (S_0), accompanied by the release of a photon with lower energy than the absorbed light. The emission occurs on a nanosecond timescale and, in proteins, primarily involves aromatic amino acids such as tryptophan (Trp). In contrast to absorption, which occurs on a femtosecond scale, fluorescence is slower and therefore more sensitive to environmental

factors such as solvent accessibility, protein rotational dynamics, and diffusion of quenchers.

2.1.1.2.1 Factors that affect fluorescence intensity:

A. Internal Conversion

During internal conversion, a fluorophore rapidly relaxes from higher vibrational levels of excited states (such as S_2 or S_1) to the lowest vibrational level of S_1. This energy loss occurs through molecular collisions with the solvent or other molecules, or via internal vibrational pathways. Internal conversion typically occurs in less than 10^{-12} seconds. Both internal conversion and vibrational relaxation contribute to an increase in the solvent's temperature. The rate of internal conversion (k_{ic}) is temperature-dependent, increasing with rising temperature. Consequently, elevated temperatures lead to reduced fluorescence intensity. This intrinsic temperature sensitivity complicates the monitoring of heat-induced conformational changes in macromolecules.

B. Quenching

Fluorescence quenching refers to any process that leads to a reduction in the fluorescence intensity of a fluorophore. This typically occurs when the excited fluorophore interacts with a quencher molecule (Q), resulting in non-radiative deactivation of the excited state. Such interactions may involve transient collisions or stable complex formation. Common collisional quenchers include oxygen, amines, halogens, and acrylamide, all of which can effectively depopulate the excited state. The rate of quenching via collisions is diffusion-limited, and when driven by such encounters, the process follows bimolecular kinetics.

$$S_b + Q \xrightarrow{k_q} S_a + Q + \text{Heat} \qquad (2.14)$$

Here, S_a and S_b represent the ground and excited electronic states of the molecule, respectively. Q denotes the quencher, and k_q is the bimolecular quenching rate constant. Since the concentration of the quencher is much higher than that of the excited-state species S_b, the quenching process follows pseudo first order kinetics. By systematically varying the quencher concentration [Q], the value of k_q can be experimentally determined.

C. Intersystem Crossing

A fluorophore in the excited singlet state (S_1) may undergo a spin-state transition to the excited triplet state (T_1), a process known as intersystem crossing. The triplet state can then return to the ground singlet state (S_0) via phosphorescence or internal conversion. Emission from the triplet state occurs at longer wavelengths and lower energy compared to singlet emission. The likelihood of intersystem crossing increases when vibrational levels of the singlet and triplet states overlap. Since the transition from T_1 to S_0 is spin-forbidden, the triplet state typically has a much longer lifetime (~ 10^{-3} s) than the singlet excited state (about 10^{-9}). Molecules containing heavy atoms often exhibit phosphorescence, as the presence of heavy atoms enhances intersystem crossing through spin orbit coupling.

For a fluorophore where both the non-radiative as well as the radiative process occurs, the rate of fluorescence significantly decreases, and the observed fluorescence lifetime (τ) is expressed as-

$$\tau_F = \frac{1}{k_r + k_{isc} + k_{ic} + k_q[Q]} \qquad (2.15)$$

where k_r, k_{isc} and k_{ic} represent the rate of the radiative decay, intersystem crossing, internal conversion. k_q and $[Q]$ represent the fluorescence quenching rate and molar quencher concentration. The above equation can be simplified by combining all the rates of non-radiative decay processes as k_{nr}.

$$\tau_F = \frac{1}{k_r + k_{nr}} \qquad (2.16)$$

Since the fluorescence efficiency or the quantum yield (ϕ) is defined as

$$\phi = \frac{k_r}{k_r + k_{isc} + k_{ic} + k_q[Q]} = \frac{k_r}{k_r + k_{nr}} \qquad (2.17)$$

The natural lifetime (τ_n) of a fluorophore is defined as the case where no non-radiative process occurs and can be represented as-

$$\tau_n = \frac{1}{k_r} \tag{2.18}$$

Combining equations 2.16, 2.17 and 2.18:

$$\Phi = \frac{\tau_F}{\tau_n} \tag{2.19}$$

This equation represents that quantum yield decreases with decreases in fluorescence intensity caused by non-radiative processes.

2.1.1.2.2 Distinctive traits of fluorescence

Fluorescence relies on two key photophysical traits:

A) Stokes shift: The fluorescent emission always occurs at a lower energy (longer wavelength) than the absorption. This energy difference, the shift between the absorption peak and the emission peak, is known as the Stokes shift, which arises from internal conversion and solvent relaxation processes (Figure 2.5).

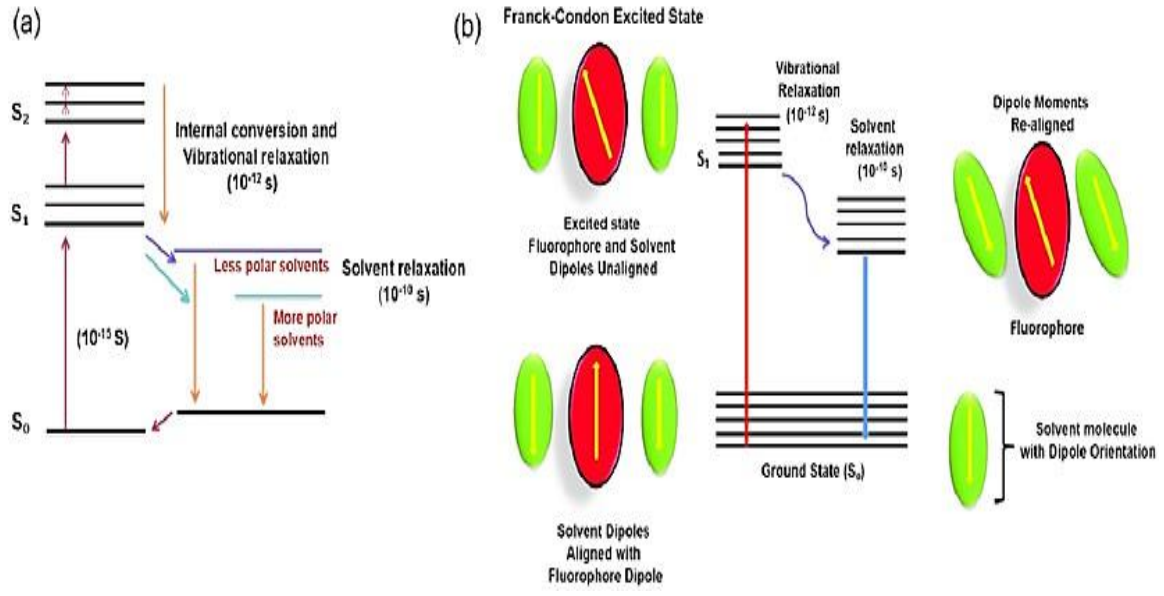

Figure 2.5: (a) Jablonski diagram for fluorescence with solvent relaxation and (b) fluorophore-

solvent excited state interaction (Nidhisha et al., 2024).

B) Excitation-independent emission (Kasha's rule): Regardless of which wavelength is used to excite a fluorophore, the shape and wavelength of its emission spectrum remain the same. This happens because emission always originates from the lowest vibrational level of the first excited singlet state (S_1), meaning that any higher-state excitations (e.g. S_2) first relax down via non-radiative processes before fluorescence occurs.

2.1.1.2.3 Steady State fluorescence

In steady-state fluorescence, the sample is continuously exposed to light of a specific wavelength, and the emitted fluorescence is recorded as a function of wavelength. During this process, an equilibrium is established between the ground-state and excited-state populations of the fluorophores. This technique yields time-averaged information about the behavior of fluorophores in the excited state. It enables a wide range of experiments, such as recording excitation and emission spectra, determining quantum yield, studying fluorescence quenching, Förster Resonance Energy Transfer (FRET), and measuring steady- state fluorescence anisotropy, among others. Additionally, changes in fluorescence intensity and emission maxima offer insights into the local environment of the fluorophore, such as solvent exposure and polarity factors that are relevant to the investigation of biological processes like protein folding and conformational transitions.

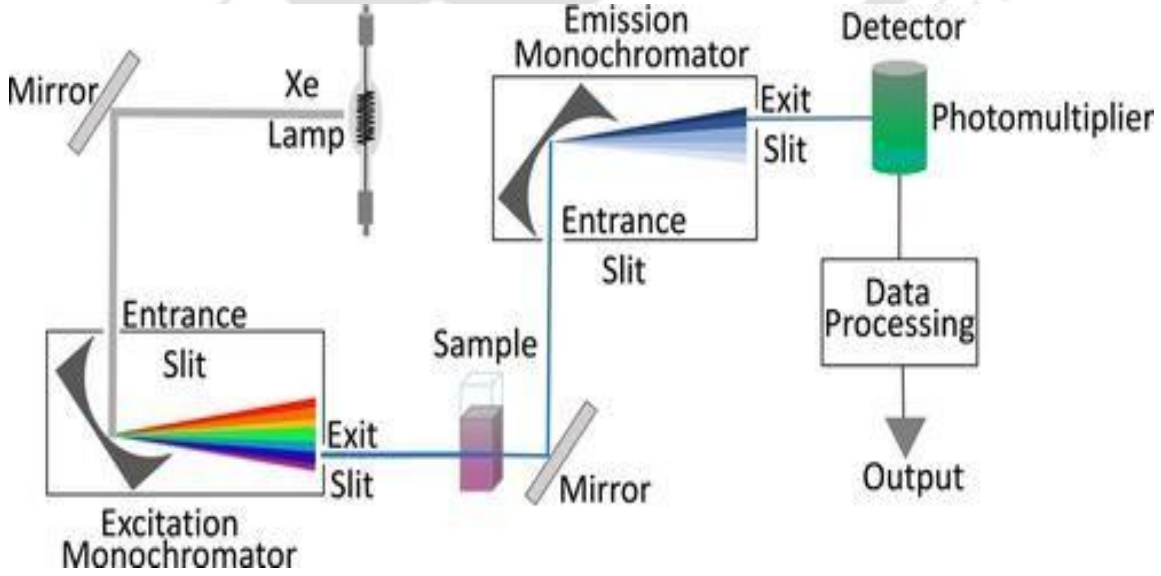

Figure 2.6: Major components of fluorescence spectrophotometer. (Gomes et al., 2019).

2.1.1.3 Circular Dichroism (CD)

Electromagnetic radiation consists of two oscillating components, electric and magnetic fields, that are mutually perpendicular and also oriented perpendicular to the direction of wave propagation. In linearly polarized light, the electric field vector oscillates within a single plane, with its direction fixed and magnitude varying. In contrast, circularly polarized light features an electric field vector that rotates continuously around the axis of propagation while maintaining a constant magnitude, as illustrated in Figure 2.7. For a chromophore to exhibit a circular dichroism (CD) signal, it must be chiral or situated in an asymmetric environment, as circularly polarized light itself is inherently chiral. When such light interacts with a chiral center, the right- and left-circularly polarized components experience differences in velocity, wavelength, and absorbance. As a result, the molar circular dichroism is influenced not only by the wavelength but also by the conformation of the absorbing molecule.

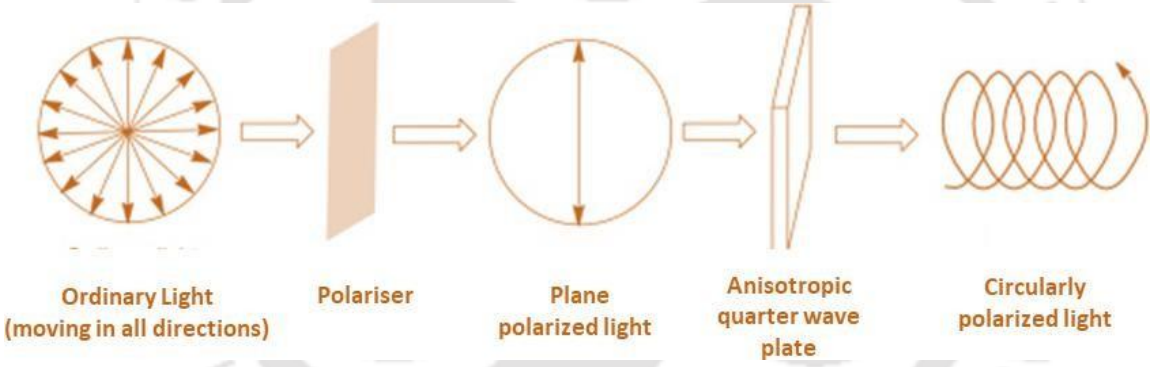

Figure 2.7: Origin of Circularly Polarized Light from ordinary light. (Adapted from Karnik & Hasan, 2021)

Furthermore, in the presence of an electric field, a linear displacement of charge occurs, while the magnetic field induces circular charge movement. This combined effect results in the excitation of an electron in a helical trajectory, characterized by both translational and rotational components. Together, these define the rotational strength (R_{0a}) associated with the transition from the ground state (0) to an excited state (a). Rotational strength is analogous to dipole strength in absorption measurements. The relationship between rotational strength and the molar ellipticity [θ], an intrinsic measure of elliptical polarization, is expressed by:

$$R_{0a} = \frac{3hc}{8\pi^3 N_0} \int \{[\theta(\lambda)]/\lambda\} d\lambda \quad (2.20)$$

A chiral molecule that is optically active interacts differently with left- and right-handed circularly polarized light: it absorbs one polarization more than the other. This unequal absorption is quantified as:

$$\Delta A = A_L - A_R \quad (2.21)$$

where A_L and A_R are the absorbance for left and right-handed circularly polarized light, respectively.

Molar absorptivity ΔA can be expressed in terms of molar circular dichroism $\Delta\varepsilon$ using Beer-Lambert Law ($A = \varepsilon\, Cl$)

$$\Delta\varepsilon = \varepsilon_L - \varepsilon_R \quad (2.22)$$

$$\Delta A = \Delta\varepsilon\, Cl \quad (2.23)$$

The circular dichroism (CD) spectrum is typically expressed in terms of ellipticity (θ), which quantifies how much the resulting light deviates from linear polarization. Mathematically, θ is defined by the electric-field components of right- and left-handed circularly polarized light as:

$$tan\,\theta = \frac{E_L - E_R}{E_L + E_R} \quad (2.24)$$

where E is the magnitude of the electric field vector of right and left circularly polarized light.

The ellipticity can be written in terms of molar absorptivity as-

$$\theta(degrees) = \Delta A \left(\frac{ln10}{4}\right)\left(\frac{180}{\pi}\right) \quad (2.25)$$

Furthermore, akin to molar circular dichroism, molar ellipticity characterizes the intrinsic optical activity of a chiral molecule by eliminating the influence of concentration and path length. It is calculated using the expression:

$$[\theta] = \frac{100\,\theta}{Cl} \tag{2.26}$$

Combining equations 2.23, 2.25 and 2.26, we get the relationship between molar ellipticity and molar dichroism,

$$[\theta] = 3300\Delta\varepsilon \tag{2.27}$$

The units of molar ellipticity are historically (deg. cm^2/dmol).

Far-UV circular dichroism (CD) spectra primarily provide insights into the secondary structure of proteins, including α-helices, β-sheets, β-turns, and random coils. In the wavelength range of 240 to 190 nm, the peptide bond is the main chromophore, showing a strong $\pi \rightarrow \pi^*$ transition around 190 nm and a weaker, broader $n \rightarrow \pi^*$ transition between 210–220 nm.

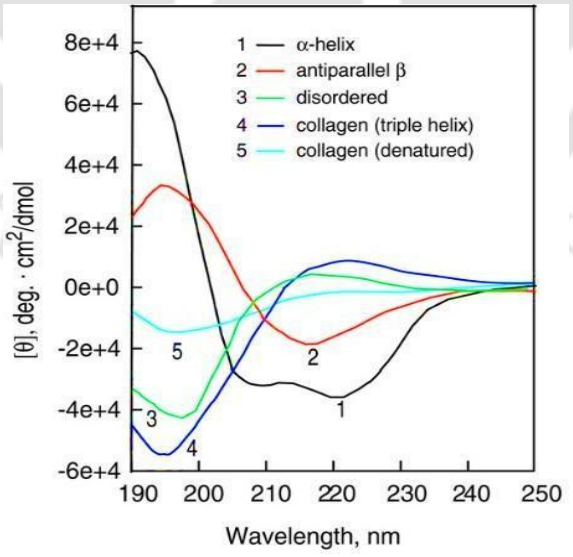

Figure 2.8: Secondary structure elements in protein and their characteristic features in the CD spectrum. (Adapted from Greenfield, 2006).

Near-UV CD spectra, on the other hand, offer information about the tertiary structure of proteins. In the 250 to 290 nm range, the signal mainly arises from the absorption of aromatic amino acid side chains such as phenylalanine (Phe), tyrosine (Tyr), and tryptophan (Trp). As the polypeptide chain folds, these aromatic residues become positioned in chiral environments, allowing the near-UV CD spectrum to serve as a distinctive fingerprint of the protein's folded state.

2.1.2 Size Exclusion Chromatography

Size Exclusion Chromatography (SEC), also known as gel filtration or gel permeation chromatography, is a technique employed to separate molecules based on their size in solution. It is particularly effective for distinguishing high molecular weight species such as polymers, large proteins, or aggregates from smaller proteins or solutes.

The fundamental principle of SEC involves the differential migration of molecules through a column packed with porous beads. As a sample traverses the column, larger molecules are unable to penetrate the pores and thus elute first, while smaller molecules enter the pores and elute later. This separation is governed by the hydrodynamic volume of the molecules, not their molecular weight per se.

Unlike other chromatographic methods that rely on interactions between the analyte and the stationary phase, SEC operates under the premise that there are minimal to no such interactions. This allows for the preservation of the native state of biomolecules during analysis. Consequently, SEC is widely utilized in the characterization of proteins, particularly for assessing aggregation states and molecular size distributions. In summary, SEC is a valuable tool for the separation and analysis of macromolecules based on size, offering insights into the structural and conformational properties of biological and synthetic polymers.

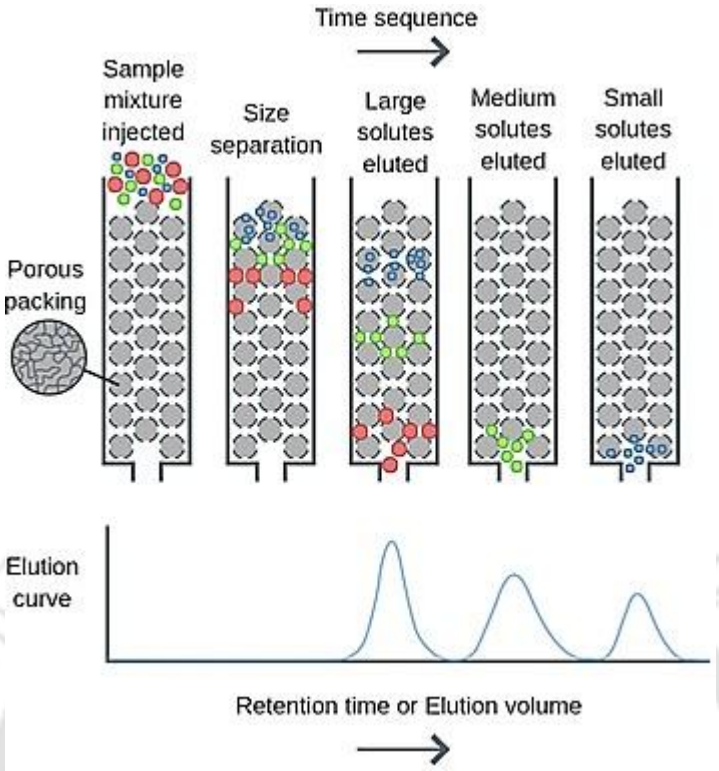

Figure 2.9: The schematic of the principle of Size Exclusion Chromatography (Adapted from Barron, 2015).

The molecular weight (M_w) of a solute is directly related to its retention time or elution volume in size exclusion chromatography (SEC). To estimate M_w, a calibration curve is constructed by plotting the partition coefficient (K_{av}) against the logarithm of the molecular weights (log M_w) of standard proteins. K_{av} is calculated using the formula:

$$K_{av} = \frac{V_e - V_o}{V_t - V_o} \qquad (2.28)$$

V_e, V_o, and V_t are the measured elution volume, void volume and the total column volume.

For polymeric biopolymers, the weight averaged molecular weight (M_w) and the number averaged molecular weight (M_n) can be described based on a distribution of individual solute molecules, where each type of molecule has a molecular weight M_i and is present in a quantity N_i. These parameters are defined as follows:

$$M_n = \frac{\sum N_i M_i}{\sum N_i} \qquad (2.29)$$

$$M_w = \frac{\sum N_i M_i^2}{\sum N_i M_i} \quad (2.30)$$

The polydispersity index (PDI) is an important metric in polymer chemistry, calculated as the ratio of weight-average molecular weight (M_w) to number-average molecular weight (M_n). It reflects how broadly the molecular masses of individual polymer chains are distributed. A higher M_w / M_n ratio indicates greater molecular weight dispersion, whereas a value close to 1 signifies a nearly monodisperse polymer sample.

2.2 Materials

2.2.1 Chemicals and Reagents

Glycine (G8898); Streptomycin Sulfate salt (S6501); Triton X-100 (T9284); β Mercaptoethanol (63689); PMSF (P7626); Sinapic acid (85429); $CaCl_2$ (C8106); Urea (U5378); 1,4-Dithiothreitol (D0632); Folin & Ciocalteu's phenol reagent (F9252); Guanidine hydrochloride (G3272); Gel loading buffer (G2526); Trifluoroacetic acid (T6508); Thioflavin T (T3516); 8-Anilinonaphthalene-1-sulfonic acid (A3125); Acrylamide (A3553); N-acetyl tryptophan amide (A6501) were purchased from Sigma Aldrich Chemicals Pvt. Limited, Bengaluru, India. The Luria Broth (M1245); Luria Agar (M557); $MgCl_2$ (TC186) and Imidazole (GRM1864); Lithium Chloride (GRM768); HEPES (MB016); Dithiothreitol (RM525); Isopropyl β-D-1- thiogalactopyranoside (MB072); Sodium chloride (GRM031); Sodium dihydrogen Phosphate monohydrate (PCT0013); Ampicillin sodium salt (TC021); EDTA(GRM3915); Sucrose (MB025) were procured from HiMedia Laboratories, India. 5-(Dimethylamino) naphthalene- 1-sulfonyl chloride (D23) was purchased from Invitrogen, Molecular Probes, USA. The PD- 10 desalting column (17-0851-01) was purchased from GE Healthcare. The Tris (Hydroxy methyl amino methane) (93315); SDS (184190); and Potassium chloride (91635); Cyclohexane (1028220500); Ammonium Sulfate (101217); Sodium hydrogen carbonate (106329); Sodium hydroxide (193102); Dimethylformamide (17754); HiTrap™ IMAC Sepharose™ FF columns (17092104) and Dialysis tubing cellulose membrane (D9277) were purchased from

Merck India Limited. Nuvia IMAC Ni-Charged Resin (780-0800) was purchased from Bio-Rad. All chemicals used were analytical grade with purity ≥98%.

2.2.1.1 Amino acid sequences of the proteins used in the thesis work

A. Alpha casein protein (214 amino acids)

```
        10         20         30         40         50
MKLLILTCLV AVALARPKHP IKHQGLPQEV LNENLLRFFV APFPEVFGKE
        60         70         80         90        100
KVNELSKDIG SESTEDQAME DIKQMEAESI SSSEEIVPNS VEQKHIQKDD
       110        120        130        140        150
VPSERYLGYL EQLLRLKKYK VPQLEIVPNS AEERLHSMKE GIHAQQKEPM
       160        170        180        190        200
IGVNQELAYF YPELFRQFYQ LDAYPSGAWY YVPLGTQYTD APSFSDIPNP
       210
IGSENSGKTT MPLW
```

B. Beta-casein protein (224 amino acids)

```
        10         20         30         40         50
MKVLILACLV ALALARELEE LNVPGEIVES LSSSEESITR INKKIEKFQS
        60         70         80         90        100
EEQQQTEDEL QDKIHPFAQT QSLVYPFPGP IHNSLPQNIP PLTQTPVVVP
       110        120        130        140        150
PFLQPEVMGV SKVKEAMAPK HKEMPFPKYP VEPFTESQSL TLTDVENLHL
       160        170        180        190        200
PLPLLQSWMH QPHQPLPPTV MFPPQSVLSL SQSKVLPVPQ KAVPYPQRDM
       210        220
PIQAFLLYQE PVLGPVRGPF PIIV
```

C. Alpha synuclein protein (140 amino acids)

```
        10         20         30         40         50
MDVFMKGLSK AKEGVVAAAE KTKQGVAEAA GKTKEGVLYV GSKTKEGVVH
        60         70         80         90        100
GVATVAEKTK EQVTNVGGAV VTGVTAVAQK TVEGAGSIAA ATGFVKKDQL
       110        120        130        140
GKNEEGAPQE GILEDMPVDP DNEAYEMPSE EGYQDYEPEA
```

D. Human Lysozyme protein (148 amino acids)

```
          10          20          30          40          50
MKALIVLGLV LLSVTVQGKV FERCELARTL KRLGMDGYRG ISLANWMCLA

          60          70          80          90         100
KWESGYNTRA TNYNAGDRST DYGIFQINSR YWCNDGKTPG AVNACHLSCS

         110         120         130         140
ALLQDNIADA VACAKRVVRD PQGIRAWVAW RNRCQNRDVR QYVQGCGV
```

E. ERK2 protein (360 amino acids)

```
        10          20          30          40          50          60
MAHHHHHHAG PEMVRGQVFD VGPRYTNLSY IGEGAYGMVC SAYDNVNKVR VAIKKISPFE

        70          80          90         100         110         120
HQTYCQRTLR EIKILLRFRH ENIIGINDII RAPTIEQMKD VYIVQDLMET DLYKLLKTQH

       130         140         150         160         170         180
LSNDHICYFL YQILRGLKYI HSANVLHRDL KPSNLLLNTT CDLKICDFGL ARVADPDHDH

       190         200         210         220         230         240
TGFLTEYVAT RWYRAPEIML NSKGYTKSID IWSVGCILAE MLSNRPIFPG KHYLDQLNHI

       250         260         270         280         290         300
LGILGSPSQE DLNCIINLKA RNYLLSLPHK NKVPWNRLFP NADSKALDLL DKMLTFNPHK

       310         320         330         340         350         360
RIEVEQALAH PYLEQYYDPS DEPIAEAPFK FDMELDDLPK EKLKELIFEE TARFQPGYRS
```

Charged amino acids: Arginine(blue); Aspartate(red); Lysine(blue); Glutamate(red); Histidine(blue) are highlighted in bold fonts.

Aromatic amino acids: All are green in colour.

2.2.1.2 Amino acid sequences of the phosphorylated and unphosphorylated peptides

Two pairs of peptides were commercially synthesized. Their sequences are as follows:

LG 7:- LRRASLG

LG 7(P):- LRRAS (P) LG

KK9:- KSPAKTPVK

KK9 (P):- KS (P) PAKT (P) PVK

Charged amino acids: Lysine (blue); Arginine (blue) are highlighted
Phosphorylated serine is highlighted in red, with added P in parenthesis.

Alpha-casein, beta-casein and Human Lysozyme proteins were procured from Sigma Aldrich, Bangalore, India, in lyophilized form. These proteins were directly used without any further processing or purification. Purity check for alpha casein and beta casein protein was checked using SDS PAGE.

2.3 Methods

2.3.1 Protein(s) purification

2.3.1.1 Cloning

A) Alpha Synuclein protein

Alpha synuclein containing 214 amino acids were cloned in a pET21a expression vector with no additional tag attached to it. The construct was provided by Prof. Mireille M. A. E. Claessens, University of Twente, Netherlands.

B). ERK2 protein

ERK2 protein were cloned in pETHis6 plasmid vector with a T7 promoter. The construct was provided by Prof. Vinay Kumar Nandicoorie from National Institute of Immunology, New Delhi, India.

2.3.1.2 Preparation of competent cells

E. coli BL-21 (DE3) strain was used for both alpha synucein and ERK2 proteins. DH5α strain was used for plasmid multiplication. E. coli DH5α and BL21 competent cells were transformed with plasmid DNA for the purposes of DNA isolation and protein expression/purification, respectively. Competent cells were prepared using a chemical method involving $CaCl_2$ treatment. A starter culture was initiated in 5 mL of Luria Broth (LB) with a 1% inoculum and incubated overnight at 37 °C and 180 rpm in a shaker incubator. Following overnight growth, 500 µL of the starter culture was inoculated into 50 mL of LB and further incubated at 37 °C, 180 rpm until the absorbance at 600 nm reached 0.4. The culture was then chilled on ice for 10 minutes and centrifuged at 3000 rpm for 10 minutes at 4 °C. After discarding the supernatant, the cell pellet was gently resuspended in 15 mL of ice-cold solution containing 80 mM $MgCl_2$ and 20 mM $CaCl_2$. A second centrifugation was performed under the same conditions, and the resulting pellet was resuspended in a final volume of 1 mL composed of 900 µL CaCl2 and 100 µL autoclaved glycerol. The prepared competent cells were aliquoted in 100 µL volumes and stored at -80 °C for later transformation use. All procedures were carried out under sterile conditions. Solutions were autoclaved prior to use, and the entire preparation process was conducted within a laminar airflow (LAF) cabinet to maintain sterility.

.

2.3.1.3 Transformation

DH5α competent cells were transformed with plasmid DNA using the heat shock method. A total of 25 ng of plasmid DNA was mixed with the competent cells, followed by a heat shock at 42°C for 60 seconds. The cells were then placed on ice for 2 minutes to stabilize. Subsequently, 800 µL of autoclaved LB was added to the mixture, and the cells were incubated at 37 °C with shaking at 180 rpm for 1 hour to allow recovery and expression of the antibiotic resistance gene. Following incubation, the cells were plated on Luria agar plates supplemented with 100 µg/mL ampicillin and incubated at 37°C for 12 hours. After incubation, single colonies were selected and used to inoculate 5 mL LB medium containing ampicillin. These overnight cultures were then used for plasmid extraction using the QIAprep Spin Miniprep Kit. The purified plasmid DNA was stored at -20°C for further use.

E. coli BL21 (DE3) competent cells stored at -80 °C were thawed on ice. Approximately 0.2–0.6 µL of plasmid DNA encoding alpha-synuclein or ERK2 was added to separate aliquots of competent cells, followed by incubation at 4 °C for 15 minutes. Negative control samples

containing competent cells without plasmid DNA were also prepared in parallel. After incubation, the tubes were subjected to a heat shock at 42 °C for 90 seconds and then immediately returned to ice for a brief incubation. The cells were then mixed with 800–900 µL of LB medium without antibiotics and incubated at 37 °C with shaking at 180 rpm for 1 hour to allow expression of the antibiotic resistance gene. Once the culture showed slight turbidity, indicating bacterial growth, the cells were centrifuged at 6,000 rpm for 10 minutes. The resulting pellet was resuspended in 100 µL of fresh LB medium and plated on LB agar plates containing 100 µg/mL ampicillin, specific for either alpha-synuclein or ERK2 transformation. The plates were incubated in an inverted position at 37 °C for 10–12 hours until colonies of transformed cells became visible.

2.3.1.4 Expression

E. coli BL21 cells transformed with individual recombinant plasmids were grown in LB broth containing 100 µg/mL ampicillin at 37°C. When the culture achieved an optical density of 0.6–0.7 at 600 nm, Isopropylthio-β-d-galactoside (IPTG) was added to a final concentration of 1.0 mM for alphasynuclein proteinexpressionand 0.25 mMfor ERK2 expression. After an additional 3-4 hours of incubation (alpha synuclein protein) and 12 hours of incubation (ERK2 protein), the cells were harvested by centrifugation at 6000 rpm for 15 min, and the pelleted cells were kept at -20°C.

2.3.1.5 Purification

Purification of ERK2 was carried out similar to that of previously reported protocol (Khokhlatchev et al., 1997) with some modifications. From a 1litre culture, the pelleted cells were mixed in ice- cold lysis buffer (50 mM phosphate buffer (pH 7.4); 500 mM NaCl; 5 mM Imidazole). Subsequently, 1mM phenyl-methyl-sulfonyl-fluoride (PMSF) was added, and the cells were lysed by sonication. The cell lysate was then centrifuged for 30 mins at 13000g, at 4°C. Supernatants were filtered with a 0.45 µm filter and were loaded on the affinity column of nickel–NTA agarose resin (Qiagen) with 2 mL Ni-NTA agarose beads. Before supernatants were loaded, the column was pre-equilibrated with binding buffer (50 mM phosphate buffer (pH 7.4); 500 mM NaCl; 5 mM Imidazole). The resin containing the protein was kept for 4-5 hours in a rocker at 4 °C allowing the Ni-NTA beads to bind to His tag of protein. 2-3 column volumes (CVs) of the same binding buffer were used to wash the protein-

bound-Ni-NTA beads. The proteins were then eluted with elution buffer I (50 mM phosphate buffer (pH 7.4); 500 mM NaCl; 50 mM Imidazole) and with elution buffer II (50 mM Phosphate buffer (pH 7.4); 500 mM NaCl; 250 mM Imidazole). The samples were collected in multiple fractions. Quantifying proteins in these fractions was done using UV-Visible spectroscopy, and fractions with relatively higher protein concentrations were pooled together. The protein was dialyzed against enough water to remove the imidazole from the elution buffer. Subsequently, the proteins were further characterized by SDS-PAGE and MALDI -TOF to check the purity of the purified proteins.

Alpha Synuclein purification was carried out similar to that reported previously [Hoyer et al., 2002] with minor modifications. Cells harvested from 1-litre culture were lysed and sonicated in 50 mM Tris- HCl buffer. 1 mM EDTA, 1 mM PMSF, (pH 7.4) and centrifuged for 1 hour at 13000 g, 4°C. Solid streptomycin sulphate was added to 1% w/v of supernatant and centrifuged for 30 min, 4°C. Subsequently, solid ammonium sulphate was added to 47% w/v of the supernatant and centrifuge for 1 hour, 4°C. The pellet is collected and stored at 4°C. The pellet was then dissolved in 100 mM Tris-HCl, pH 7.5,100 mM NaCl and 2 mM DTT (purification buffer), filtered and passed through Hi-load Q Sepharose column (5 ml for one CV) at 1 mL/min for Anion Exchange Chromatography. The elution was collected with the gradient of 0 mM to 500 mM NaCl in purification buffer. The elute was collected around 350 mM NaCl concentration. This was then passed through Hi-load Sephadex column during Size Exclusion Chromatography (SEC). The elute was collected as purified monomeric alpha synuclein protein. Anion Exchange Chromatography and SEC was carried out using ÄKTApurifier TM FPLC (GE Healthcare) chromatography system. Protein was dialyzed in 25 mM phosphate buffer, pH 7.5, for 5-6 hours. The protein was stored at -80°C. All the AEC and SEC analyses were done after pre-equilibrating the column with 2 CVs, the same degassed buffer used for proteins.

2.3.2 Sodium dodecyl sulfate-polyacrylamide gel electrophoresis (SDS-PAGE)

To assess protein expression and purification, reducing SDS-PAGE was carried out following a standard protocol. A resolving gel (15% acrylamide) and a stacking gel were prepared using deionized water, acrylamide, Tris(hydroxymethyl)aminomethane, SDS, ammonium persulfate, and N,N,N',N'-tetramethylethylenediamine (TEMED).

Protein samples were mixed with gel loading buffer in a 3:1 ratio and denatured by heating at 95 °C for 3–5 minutes. The prepared samples were loaded into separate wells of the casted gel, along with a standard molecular weight marker for reference. The gels were run in a vertical Mini-PROTEAN Tetra Electrophoresis System (Bio-Rad) at a constant voltage of 80–100 V for approximately 1.5–2 hours, until the tracking dye reached the bottom of the gel.

Post-electrophoresis, the gels were stained using Coomassie Brilliant Blue R-250 solution, composed of 0.025% (w/v) dye in 45% methanol, 45% deionized water, and 10% glacial acetic acid, for 4 hours. Gels were then de-stained in a solution containing 30% methanol, 10% glacial acetic acid, and 60% deionized water until distinct protein bands and molecular markers became clearly visible.

2.3.3 Protein estimation

The concentrations of both alpha-synuclein and ERK2 proteins were determined using the Lowry method [Lowry et al., 1951]. For preparing the standard curve, a series of BSA (Bovine Serum Albumin) dilutions ranging from 0.05 to 1.00 mg/mL were made from a 1.00 mg/mL stock solution in water. Each dilution, along with 200 µL of both the proteins individually and a blank sample (deionized water), was added to test tubes wrapped in aluminum foil to prevent light exposure. To each tube, 2 mL of Reagent I was added. Reagent I was prepared by mixing 48 mL of Solution A (2% sodium carbonate in 0.1% NaOH), 1 mL of Solution B (2.37% potassium sodium tartrate in water), and 1 mL of Solution C (1.56% copper sulfate in water). The mixtures were vortexed thoroughly and incubated at room temperature for 10–15 minutes. Following incubation, 200 µL of Reagent II, prepared by combining equal parts of Folin's reagent and water, was added to each sample. The mixtures were gently mixed and incubated in the dark for 30 minutes. Absorbance readings for each sample were taken in duplicates at 650 nm. The protein concentrations were then accurately calculated using the standard BSA curve plotted as absorbance versus concentration.

However, for experiments involving Phosphorylated and unphosphorylated peptides, the concentrations of lyophilized peptides were calculated based on their weighed mass rather

than using the Lowry method.

Furthermore, the concentrations of peptides were validated by recording absorbance at 215 nm and 225 nm (A_{215} and A_{225}) in the far-UV range, and applying the following equation:

$$\text{Protein/peptide concentration } (\mu g/ml) = 144*(A_{215}-A_{225}) \quad (2.31)$$

Concentration of alpha synuclein protein and ERK2 protein was calculated by taking the absorbance in UV region and using extinction coefficient ε_{280} of 5600 $M^{-1}cm^{-1}$ and 37800 $M^{-1}cm^{-1}$ for alpha synuclein and ERK2 protein respectively.

2.3.4 Mass Spectrometry

MALDI-TOF mass spectrometer (Daltonics Bruker, Germany) was used to determine the mass of alpha synuclein and ERK2 protein. A solution of Sinapic acid was dissolved in TA-30 solvent [0.1% Trifluoroacetic acid and acetonitrile mixed in 7:3 ratios] to prepare the MALDI matrix. It was then sonicated for 30 minutes, centrifuged at 12000 rpm at 25 °C for 15 minutes, and the supernatant collected carefully was mixed with protein in a 2:1 ratio in PCR tubes. The mixture was then spotted on the target plate and was allowed to dry for 3 hours. Data acquisition was made with flex control in Linear Mode, and analysis was carried out by flex Analysis software (make: Bruker Daltonics).

2.3.5 Dephosphorylation of alpha casein and beta casein

The commercially purchased casein proteins were in phosphorylated forms. Dephosphorylation of Alpha casein was carried out using alkaline phosphatase according to the method of Lorient and Linden (1976) with slight modifications. 25 µM Alpha casein was dissolved in 20 mM Tris-HCl (pH 9.5) with 10 mM $MgCl_2$. A 0.5 mL of alkaline phosphatase (5 units/mL) solution was added to a 2 mL Alpha casein solution and placed in a narrow dialysis bag. The reaction mixture was dialysed against 500 mL external buffer (20 mM tris-HCl at pH 9.5, 10 mM $MgCl_2$ and 1 mM PMSF) at 37°C with continuous stirring for 12 hours. The same protein was dialysed under similar conditions without alkaline phosphatase for comparison. The dephosphorylation reaction was dialysed against the same buffer in a

dialysis bag to allow for inorganic phosphate to travel across dialysis membrane and the external buffer and establish equilibrium. Dephosphorylation of Beta casein (25 μM) was carried out under the same conditions as Alpha casein.

2.3.6 Alpha synuclein aggregation

Alpha synuclein aggregation was performed as mentioned [Iyer et al., 2014]. For aggregation studies the protein was dialysed against PBS buffer (pH 7.4) and concentrated using Vivaspin 6 centricon. The protein concentration taken was 100 μM. The aggregation was set with monomeric alpha synuclein (100 μM) in 25 mM PBS buffer (pH 7.4) and 150 mM NaCl at 300 rpm at 37°C for 10 hours. Different time scales were observed for the protein aggregation, and their characterization was done using various techniques at multiple time points.

2.3.7 Human Lysozyme Aggregation

A stock solution of Human Lysozyme (HuL) monomer (0.5 mM) was prepared in deionized water. Desired concentrations for experiments were obtained by diluting this stock in the respective buffers. All concentrations stated refer to the monomeric form of HuL.

A.) Aggregation at Alkaline pH 12.2

HuL (120 μM; 1 mL) was diluted in 50 mM sodium phosphate buffer at pH 12.2 and incubated at 23–25 °C without agitation for 10 days [Ravi et al., 2014b]. At the end of each day, aliquots were either stored at 4 °C for further analysis or immediately diluted in 0.1 M bicarbonate buffer (pH 9.3) to a final concentration of 20 μM for absorbance measurements.

B.) Aggregation at Acidic pH 2.0

HuL (1.36 mM; 1 mL) was incubated in 10 mM glycine buffer (pH 2.0) at 65 °C with intermittent stirring for 5 days [Chaari et al., 2015; Krebs et al., 2000]. Each day, 100 μL aliquots were collected and stored at 4 °C for further testing. For absorbance and luminescence measurements, the incubated samples were diluted to 100 μM using the same buffer.

2.3.8 Unfolding of proteins: HuL and ERK2

Protein unfolding was monitored using both conventional techniques and the ProCharTS method.

A.) Human Lysozyme unfolding

Human Lysozyme was incubated with varying concentrations of guanidinium hydrochloride (GdnHCl) ranging from 0 to 6 M in 20 mM sodium phosphate buffer containing 0.5 mM TCEP at pH 7.2 for 4 hours at room temperature (~25 °C). The unfolding process was characterized using multiple parameters: ProCharTS absorbance, MRE_{222}, ProCharTS luminescence, tryptophan (Trp) fluorescence and ANS fluorescence. The concentration of GdnHCl stock solutions was determined using refractive index measurements on an Abbe's refractometer.

B.) ERK2 unfolding

Similarly, ERK2 was treated with 0 to 6 M GdnHCl in 20 mM sodium phosphate buffer (pH 7.2) and incubated for 6 hours at room temperature. Unfolding was monitored using ProCharTS absorbance, ProCharTS luminescence, MRE_{222}, and Trp fluorescence and ANS fluorescence at various stages along the unfolding pathway.

2.3.9 UV-Visible and ProCharTS absorbance

Double beam Lambda-25 UV-Visible Spectrophotometer (Perkin Elmer, USA) was used to record absorbance. A quartz cuvette with a path length of 10 mm (Hellma; Z600210) was used for all measurements. Absorption spectra were acquired in duplicates between 250 nm and 800 nm with a scan speed of 480 nm/minute and are averaged. The spectra obtained from each concentration were normalized with individual concentration to calculate the extinction coefficient for all the samples.

For the Phosphorylated and unphosphorylated peptides, 2 mM concentration was used

and their absorbance was recorded. The experiments were carried out in deionized water and at room temperature.

For alpha casein and beta casein proteins, absorbance measurements were performed with 25 μM and 45 μM concentrations respectively and their absorbance at 6 different wavelengths was plotted versus concentration. The experiments were carried out in deionized water and at room temperature

For alpha synuclein aggregation and Human Lysozyme aggregation (pH 2), ProCharTS spectra (250-800 nm) at different times were carried out in their respective aggregation buffers. The change in ProCharTS absorbance at various wavelengths versus aggregation time was calculated from each spectrum and plotted versus time. The protein concentration was kept at 50 μM and 25 μM of alpha synuclein and human lysozyme respectively. All the aggregated samples were centrifuged at 12,000 g for 10 minutes prior to absorbance measurements to remove insoluble aggregates that can cause light scattering. All the readings were done in duplicates and at room temperature.

For HuL aggregation pH 12.2, ProCharTS absorbance spectra were recorded after dilution in 0.1 M sodium bicarbonate buffer (pH 9.3) to keep the lysine side chain charged and protonated for ProCharTS. All the aggregated samples were centrifuged at 12,000 g for 10 minutes prior to absorbance measurements to remove insoluble aggregates. All the readings were done in duplicates and at room temperature.

For measurement of linearity in absorbance with increasing concentration, among different amino acids, stock of 20 μM of Human Lysozyme and 15 μM of ERK2 was used in their respective buffers.

For absorbance measurements done to study the effect of unfolding on the ProCharTS, the incubated HuL and ERK2 samples were measured against the respective buffer blanks containing either 0 - 6 M Gdn·HCl. All the solutions were buffered at pH 7.5 (20 mM Phosphate buffer, 0.5mM TCEP)

2.3.10 Steady-state luminescence

Luminescence Emission Spectra: Luminescence emission spectra for LG7 peptides and KK9 peptides were measured in the range 300-500 (λ_{ex} 280 nm); 330-600 (λ_{ex} 310 nm); 360-660 (λ_{ex} 340 nm); 375-720 (λ_{ex} 355 nm); 390-720 (λ_{ex} 370 nm) and 430-800 nm (λ_{ex} 410 nm). The slit width for excitation was 2 nm, and it was kept at 15 nm for emission. Concentrations for all peptides were 2 mM.

Luminescence Emission of alpha casein and beta casein dephosphorylation was carried out with 25 μM and 45 μM of alpha casein and beta casein respectively at 4 different excitation wavelengths: 310 nm, 340 nm, 355 nm and 370 nm were used, and emission spectra were collected between 330-550; 360-600; 375-600 and 390-600 nm respectively. Slit width: excitation = 2 nm, emission = 15 nm. All readings were taken in duplicates, and 10 scans were recorded for each and averaged later. Moreover, the area under the emission curve for all the sample was integrated for each spectrum and was plotted versus the corresponding exciting wavelength.

The intrinsic luminescence from alpha synuclein and HuL aggregates (formed at pH 2 and pH 12.2) were observed by exciting the samples collected at different time points at λex 280 nm (only for alpha synuclein aggregates), 295 nm, 340 nm and 355 nm with excitation slit width of 2 nm and emission was collected with a slit width of 5 nm. Before the fluorescence measurements, all the samples were centrifuged at 10,000g for 10 minutes to remove any insoluble aggregates.

Effect of unfolding of HuL and ERK2 proteins on the luminescence from charge transfer states was observed by exciting the natively folded and unfolded proteins (in presence of 0-6 M Gdn-HCl) at λex 340 nm and 355 nm with slit width of 2 nm and emission was collected between 360-600 nm and 375-600 nm respectively with a slit width of 15 nm. Similarly, all the samples were also observed for the Trp fluorescence to affirm the event of unfolding. For this, samples were excited at λex 295 nm with a slit width of 2 nm and emission was collected between 315 nm to 550 nm with a slit width of 5 nm. All the samples were buffered

at pH 7.5 (20 mM phosphate buffer) to avoid any effect from mere change in pH.

Luminescence Linearity*:* Linearity in luminescence was carried out at λ_{ex} 355 nm with similar concentrations of all samples as used for acquiring emission spectra. The luminescence spectra thus collected were integrated and linearly fitted with varied concentrations using OriginPro 8.5 software.

2.3.11 Stokes shift

Excitation wavelength dependent changes in Stokes shift (in wavenumber units) was calculated from the emission spectra of all the samples when excited at 280, 310, 340, 355, 370 and 410 nm using the equation below

$$Stokes\ Shift\ \ \Delta(\bar{\nu}) = \ \bar{\nu}_{ex}\ - \bar{\nu}_{emm} \qquad (2.32)$$

Here, $\bar{\nu}_{ex}$ and $\bar{\nu}_{emm}$ stands for the excitation wavelength and corresponding emission maximum, respectively (in cm-1).

2.3.12 ANS binding assay

8-Anilinonaphthalene-1-sulfonic acid (ANS) binding assays were performed by measuring steady-state fluorescence intensity of ANS. Aliquots of HuL and ERK2 protein unfolding reaction (10 μM each) were collected at different time points and mixed with 10 μM ANS (from stock solution) in a 1:1 ratio. Fluorescence spectra were then recorded for each aliquot. A control spectrum was also obtained using 10 μM ANS alone in the same phosphate buffer (pH 7.2) used for protein unfolding.

The ANS concentration was determined using its molar extinction coefficient of 4,900 $M^{-1}cm^{-1}$ at 350 nm [Hawe et al., 2010]. Excitation was carried out at 380 nm, and emission spectra were recorded from 400 nm to 700 nm. The slit widths were set at 2 nm for excitation and 5 nm for emission. Background fluorescence from the buffer was subtracted from all sample spectra. Each measurement was performed in duplicate, with two spectral

scans recorded per reading.

2.3.13 Thioflavin T (ThT) assay

To assess fibril formation under acidic conditions, a Thioflavin T (ThT) fluorescence assay was performed following a previously established protocol with slight modifications [Ravi et al., 2014a]. A stock solution of ThT was prepared in deionized water and filtered through a 0.45 µm membrane filter. The concentration of ThT was determined spectrophotometrically at 416 nm using an extinction coefficient of 26,620 $M^{-1}cm^{-1}$ in ethanol [Gade Malmos et al., 2017; Ravi et al., 2014a].

For optimal ThT binding to amyloid fibrils, a dye-to-monomer molar ratio of 2:1 was maintained [Wall et al., 1999]. Accordingly, fluorescence measurements were performed by mixing 10 µM of aggregated protein with 20 µM ThT in an aqueous buffer at pH 8.5. The sample was excited at 450 nm (excitation slit width: 1 nm), and emission spectra were recorded between 470 nm and 550 nm (emission slit width: 5 nm). The fluorescence intensity was quantified by calculating the area under the emission curve after subtracting the background spectrum obtained without ThT.All measurements were conducted in triplicate using a 1 mL quartz cuvette with a 10 mm path length [Hellma (Z600253)] and a Fluoromax-3 spectrofluorometer (Jobin-Yvon Horiba Inc., USA).

2.3.14 Circular Dichroism

A CD spectrometer (Make: Jasco, Model J-1500, Jasco Inc., Maryland, USA), was used to obtain CD spectra. Spectra were collected starting from 190 to 260 nm, keeping scan speed at 100 nm/minute; data pitch at 0.1 nm and bandwidth at 2 nm. 2 mm quartz cuvette (Starna Scientific Ltd) was used for measurements. Blank subtraction for deionized water or buffers was corrected before data acquisition. A thermoregulator is equipped with the CD spectrometer for stabilizing temperature at any defined temperature. For each sample, two independent scans were carried out at 25°C.

For dephosphorylation study,2 µM of protein concentrations were used in their respective

buffers. All the readings were done in duplicate scans and at room temperature.

For aggregation study, 2 μM of protein concentrations in their respective aggregation buffer in various time intervals were used for the CD study. All the readings were done in duplicate scans and at room temperature.

For unfolding study, 1.25 μM of concentrations of proteins were used in their respective unfolding buffer. For each sample, two independent scans were carried out at room temperature.

CHAPTER 3

INVESTIGATING EFFECT OF PHOSPHORYLATION ON SYNTHETIC PEPTIDES AND CASEIN PROTEINS USING PROCHARTS.

3.1 Introduction

Protein phosphorylation stands as the most prevalent and extensively researched post-translational modification (PTM) within eukaryotic organisms. This reaction plays a pivotal role in a multitude of signal transduction pathways, encompassing functions like proliferation, differentiation, apoptosis, and metabolic processes that uphold cellular equilibrium and orchestrate physiological responses to external cues [Hunter, 2000]. Phosphorylation exerts its regulatory influence through diverse mechanisms, encompassing conformational adjustments that reshape protein structures and the establishment of binding sites for the assembly of multiprotein complexes [Pawson et al., 2001].

Phosphorylation is modulated by kinases, which covalently attach negatively charged phosphate groups to the neutral hydroxyl groups present on Serine (Ser), Threonine (Thr), and Tyrosine (Tyr) residues, resulting in the formation of polar anionic entities. Conversely, phosphatases execute the opposite of this biochemical process by removing phosphate groups. The interplay between these two opposing enzymes tightly governs the dynamics of phosphorylation, ensuring the precise propagation of signal transduction events and the modulation of protein activities across various biochemical cascades [Pawson et al., 2005; Tarrant et al., 2009; Cohen, 1992].

Present day investigations into protein phosphorylation primarily revolve around the identification of phosphorylation sites, the quantification of their abundance, and the comprehensive understanding of their functional implications. Analytically, the study of phosphorylation poses inherent challenges due to the labile nature of this modification and its presence in sub-stoichiometric concentrations [Tsai et al., 2011].

Various biochemical approaches have been developed and employed to scrutinize protein phosphorylation; however, each approach carries intrinsic limitations. For instance, phosphoimaging, a historical method, initially relied on the use of radioisotopes, such as the incorporation of P^{32} -labeled ATP to track kinase activity directed towards specific substrates [Karra et al., 2017]. In more recent times, fluorescence-based dyes have emerged as an alternative, permitting the selective or universal staining of phospho-residues and direct

imaging on blotting membranes [Akita et al., 2008; Martin et al., 2003]. Nevertheless, it is worth noting that these techniques involve synthesis and use of dyes, toxic chemicals and generation of radioactive waste.

Alternatively, antibody-based immunoassays, including immunoblotting and enzyme-linked immunosorbent assay (ELISA), have been adopted as alternatives to radiolabelling techniques. [Blackburn et al., 2009]. However, the adoption of these methods has been hindered by the exorbitant costs associated with utilizing specialized antibodies and the necessity for time-consuming washing steps.

During the past decade and beyond, there has been a growing trend towards employing synthetic chemical sensors that utilize fluorescent or luminescent reporters for detecting phosphorylation at the peptide or protein level [Rothman et al., 2009; Tremblay et al., 2008; Sakamoto et al., 2009; Kraskouskaya et al., 2014; Liu et al., 2018]. However, this approach had limitations, including the requirement for a chromophore to attach to the peptide substrate and the need for the attachment site to be at an optimal distance from the phosphorylation site. These limitations restricted the broader application of this method. Consequently, there remains a strong desire for the development of a novel, nonradioactive, cost-effective, and label-free sensing technique for phosphorylation. Phosphorylation at uncharged -OH sidechains of Ser/Thr/Tyr involves incorporation of phosphate group (PO_4^{2-}) with 2 negative charges. A technique that exploits this change at the phosphorylated site is desirable.

Recently, charged and non-aromatic amino acids like lysine were initially observed to possess electronic absorption in the near UV- Vis region [Homchaudhuri et al., 2001; Homchaudhari et al., 2004]. Later, researchers have discovered Protein Charge Transfer Spectra (ProCharTS) arising from charge clusters among charged amino acids and charge rich monomeric proteins, which exhibit distinctive UV/Visible absorbance characteristics [Prasad et al., 2017; Ansari et al., 2018]. Subsequent investigations employing time-dependent density functional theory (TDDFT) calculations and computational studies focusing on Lysine-Glutamate contacts have suggested that this intrinsic absorption arises from charge transfer transitions occurring among charged residues located in close proximity [Ansari et al., 2018]. Furthermore, the detection of intrinsic fluorescence or deep-blue/blue

luminescence has proven to be promising in monomeric proteins [Guptasarma et al., 2008]. Recently, the concept of intrinsic luminescence in monomeric proteins, stemming from charge recombination following excitation at ProCharTS absorption wavelength, has been put forward as the source of this blue luminescence and has been termed "ProCharTS luminescence [Kumar et al., 2020; Kumar et al., 2022].

Following phosphorylation, amino acids like Ser, Thr and Tyr undergo a chemical transformation, becoming negatively charged as they are covalently bonded to phosphate groups. Recent research has involved computational studies and a comparison of the absorption spectra of these phosphorylated amino acid residues. Through TDDFT calculations, it has been established that charge transfer (CT) transitions dominate the UV-Vis spectra in all phosphorylated amino acid chromophores, with the lowest energy transitions identified as Peptide backbone to side chain charge transfer transitions (PBS-CT) [Mandal et al., 2018]. In this experimental study, we employ ProCharTS absorbance and luminescence as a cost-effective, non-invasive, and label-free technique to detect protein phosphorylation, accounting for the contributions from charged residues and phosphorylated groups coupled with structural changes accompanying post-translational modifications.

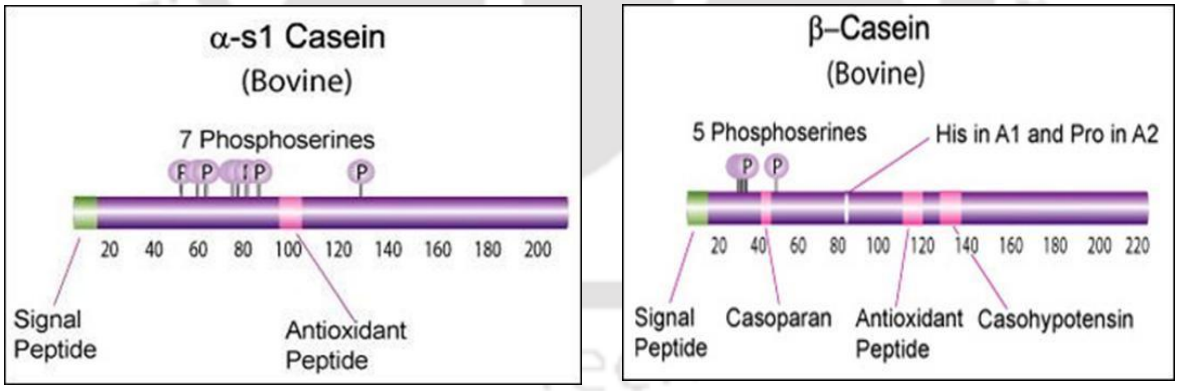

Figure 3.1: Phosphorylation sites of alpha casein and beta casein protein (phophSite calculator)

Our work entails a comparative analysis of phosphorylated and unphosphorylated peptides and dephosphorylated forms of Casein proteins, specifically alpha-casein and beta-casein, using ProCharTS absorption and luminescence, in conjunction with traditional methods like MALDI, SDS PAGE, CD and ANS. The findings underscore the potential of ProCharTS as a valuable tool to monitor phosphorylation in a label-free approach.

Both phosphorylated and unphosphorylated peptides were commercially synthesized to serve as model systems, incorporating positively charged residues (cations) that could facilitate charge transfer upon interacting with negatively charged phosphate ions (anions).

3.2 Results and Discussions

3.2.1 ProCharTS absorbance of phosphorylated and unphosphorylated peptides

In Figure 3.2, the impact of phosphorylation on Protein Charge Transfer Spectra (ProCharTS) using synthetic peptides LG7 and KK9, along with their phosphorylated counterparts, LG7P and KK9$(P)_2$ was analyzed. Notably, LG7P, which is singly phosphorylated, exhibited a higher absorbance profile compared to its unphosphorylated form, LG7. Conversely, KK9$(P)_2$, bearing two phosphate groups, showed a reduced absorbance profile relative to KK9. This suggests that while single phosphorylation may enhance ProCharTS due to increased charge content, multiple phosphorylations could lead to charge repulsion, diminishing the spectral intensity.

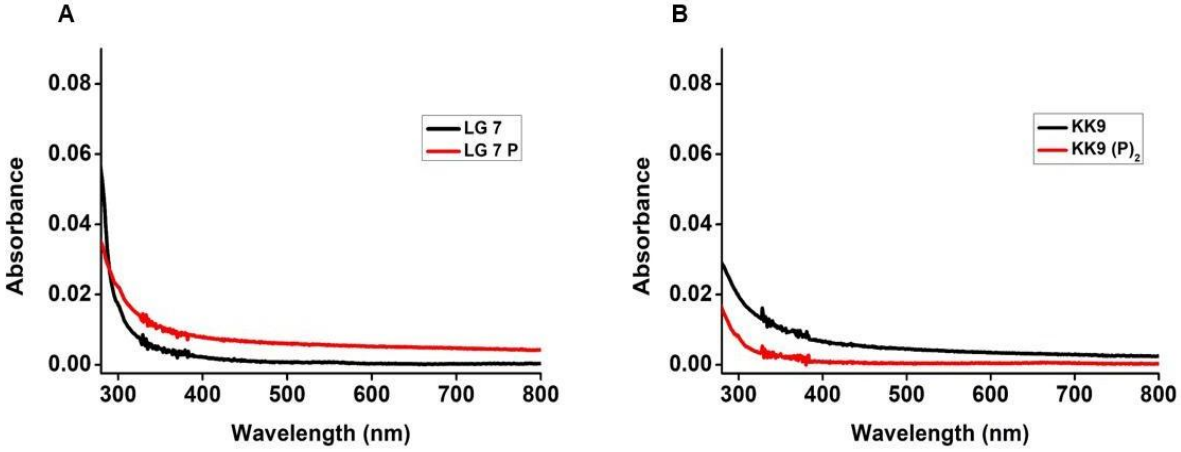

Figure 3.2. Absorption spectra of phosphorylated and unphosphorylated 2 mM (Panel A) LG 7 and (Panel B) KK9 in water from 250 nm to 800 nm averaged over 5 scans. The samples were freshly prepared in water and readings were taken at 25°C.

The molar extinction coefficients were calculated with the help of the concentration determined. The molar extinction coefficients for phosphorylated and unphosphorylated

LG7 and KK9 peptides were calculated as shown in **Figure 3.3**. As can be seen, the extinction coefficient of LG7 phosphorylated peptide is higher than the unphosphorylated LG7 peptide. On the contrary, the extinction coefficient of KK9 phosphorylated peptide is lower than the unphosphorylated KK9 peptide.

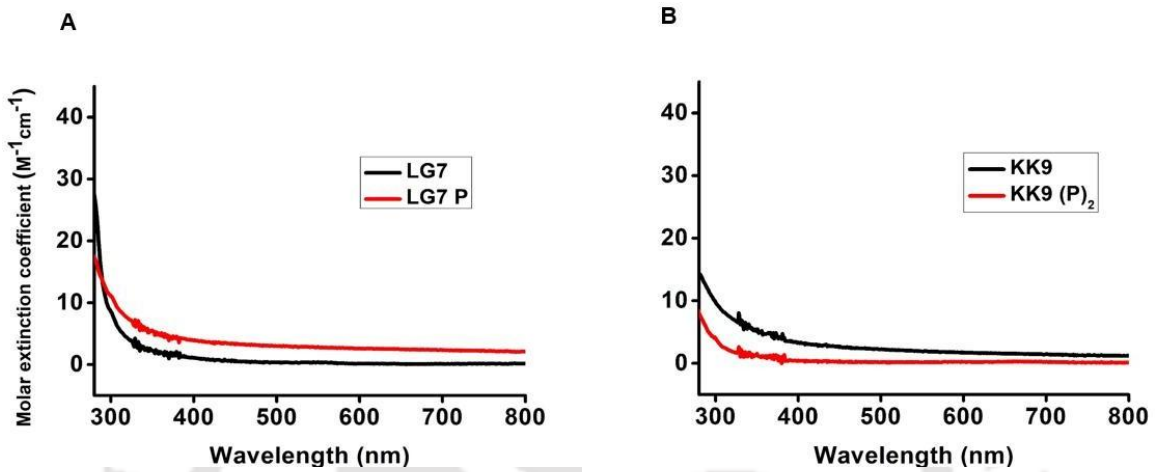

Figure 3.3. Molar extinction coefficient of phosphorylated and unphosphorylated 2 mM (Panel A) LG 7 and (Panel B) KK9 are shown here.

The plot of extinction coefficient was in accordance with the absorbance spectra of the phosphorylated and unphosphorylated LG7 and KK9 peptides. High concentration was used due to weak absorption. This may also cause aggregation. However, the polypeptide backbone in the unfolded phosphorylated and unphosphorylated peptide structures can facilitate charged terminals' interactions among aggregates and increase the number of contacts among charged residues increasing ProCharTS absorbance.

The increase in ProCharTS absorbance in the case of phosphorylated LG7 suggests that there is an increase in the overall charge content of the peptide and there may be increase in charge transfer occurring due aggregation. The so called neutral amino acid, serine, is phosphorylated in this case, which behaves as an anionic species and enhances charge transfer in the peptide. The charge transfer may occur from the peptide backbone to the lysine residues, along with the charge transfer from the phosphorylated serine residue to the lysine residue present.

On the other hand, two phosphorylations in case of KK9 peptides results in the repulsion of

charge due to four extra negative charges incorporated from 2 phosphate ions. This results in diminishing aggregation and lowering of charge transfer. Hence, the unphosphorylated KK9 shows higher ProCharTS absorbance than the phosphorylated forms (KK9PP).

3.2.2 Steady-state luminescence emission of unphosphorylated and phosphorylated peptides

Furthermore, luminescence spectra [Figures 3.4 (LG7) and 3.5 (KK9)] collected at various excitation wavelengths (280–410 nm) revealed significant differences between phosphorylated and unphosphorylated peptides, underscoring the sensitivity of ProCharTS to phosphorylation states.

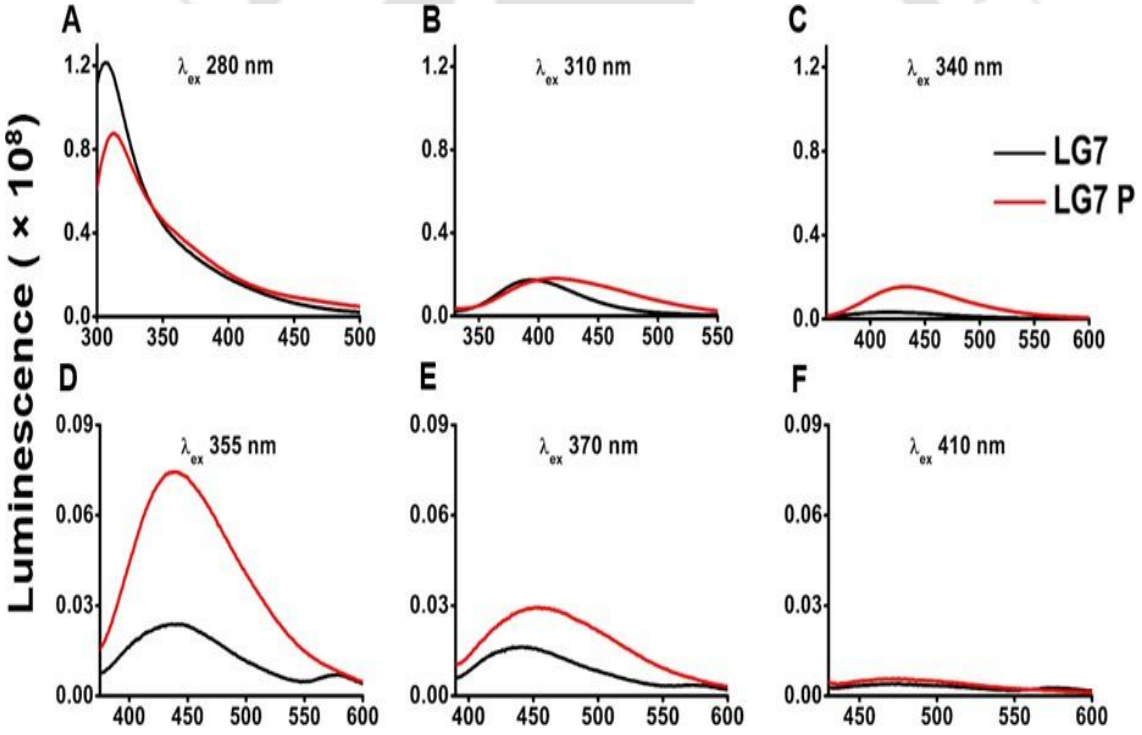

Figure 3.4: Luminescence spectra of LG7 and LG7 P (A-F) peptides at different excitation wavelengths. All excitations were performed with a 2 nm slit width, and emission was collected with a 15 nm slit width. Peptide concentrations used were 2 mM in water.

Luminescence emission spectra for phosphorylated and unphosphorylated LG 7 and KK 9 peptides were collected in the wavelength ranges 300-500, 330-550, 360-600, 375-600, 390-600, and 430-600 nm, respectively, when excited at the corresponding wavelengths: 280,

310, 340, 355, 370, and 410 nm, as seen in Figures 3.4 and 3.5. We observed that although the luminescence at 280 nm excitation in both cases showed varied spectra from the ProCharTS absorbance samples, the luminescence spectrum for all the remaining excitations behaved similarly.

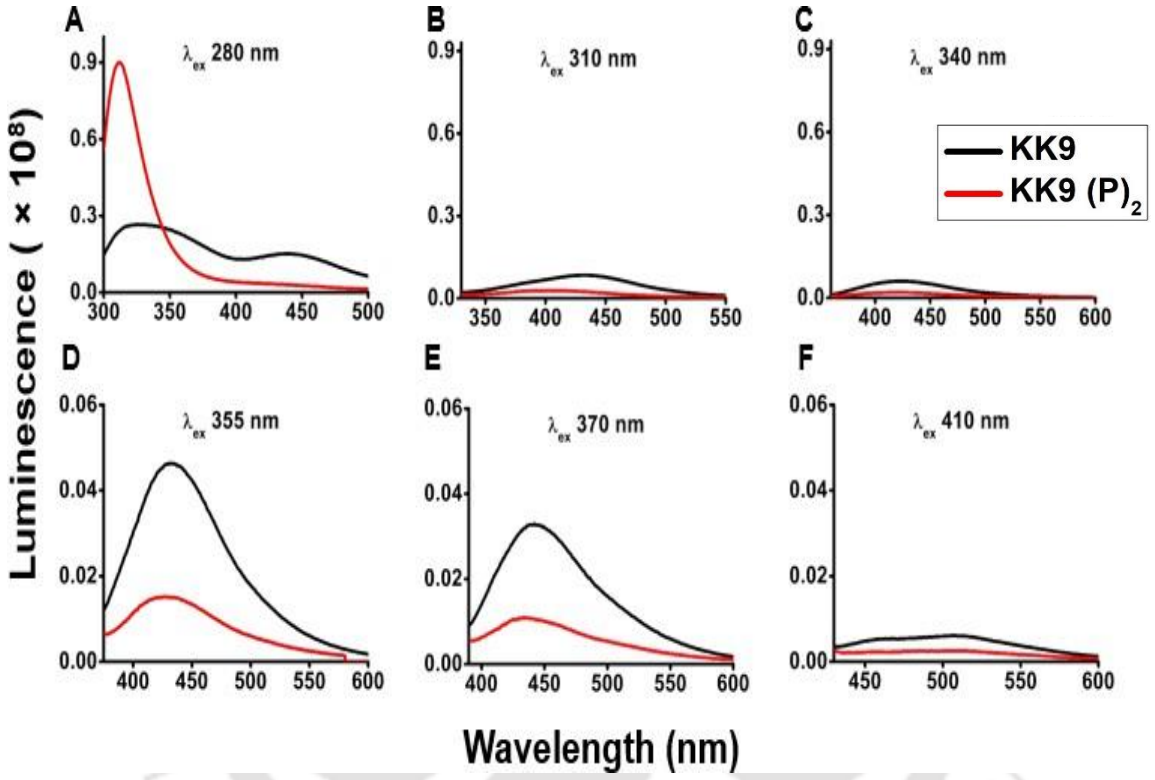

Figure 3.5: Luminescence spectra of KK9 and KK9(P)$_2$ (A-F) peptides at different excitation wavelengths. All the excitations were done with a 2 nm slit width, and emission was collected with a 15 nm slit width. Concentrations of peptides used were 2 mM in water.

The similarity between the ProCharTS absorbance and luminescence spectra suggests that the charge transfer is occurring due to phosphorylation in peptides. Hence, ProCharTS could detect phosphorylation in peptides. Although the structure of the peptides is unknown, the charge transfer due to spatial proximity is not confirmed. This intrigued us to use proteins that involve the polypeptide backbone, as well as arising from folded 3D structure, in the charge transfer within the protein due to phosphorylation.

3.2.3 Purity of alpha-casein proteins and beta-casein proteins

The purity of the casein proteins was evaluated with the 15% SDS-PAGE. Figure 3.6 shows a single band of the phosphorylated alpha-casein protein and the beta-casein protein. These proteins were commercially purchased from Sigma-Aldrich.

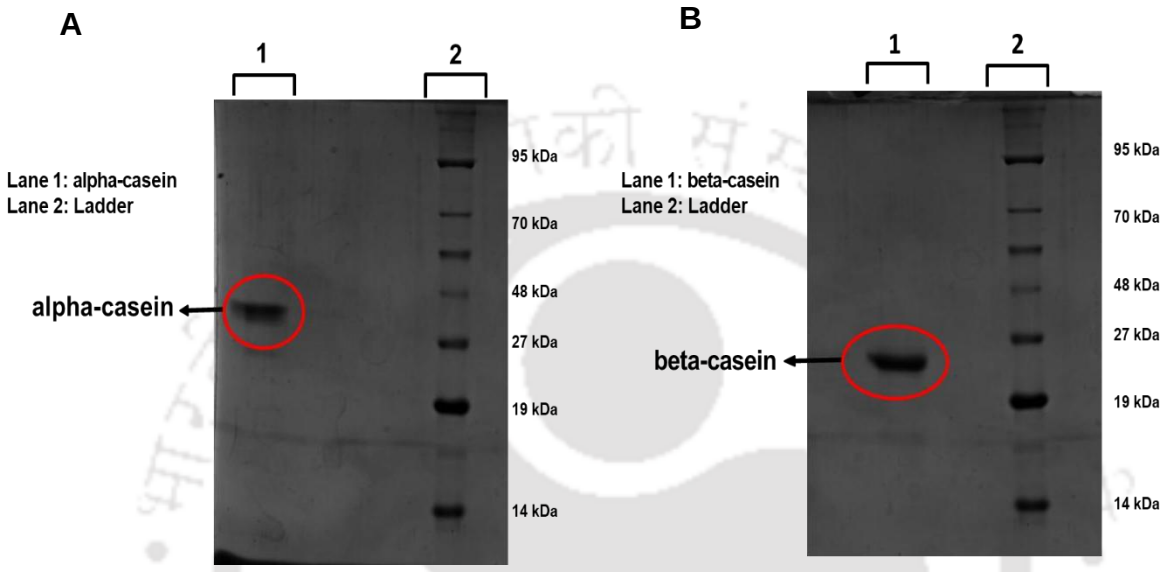

Figure 3.6: A 15% SDS PAGE gel was run using the (panel A) phosphorylated alpha-casein protein and (panel B) phosphorylated beta-casein protein.

The mass of the phosphorylated alpha-casein and beta-casein was also confirmed using Matrix Assisted Laser Desorption/Ionization (MALDI) spectra (Figure 3.7).

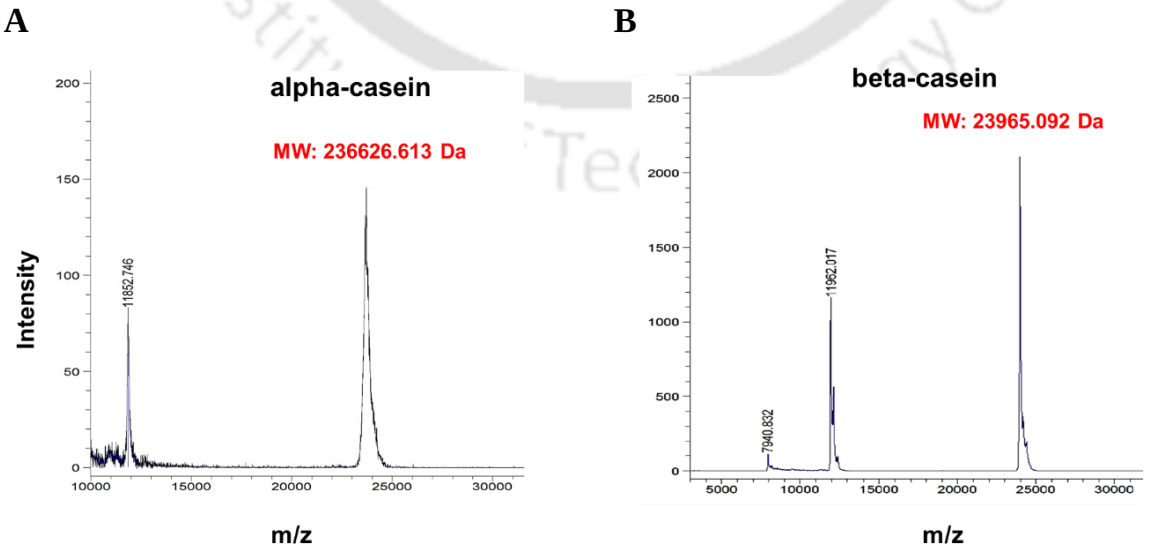

Figure 3.7: MALDI spectra for the phosphorylated (panel A) alpha-casein and (panel B) beta-

casein proteins.

The mass and the single band showed that the proteins were in the phosphorylated form. The mass of the phosphorylated alpha-casein observed was 23699.001 Da, which was approximately 629 Da more than the unphosphorylated mass calculated from the sequence of the protein. Similarly, the mass of the phosphorylated beta casein observed was 23965.092 Da, which was approximately 408 Da more than the unphosphorylated mass calculated from the sequence of the beta casein protein. The mass difference of 629 Da equals approximately 8 phosphate molecules per alpha casein protein, and the mass difference of 408 Da equals approximately 5 phosphate molecules per beta casein protein.

3.2.4 Dephosphorylation of alpha-casein and beta-casein proteins

The phosphorylated alpha-casein and beta-casein were subjected to a dephosphorylation assay using bovine alkaline phosphatase. The activity of the alkaline phosphatase (AlP) enzyme was evaluated using the pNPP assay.

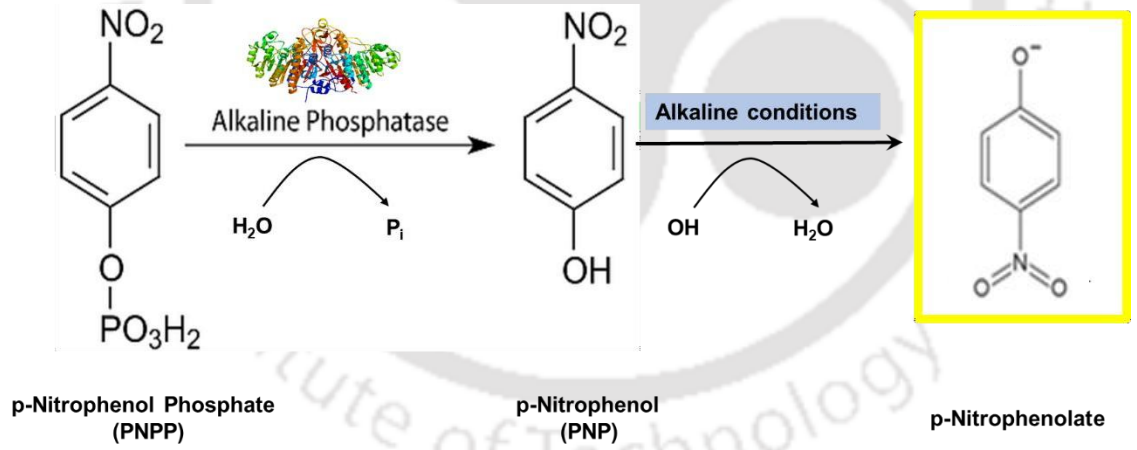

Figure 3.8: pNPP Assay reaction catalyzed by Alkaline Phosphatase (ALP) enzyme. (Adapted from Tang et al., 2019).

In this assay, AlP catalyzes the hydrolysis of the substrate pNPP to produce a yellow-colored product, para-nitrophenolate, under alkaline conditions. The product formation was monitored by measuring absorbance at 405 nm. As depicted in Figure 3.9, the absorbance reached a plateau over time, indicating that the substrate was completely and efficiently dephosphorylated by AlP.

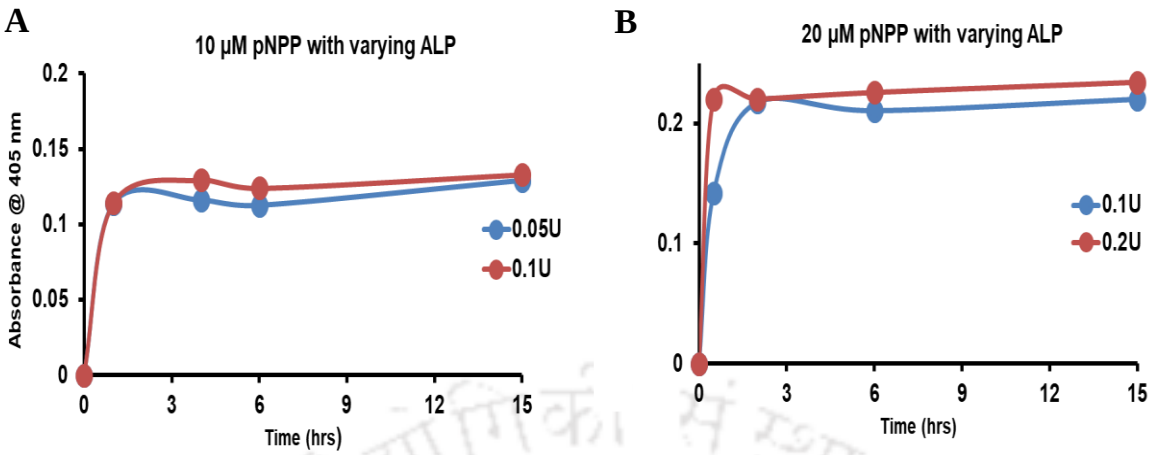

Figure 3.9: PNPP Assay- Formation of pNP was monitored for 15 hours at different time points. Figure A shows a plot with 10 µM substrate with 0.05 U and 0.1 U of enzyme at room temperature. Figure B shows a plot with 20 µM substrate with 0.1 U and 0.2 U of enzyme at room temperature.

The dephosphorylation of alpha-casein and beta-casein was then carried out using alkaline phosphatase and the products of the reaction were analyzed using SDS PAGE and MALDI.

3.2.5 SDS PAGE to confirm Dephosphorylation

The dephosphorylation of the alpha casein and beta casein proteins was confirmed using SDS PAGE as shown in Figure 3.10. In case of alpha-casein, the downward shift in the protein band upon dephosphorylation was evident (Figure 3.10A). On the other hand, in the case of beta-casein, the shift in the band was not very evident (Figure 3.10B) as the change in mass is very less in this case, which is not well resolved in SDS PAGE. The casein proteins tend to show anomalous behavior in the SDS PAGE. Hence, detection of mass change upon dephosphorylation with the help of SDS PAGE is not very reliable. Although the shift showed that dephosphorylation has occurred.

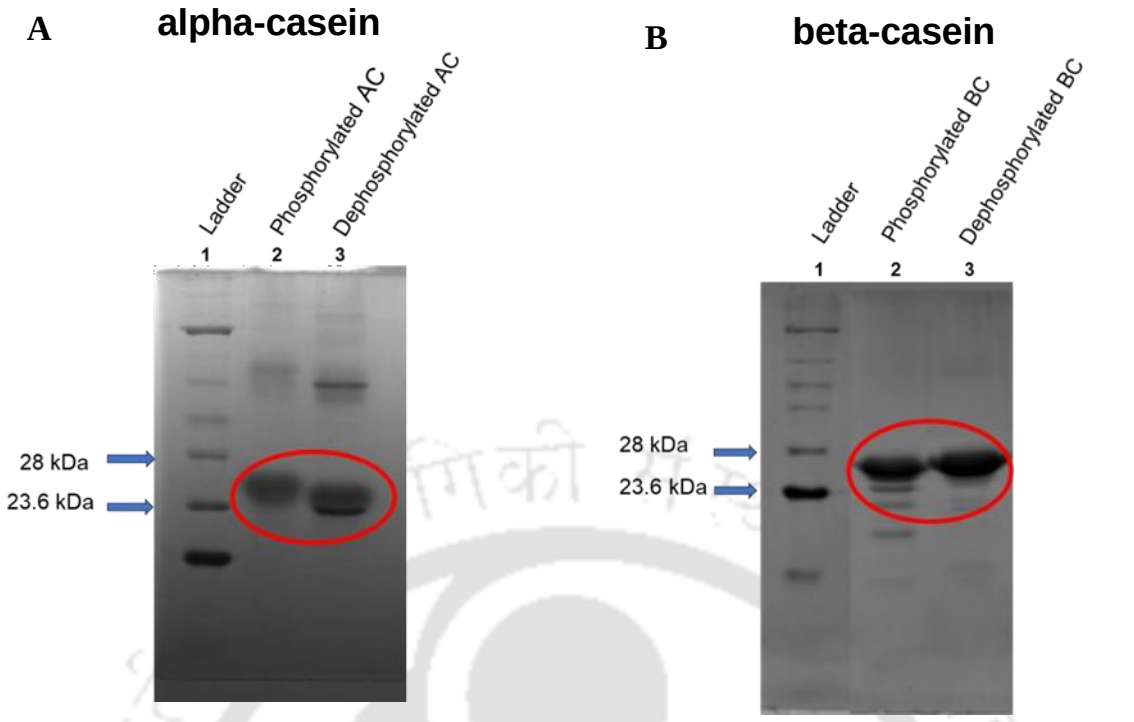

Figure 3.10: SDS-PAGE of phosphorylated and dephosphorylated alpha-casein and beta-casein.

3.2.6 MALDI to detect Dephosphorylation

The protein phosphorylation quantification was performed using MALDI as depicted in Figure 3.11. The change in mass upon dephosphorylation in the case of alpha casein (Figure 3.11A) was 629.2 Da, which is approximately equal to the mass of 8 phosphates (weight per phosphate being 78 Da), thus confirming the protein was completely dephosphorylated.

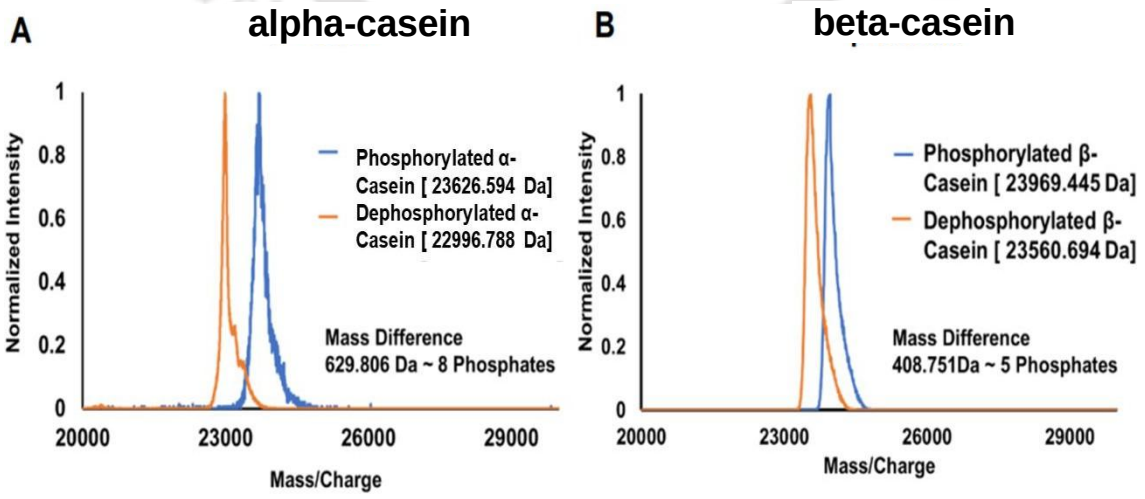

Figure 3.11: MALDI spectra of phosphorylated and dephosphorylated A. alpha-casein and B.

beta-casein after 18 hours and 12 hours reactions, respectively.

Figure 3.11B, it is shows that the change in mass upon dephosphorylation of beta-casein protein was 408.751 Da, which is equal to the mass of 5 phosphates (weight per phosphate being 78 Da). Hence, the beta-casein was completely dephosphorylated after the reaction. The change in mass observed has been tabulated in Table 3.1.

A

ALP, α-Casein	Phosphorylation state	Molecular Mass (Da)	Mass Difference (Da)	No. of Phosphates (/78 Da)
5 units, 25 µM	Phosphorylated α-Casein	23626.594	629.212	8.07
	Dephosphorylated α-Casein	22996.788	------	------

B

ALP, β-Casein	Phosphorylation state	Molecular Mass (Da)	Mass Difference (Da)	No. of Phosphates (/78 Da)
5 units, 50 µM	Phosphorylated β-Casein	23969.445	408.751	5.24
	Dephosphorylated β-Casein	23560.694	------	------

Table 3.1: Experimentally determined mass of phosphorylated and dephosphorylated Panel A. alpha-casein and Panel B. beta-casein from MALDI spectra.

Hence, from MALDI measurements, it was confirmed that the alpha-casein and beta-casein were completely dephosphorylated after 18 hours, in the case of alpha-casein, and 12 hours in the case of beta-casein. The proteins were then used for the detection of phosphorylation using ProCharTS.

3.2.7 Detection of phosphorylation using ProCharTS absorbance

The absorption spectra of both the phosphorylated and dephosphorylated forms of alpha-casein and beta-casein proteins were recorded, as illustrated in Figure 3.12. Upon dephosphorylation, a significant increase in the ProCharTS signal was observed for both

alpha-casein and beta-casein. This enhancement in signal intensity suggests that the removal of phosphate groups leads to structural or environmental changes in the proteins that increase their interaction with the surroundings and enhance ProCharTS. These changes may reflect alterations in the local polarity, charge distribution, or conformational state of the proteins, thereby enhancing their spectroscopic response following dephosphorylation.

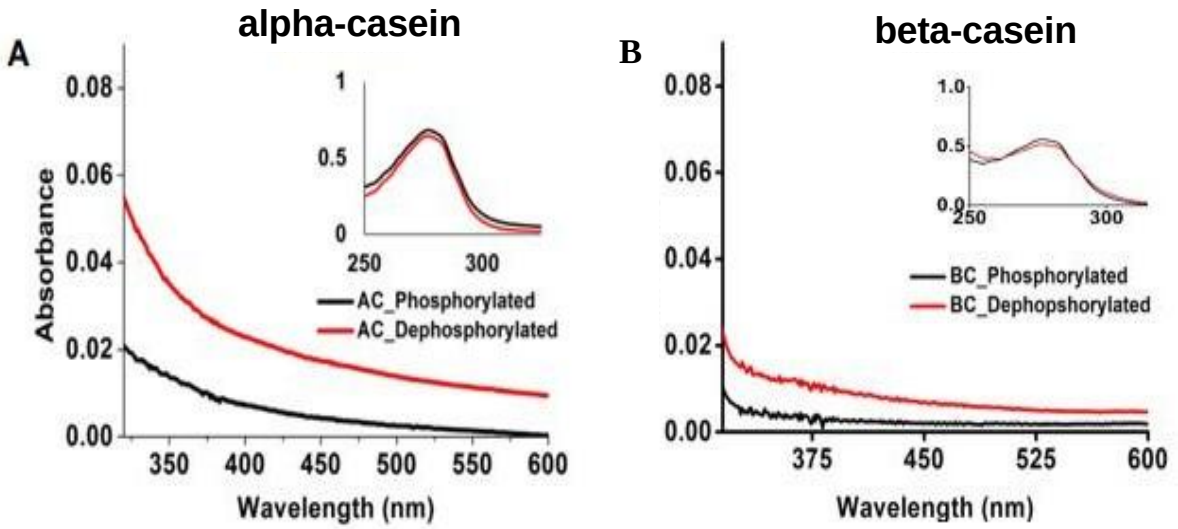

Figure 3.12: Absorbance spectra of A. phosphorylated and dephosphorylated (24 h reaction) alpha-casein (25 µM) and B. phosphorylated and dephosphorylated (12 h reaction) beta-casein (45 µM). The inset shows the spectra from 250 to 320 nm.

The dephosphorylated forms of alpha-casein and beta-casein proteins showed a pronounced increase in absorbance when monitored using the ProCharTS probe, in comparison to their phosphorylated forms. This significant enhancement in signal intensity suggests that

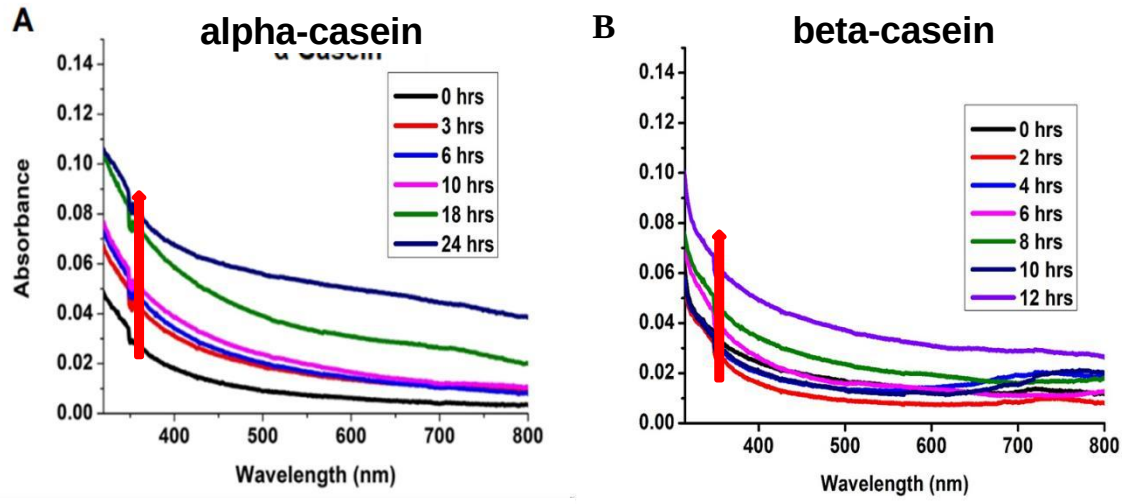

Figure 3.13: Time dependent changes in absorbance observed at different time points is shown for A. alpha- casein (45 µM) and B. beta-casein (100 µM) upon dephosphorylation.

dephosphorylation induces changes in the local molecular environment of the proteins, which in turn promotes more efficient charge transfer interactions with the ProCharTS probe.

The removal of negatively charged phosphate groups likely alters the electrostatic landscape and protein conformation, leading to greater exposure of specific residues or domains that participate in the charge transfer mechanism. These structural and electrostatic modifications contribute to the observed spectral shift and increased absorbance. Figure 3.14 illustrates the time-dependent progression of this effect, with the ProCharTS absorbance being recorded at various time intervals following the initiation of dephosphorylation. The data clearly demonstrate a gradual rise in absorbance over time, indicating that the extent of dephosphorylation correlates with the magnitude of charge transfer enhancement.

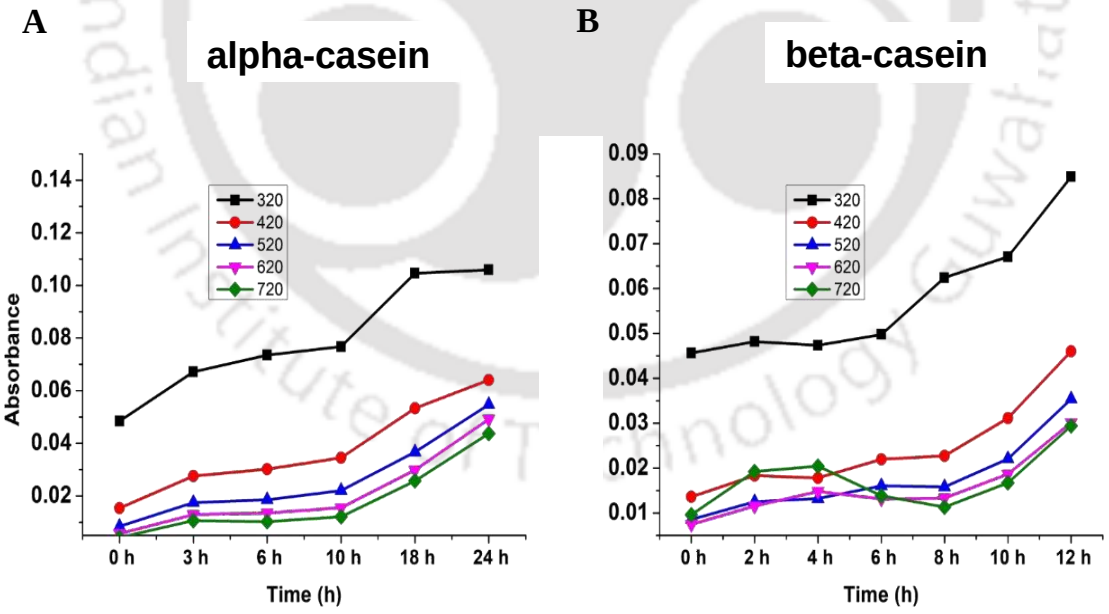

Figure 3.14: Time dependent changes in absorbance observed at multiple wavelengths is shown for A. alpha-casein (45 µM) and B. beta-casein (100 µM) upon dephosphorylation.

To determine the extinction coefficients of the proteins, varying concentrations of both phosphorylated and dephosphorylated forms of the proteins were analyzed. Absorbance

spectra were recorded across the wavelength range of 315 nm to 600 nm, and the data were used to construct calibration curves for each form. As illustrated in Figure 3.15, this analysis enabled the calculation of wavelength-dependent extinction coefficients, providing insights into how phosphorylation status influences the optical properties of the proteins.

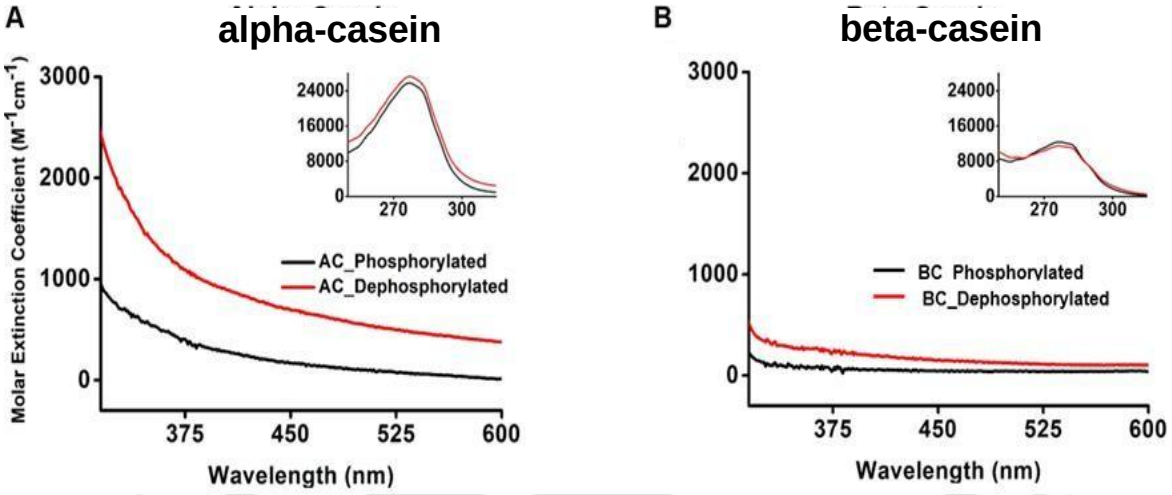

Figure 3.15: Extinction coefficient of A. phosphorylated and dephosphorylated (24 hours reaction) alpha-casein (25 µM) and B. phosphorylated and dephosphorylated (12 hours reaction) beta-casein (45 µM). The inset shows the spectra from 250 nm to 320 nm.

The absorption spectra of both the phosphorylated and dephosphorylated forms of alpha-casein and beta-casein proteins were recorded and are presented in Figure 3.12. A significant enhancement in the ProCharTS signal was observed for both alpha-casein and beta-casein following dephosphorylation. Specifically, the dephosphorylated forms exhibited a pronounced increase in absorbance compared to their phosphorylated counterparts. This increase suggests a greater extent of charge transfer interactions occurring as a result of the removal of phosphate groups. The elevated ProCharTS absorbance in the dephosphorylated proteins implies that dephosphorylation induces structural or electronic changes that enhance charge transfer properties. High extinction coefficient values of dephosphorylated form reveal significant increase in absorption for alpha-casein in comparison to beta-casein. Hence, ProCharTS absorbance could detect phosphorylation in alpha-casein and beta casein protein.

3.2.8 Detection of phosphorylation using ProCharTS Luminescence

Figures 3.16 show the ProCharTS luminescence of both the phosphorylated and dephosphorylated forms of alpha casein (Figure 3.16A-D) and beta(3.16E-H) casein proteins

at multiple excitation wavelength.

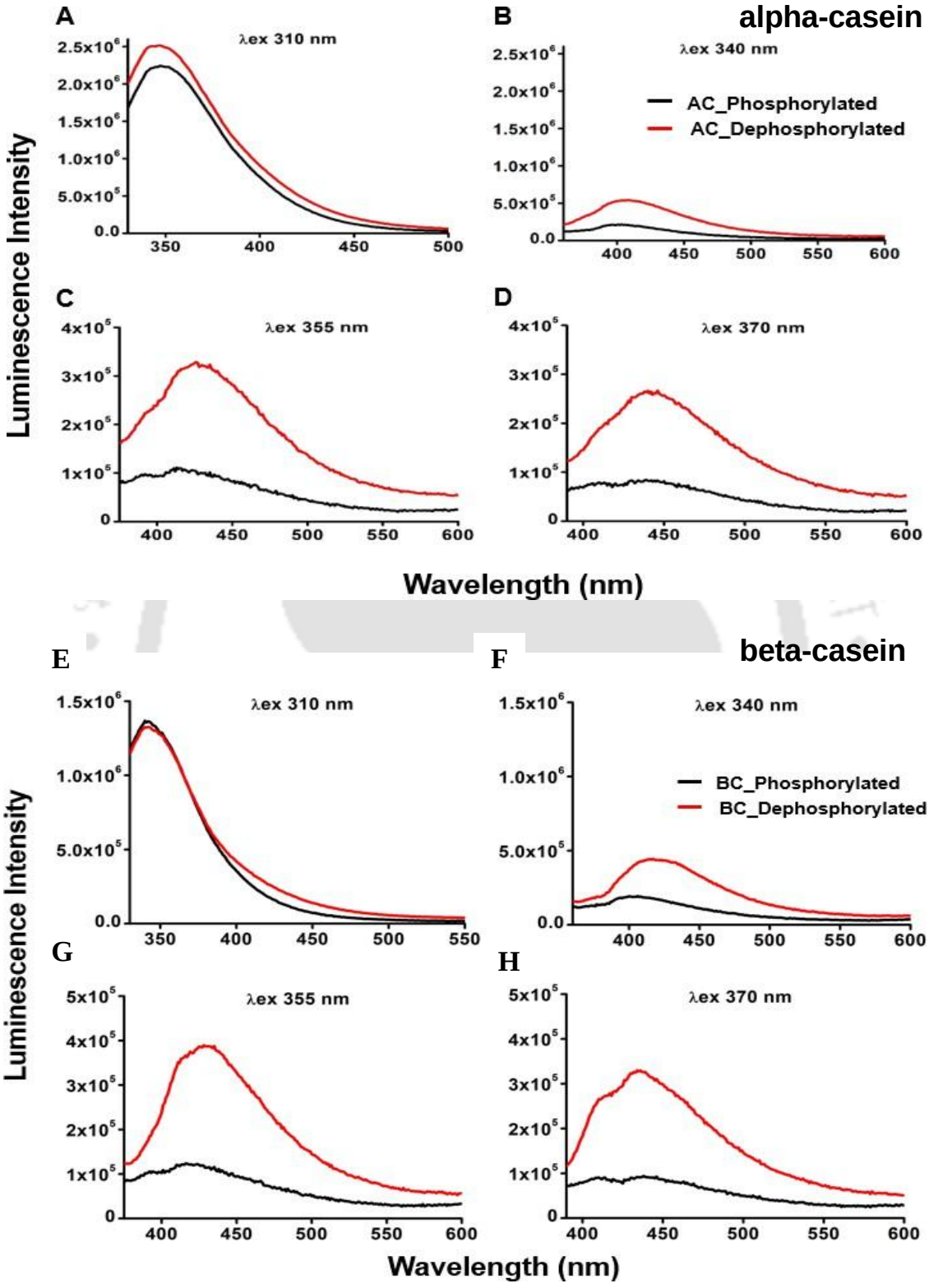

Figure 3.16: Luminescence of phosphorylated and dephosphorylated alpha-casein (panel A-D) and beta-casein (panel E-H) at different excitation wavelengths. All the excitations were done with 2 nm slit width and emission was collected with 10 nm slit width. Concentrations of

proteins used were 25 µM (alpha-casein) and 45 µM (beta-casein). The luminescence was averaged over 5 scans.

The emission profiles of the dephosphorylated proteins consistently demonstrated enhanced charge recombination characteristics when compared to their phosphorylated counterparts. This enhancement is evident from the increased luminescence intensity observed in the dephosphorylated forms. The proteins were subjected to excitation at various wavelengths to comprehensively assess the influence of dephosphorylation on their photophysical properties. The observed changes suggest that removal of phosphate groups alters the electronic environment of the proteins, thereby facilitating more efficient charge transfer, and subsequent recombination.

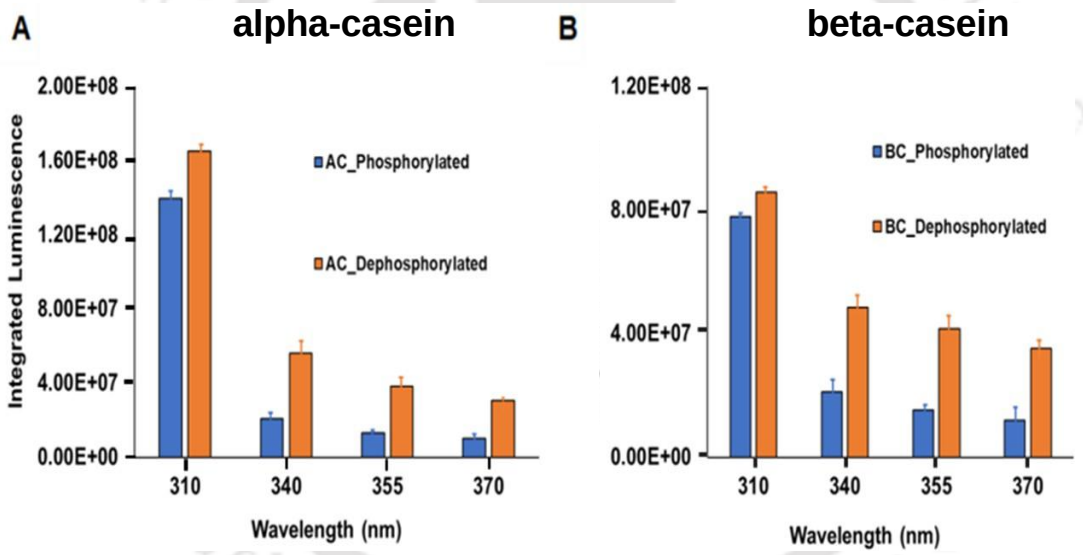

Figure 3.17: Integrated luminescence of phosphorylated and dephosphorylated A. alpha-casein and B. beta-casein at λ_{ex} = 310 nm (λ_{em} = 330-550 nm), λ_{ex}= 340 nm (λ_{em} = 360-600 nm), λ_{ex} = 355 nm (λ_{em} = 375-600 nm) and λ_{ex} = 370 nm (λ_{em} = 390-600 nm). All the excitations were done with 2 nm slit width and emission was collected with 10 nm slit width. Concentrations of proteins used were 25 µM (alpha-casein) and 45 µM (beta-casein).

Upon excitation at longer wavelengths, a decrease in luminescence intensity was observed (Figure 3.17), which is a characteristic feature of ProCharTS behavior. This wavelength-dependent decline in emission suggests that the charge transfer efficiency diminishes with lower excitation energy, consistent with the known photophysical properties of ProCharTS.

There was a similarity in luminescence profile to that of the absorbance profile of both the phosphorylated and dephosphorylated forms of alpha-casein and beta-casein proteins. The dephosphorylated forms of the alpha-casein and beta-casein proteins showed higher ProCharTS absorbance and luminescence as compared to the phosphorylated form.

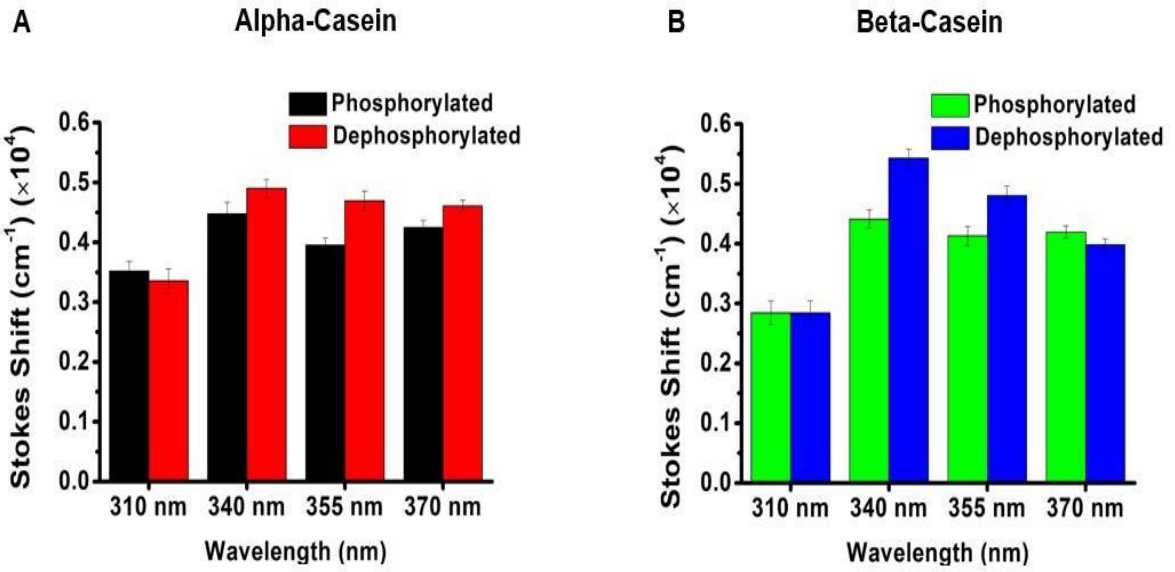

Figure 3.18: Stokes shift of different proteins as a function of excitation wavelength. Concentration of alpha-casein proteins taken was 30 µM and beta-casein proteins was 45 µM.

The Stokes shift from the emission spectra was calculated for each sample and plotted as a function of excitation wavelength, as shown in Figure 3.18. The dephosphorylated samples showed significantly higher Stokes shift at all wavelengths (4500-5800 cm^{-1}) than the phosphorylated samples. A possible explanation of this high Stokes Shift is a significantly greater loss in excitation energy, in the form of rapid internal conversion and solvent relaxation. However, a general decreasing trend of the Stokes shift with increasing excitation wavelength was observed. The Stokes shift decreased steeply from around ~5500 to ~3800 cm^{-1} in beta-casein specifically. These higher stokes shifts are characteristics of Protein Charge Transfer Spectra [Kumar et al., 2020].

The observed increase in ProCharTS absorbance and luminescence signals upon dephosphorylation prompted further investigation to uncover the underlying cause of this phenomenon. Previous work by Kaudelka et al. (2009) suggested the possibility of a subtle

gain in α-helical structure near the N-terminal region of casein proteins following dephosphorylation. Their study employed ANS fluorescence assays and circular dichroism (CD) spectroscopy to demonstrate that both alpha-casein and beta-casein undergo structural reorganization, particularly around the N-terminus, upon the removal of phosphate groups. Motivated by these findings, I conducted similar experiments including ANS binding assays and CD spectroscopy to examine whether structural changes upon dephosphorylation could account for the altered ProCharTS response. These experiments aimed to confirm whether the variations in ProCharTS signals were indeed correlated with secondary structure gain in the dephosphorylated forms of the proteins.

3.2.9 Detection of phosphorylation using ANS assay

8-Anilinonaphthalene-1-sulfonic acid (ANS) is a commonly used extrinsic fluorescent probe for investigating protein conformational changes, especially those associated with the exposure of hydrophobic regions. In aqueous environments, ANS exhibits very low intrinsic fluorescence due to its high polarity and lack of interaction with nonpolar surroundings. However, upon binding to hydrophobic patches on partially folded or conformationally altered proteins, ANS undergoes a substantial increase in fluorescence intensity along with a characteristic blue shift in its emission maximum. This makes ANS an effective tool for detecting structural transitions, protein unfolding, or exposure of hydrophobic domains that are typically buried in the native state.

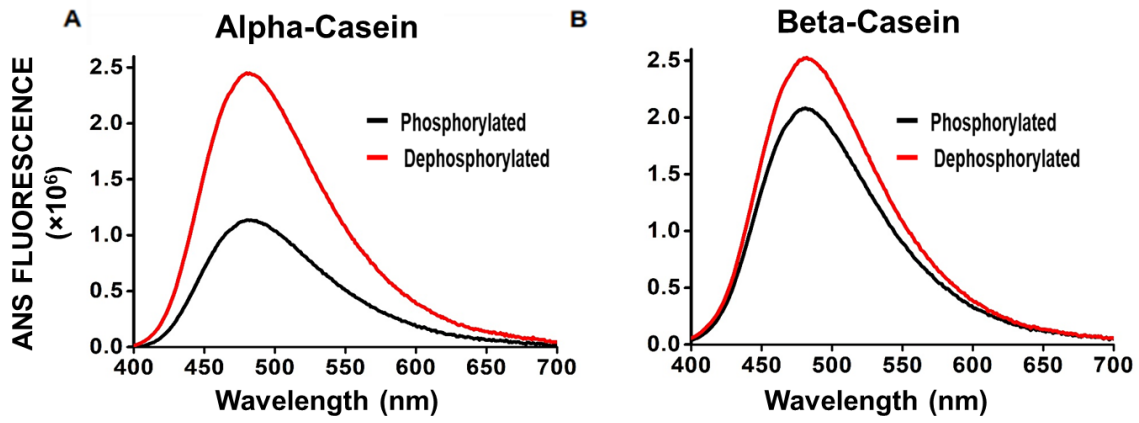

Figure 3.19: Panels A and B show the ANS fluorescence spectra of phosphorylated and dephosphorylated forms of alpha-casein (10 µM) and beta-casein (10 µM), respectively, recorded at an excitation wavelength of 380 nm.

Using ANS fluorescence spectroscopy, I observed a significant increase in fluorescence intensity for both α-casein and β-casein upon dephosphorylation. As shown in Figure 3.19, the ANS fluorescence spectra of the dephosphorylated forms exhibit higher intensity compared to their phosphorylated counterparts. This enhancement suggests that dephosphorylation induces conformational changes in the proteins, leading to the exposure of previously buried hydrophobic regions. These exposed hydrophobic sites provide more binding opportunities for the ANS probe, thereby increasing its fluorescence signal. The results support the hypothesis that removal of phosphate groups alters the structural organization of casein proteins, potentially contributing to the observed changes in ProCharTS response as well.

The integrated ANS fluorescence intensity, as shown in Figure 3.20, revealed a marked increase upon dephosphorylation of both alpha-casein and beta-casein. This enhancement suggests increased binding of ANS, particularly its sulfonate moiety, to the exposed hydrophobic regions of the protein.

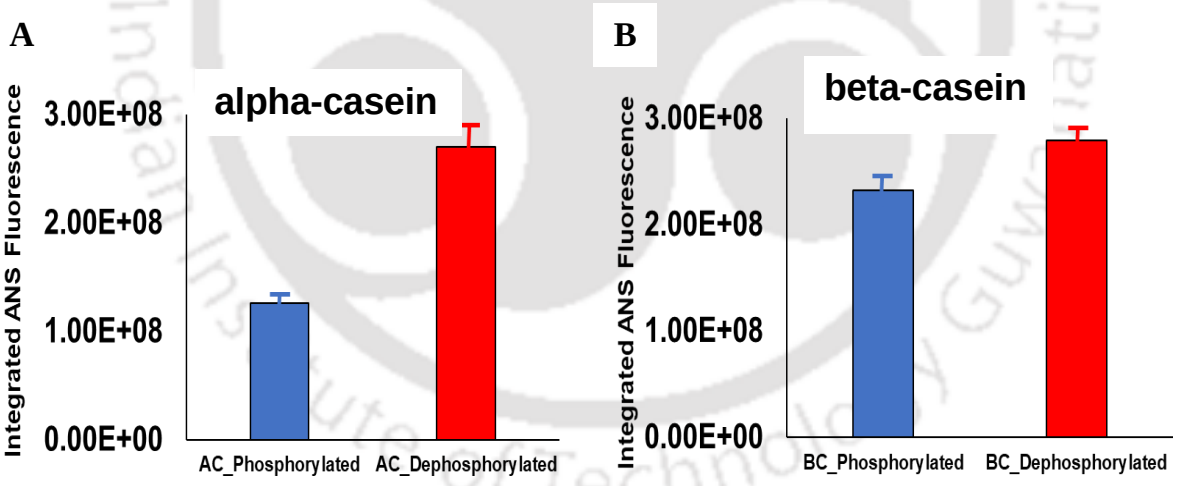

Figure 3.20: Panels A and B shows the integrated ANS fluorescence (λ_{em} = 400-700 nm) for Phosphorylated and dephosphorylated alpha-casein (10 µM) and beta-casein (10 µM).

In the phosphorylated forms, the presence of negatively charged phosphate groups likely creates electrostatic repulsion with the negatively charged sulfonate group of ANS, thereby limiting its binding affinity. Upon dephosphorylation, this repulsion is reduced, facilitating stronger ANS–protein interactions and resulting in higher fluorescence intensity. These

findings further support the hypothesis that dephosphorylation alters the protein's conformation to expose hydrophobic domains. Consequently, the observed increase in ProCharTS response upon dephosphorylation is consistent with the structural changes detected by ANS fluorescence.

3.2.10 Detection of secondary structure change upon dephosphorylation

To further validate the structural changes observed through ANS fluorescence, Circular Dichroism (CD) spectroscopy was performed. CD spectroscopy provides valuable insights into the secondary structure content of proteins, such as the presence of α-helices, β-sheets, and random coils. Figure 3.18 (Panels A and B) displays the far-UV CD spectra of both the phosphorylated and dephosphorylated forms of alpha-casein and beta-casein, respectively. Comparative analysis of these spectra allows for the assessment of changes in secondary structural elements resulting from dephosphorylation, offering additional evidence to support conformational rearrangements in the proteins.

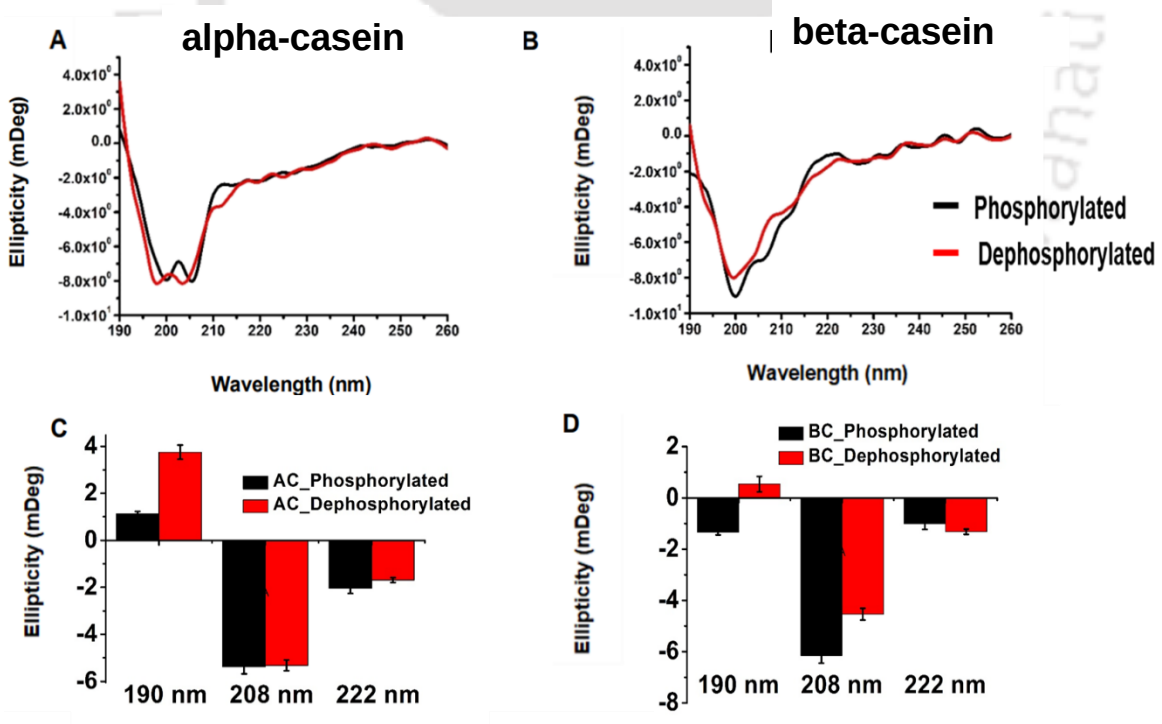

Figure 3.21: CD spectra for phosphorylated and dephosphorylated alpha-casein and beta-casein (A and B respectively). C and D shows the changes observed at 190 nm, 208 nm and 220 nm. Protein Concentration taken was 3 µM.

A pronounced change in ellipticity is observed at 190 nm for both alpha-casein and beta-casein upon dephosphorylation, indicating alterations in their secondary structure. Additionally, beta-casein shows a notable change at 208 nm, while the signal at 222 nm remains largely unchanged in both proteins. These spectral features, as summarized in the bar graphs of Figures 3.21C and 3.21D, suggest that dephosphorylation leads to subtle conformational rearrangements, including a modest gain in α-helical content.

3.2.11 Mechanism of charge transfer following casein dephosphorylation:

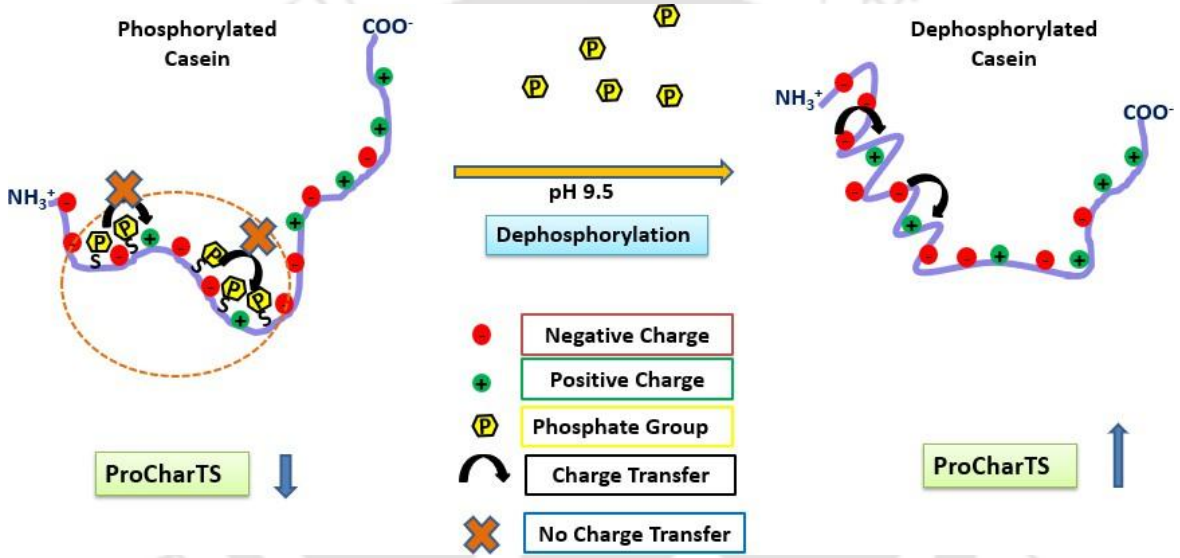

Figure 3.22: Illustration of the phenomenon behind the charge transfer occurring after casein dephosphorylation.

The schematic in Figure 3.22 provides a conceptual understanding of how charge transfer is influenced by the phosphorylation state of casein proteins. It visually represents the electrostatic environment and the structural changes that occur upon removal of phosphate groups.

In casein proteins, the phosphate groups are predominantly located near the N-terminal region. Sequence analysis also reveals that most of the negatively charged amino acid residues such as glutamate and aspartate are clustered toward this same N-terminal region. This results in a highly negative charge density in phosphorylated casein proteins.

The accumulation of negatively charged phosphate groups alongside other negatively charged residues leads to significant electrostatic repulsion. This dense negative environment hinders effective intramolecular or intermolecular charge transfer processes, thereby reducing the ProCharTS signal in phosphorylated forms of the protein. Upon dephosphorylation, the removal of double negative phosphate groups alleviates this repulsion, leading to a more favorable environment for charge transfer. This shift is detected as an increase in the ProCharTS absorbance and luminescence signals, confirming the sensitivity of the technique to changes in electrostatic interactions and supporting its utility in monitoring phosphorylation events. This interpretation is consistent with earlier findings by Darewich et al. (2000). Such structural changes are likely to contribute to enhanced charge-transfer transitions, as reflected in the increased ProCharTS response observed upon dephosphorylation.

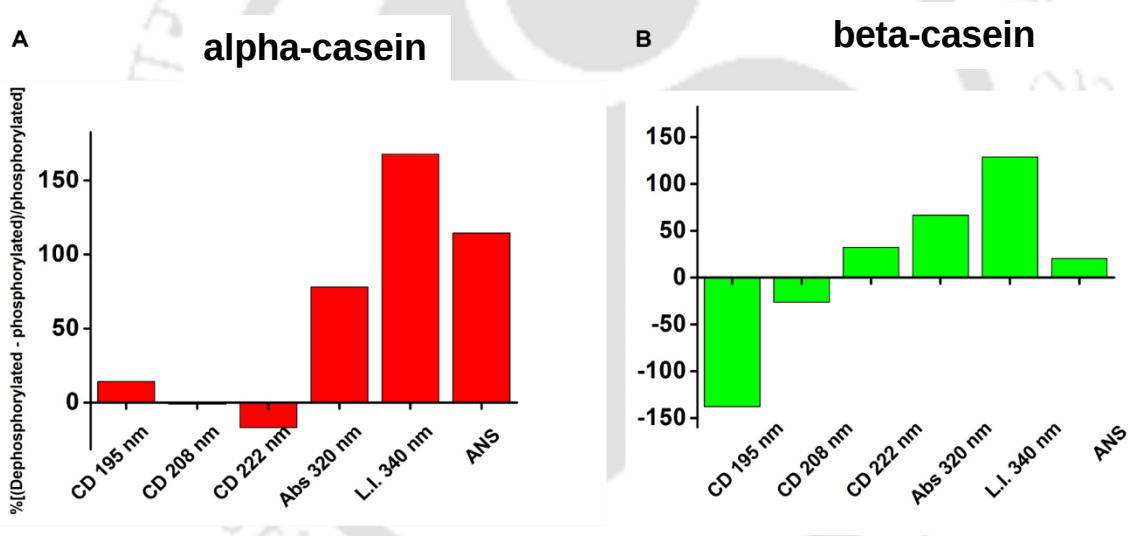

Figure 3.23: Percentage change detected in the dephosphorylated state as compared to phosphorylated states of alpha and beta caseins in the various techniques compared.

To summarize the findings, a comparative plot was generated incorporating results from various techniques used to detect phosphorylation, including ProCharTS absorbance and luminescence data (Figure 3.23). The analysis clearly demonstrated that Protein Charge Transfer Spectra (ProCharTS) is a comparatively efficient and sensitive method for detecting dephosphorylation in proteins. The distinct optical responses associated with the phosphorylation state underscore the potential of ProCharTS as a reliable tool for monitoring such post-translational modifications. Furthermore, these results suggest broader

applicability of this technique, opening new avenues for the detection and characterization of other post-translational modifications across a wide range of proteins.

3.3 Conclusion

- **Phosphorylation-induced charge redistribution influences ProCharTS signals:** Phosphorylation and dephosphorylation events introduce or remove negatively charged phosphate groups on serine, threonine, or tyrosine residues in proteins. These modifications significantly alter the local and overall electrostatic environment of the protein. As a result, the proximity and distribution of charged residues are dynamically modulated. Protein Charge Transfer Spectroscopy (ProCharTS) is sensitive to these changes in charge distribution, and it registers them as measurable variations in its absorbance or luminescence profile. These spectral shifts provide a direct, non-destructive readout of the phosphorylation state of the protein.

- **Sensitivity of ProCharTS is comparable to well-established analytical techniques:** The effectiveness of ProCharTS in detecting phosphorylation events is on par with widely used biochemical and biophysical techniques, including Circular Dichroism (CD) spectroscopy, MALDI-TOF mass spectrometry, and SDS-PAGE. While CD spectroscopy gives insight into changes in secondary structure, and mass spectrometry and SDS-PAGE provide molecular weight-based detection of phosphorylation, ProCharTS offers a unique advantage by simultaneously reflecting both charge redistribution and subtle conformational changes, without requiring extensive sample preparation or labelling.

- **Dynamic monitoring of structural and charge-related changes:** ProCharTS is particularly well-suited for tracking dynamic alterations in protein charge and structure that result from post-translational modifications. When dephosphorylation occurs, the removal of the phosphate group neutralizes a negative charge and can lead to minor structural rearrangements. These changes are effectively captured through shifts

in ProCharTS spectra, demonstrating its ability to monitor the biochemical state of proteins in real time. As a result, ProCharTS serves not just as a detection tool but also as a powerful method for studying the kinetics and dynamics of phosphorylation-related processes.

- **Broad applicability to peptides and full-length proteins:** A major strength of the ProCharTS technique lies in its versatility. It is capable of detecting phosphorylation not only in small peptide fragments but also in larger, more complex full-length proteins. This makes ProCharTS an attractive tool for applications in both fundamental biochemical research and large-scale proteomic studies. Its adaptability across different protein types and sample conditions enhances its utility in diverse experimental setups.

CHAPTER 4

INVESTIGATING THE IMPACT OF PROTEIN AGGREGATION ON PROCHARTS USING ALPHA-SYNUCLEIN AND HUMAN LYSOZYME PROTEINS.

4.1 Introduction

Protein aggregation is a major contributing factor in the development of amyloidosis [Aguzzi & O'Connor, 2010; Fink, 1998; Sipe, 1992]. Amyloid deposits are implicated in a range of diseases, including type 2 diabetes, Alzheimer's, Parkinson's, Huntington's, and prion-related disorders [Aguzzi & Calella, 2009; Ashraf et al., 2014; Kumar et al., 2016; Mukherjee et al., 2015; Mukherjee & Soto, 2017; Olzscha et al., 2011; Pedersen & Heegaard, 2013; Ross & Poirier, 2005]. Gaining insight into the mechanisms and pathways of protein aggregation, as well as developing strategies for early detection, is essential for advancing therapeutic approaches. Among the proteins commonly studied for aggregation, alpha synuclein [Calabresi et al., 2023] and lysozyme [Swaminathan et al., 2011] serve as a well- established model.

Even though the pivotal role of alpha synuclein (α-syn) in the pathogenesis of Parkinson's disease (PD) was identified twenty-five years ago, this discovery continues to stand as a landmark in PD research [Calabresi et al., 2023]. Since the landmark report by Spillantini et al. in 1997 [Spillantini et al., 1997], research on synucleinopathies has expanded dramatically, with 84,804 publications listed in PubMed under the keyword 'synucleinopathy.' Of these, 6,433 specifically reference 'synuclein aggregation' (as of October 2022). This highlights the critical importance of studying, monitoring, characterizing, and quantifying alpha synuclein aggregation across different contexts whether *in tubo* [Calero et al., 2005; Kelly et al., 2005], *in vitro* [Jun et al., 2019], or *in vivo* [Shahmoradian et al., 2019].

Hen egg white lysozyme (HEWL), a small protein consisting of 129 amino acids [Canfield, 1963], shares approximately 60% sequence identity with human lysozyme (HuL). HEWL is a highly studied aggregating protein. HEWL aggregation has been extensively examined under various conditions, including alkaline pH [Hameed et al., 2007; Homchaudhuri et al., 2006; Ravi et al., 2014b; Sophianopoulos & Van Holde ,1961, 1964; Ansari et al., 2018] and acidic pH [Arnaudov & de Vries, 2005; Chaari et al., 2015; Hill et al., 2009; Krebs et al., 2000; Mishra et al., 2007; Ansari et al., 2018]. Extensive *in vitro* studies on the molecular

mechanisms underlying the aggregation of HEWL and human lysozyme have attracted significant attention, leading to the identification of numerous conditions that promote amyloid fibril formation through diverse pathways [Swaminathan et al., 2011].

Detecting early-stage protein aggregates *in vitro* remains challenging. Mature amyloid fibrils are typically identified using molecular dyes such as Thioflavin-T (ThT), Congo Red [Maezawa et al., 2008], and 1-anilinonaphthalene-8-sulfonate [Ladiwala et al., 2011]. Traditional methods like Atomic Force Microscopy (AFM), Transmission Electron Microscopy (TEM), Circular Dichroism (CD), and Fourier Transform Infrared Spectroscopy (FTIR) are also employed to monitor pre-fibrillar aggregates [Gregoire et al., 2012; Nilsson, 2004]. However, ThT assays lack sensitivity to oligomers [Lee et al., 2011] and suffer from fluorescence self-quenching issues [Lindberg et al., 2017]. Intrinsic probes such as tryptophan fluorescence are similarly limited in tracking aggregation [Swaminathan et al., 1994].

In this chapter, we employ Protein Charge Transfer Spectroscopy (ProCharTS) to monitor the oligomerization and fibrillation of alpha synuclein and Human Lysozyme (HuL) under both alkaline and acidic conditions. Since ProCharTS intensity strongly depends on the proximity of charged residues [Prasad et al., 2017], it offers a novel label-free method to track intermolecular events such as aggregation, which involves formation of new intermolecular contacts.

Later in the chapter, we explore luminescence arising from aggregated protein structures. Several studies have reported intrinsic fluorescence from both protein oligomers [Bhattacharya et al., 2014, 2017] and mature amyloid fibrils [Chan et al., 2013; del Mercato et al., 2007; Tikhonova et al., 2018]. This emission, often referred to as intrinsic fluorescence or intrinsic deep-blue/blue fluorescence, may arise from diverse mechanisms including electron or charge transport [Bhattacharya et al., 2017; del Mercato et al., 2007], proton transfer [Pinotsi et al., 2016], or oxidative modifications of amino acids [Tikhonova et al., 2018]. Notably, similar auto-fluorescence has also been observed in monomeric proteins and individual amino acids, where carbonyl double bonds are implicated as potential origins [Niyangoda et al., 2017].

In this study, we observe luminescence originating from alpha synuclein aggregates and HuL aggregates and attribute it to emissions from ProCharTS charge transfer states. A distinctive blue shift in the emission spectra, specifically associated with amyloid fibrils, is also identified. Collectively, this chapter demonstrates the utility of ProCharTS in detecting protein aggregates and differentiating between oligomers and fibrils via spectral shifts in luminescence at excitation wavelengths greater than 300 nm.

4.2 Results and Discussion

4.2.1 Expression and purification of alpha synuclein

To investigate the aggregation behavior of alpha synuclein, the protein was recombinantly expressed and subsequently purified for experimental analysis. The purification process employed Anion Exchange Chromatography (AEC), a technique that separates proteins based on their net charge. Specifically, a salt gradient was utilized to elute bound proteins, with alpha synuclein eluting at a concentration of 350 mM NaCl, indicating its specific ionic interactions with the chromatography resin.

The purity of the eluted alpha synuclein was assessed using reducing SDS-PAGE, a method that denatures proteins and provides information about their molecular weight and purity. A 15% acrylamide gel was used to achieve optimal resolution for low molecular weight proteins (Figure 4.1).

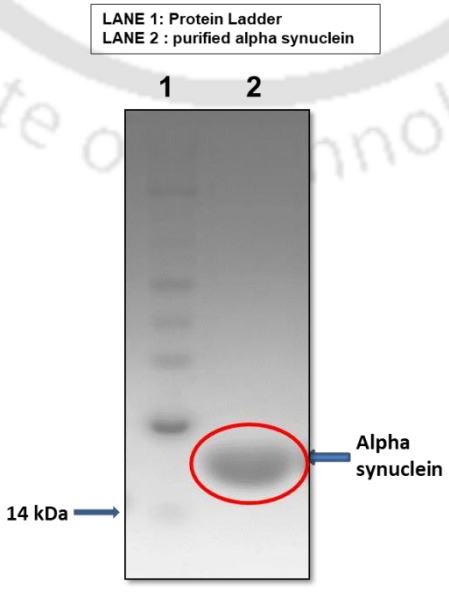

Figure 4.1: 15% Reducing SDS-PAGE showing a single band of purified proteins for alpha

synuclein (~14 kDa).

The analysis revealed a single, distinct band corresponding to α-synuclein, confirming its purity. The apparent molecular weight determined from the gel was approximately ~14 kDa, aligning with the theoretical molecular weight of monomeric alpha synuclein (14.46 kDa).

This purified alpha synuclein is suitable for downstream applications, including aggregation studies using ProCharTS, which can provide insights into the protein's propensity to form oligomers and higher order aggregates under chosen conditions.

4.2.2 Mass Spectrometry Analysis

The molecular mass of the purified alpha synuclein protein was determined using Matrix-Assisted Laser Desorption/Ionization (MALDI) mass spectrometry, a high-precision analytical technique for characterizing biomolecules. The resulting MALDI spectrum displayed a single, sharp peak corresponding to the expected molecular weight of monomeric α-synuclein (Figure 4.2). The absence of additional peaks or peak broadening indicated that the sample was free from detectable oligomeric species or degradation products, thereby confirming both the purity and monomeric state of the protein. This result validated the success of the purification protocol and ensured that the protein was suitable for downstream structural and aggregation studies.

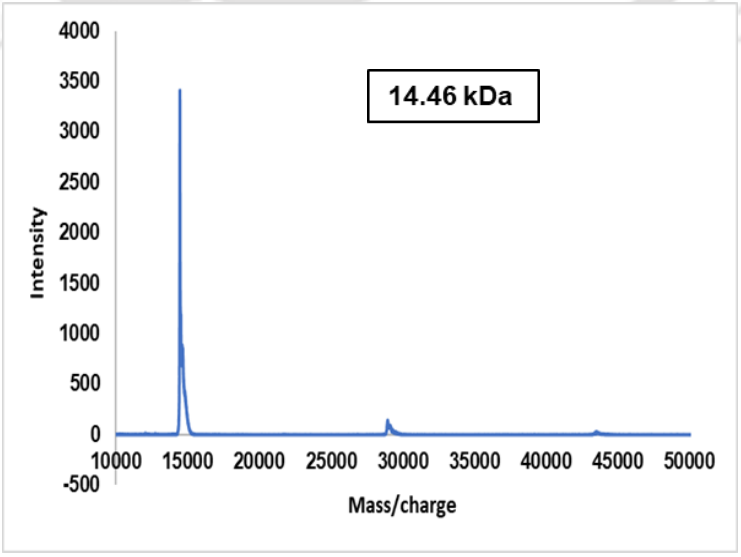

Figure 4.2: Mass spectrum of purified alpha synuclein protein present in monomeric form.

4.2.3 Detection of Alpha Synuclein protein Aggregates using ProCharTS

4.2.3.1 Spectroscopic Characterization of Monomeric Alpha Synuclein Prior to Aggregation Studies

Before initiating the aggregation experiments, the spectroscopic properties of the purified monomeric alpha synuclein were evaluated. UV–visible absorbance spectra were recorded to assess its optical characteristics. As expected for a protein lacking tryptophan and containing fewer aromatic residues, the spectra (Figure 4.3A) revealed a very low molar extinction coefficient, consistent with alpha synuclein's amino acid composition and limited aromatic chromophore content (6 in number with no tryptophan residue).

Circular Dichroism (CD) spectroscopy was subsequently performed to determine the secondary structure of the purified protein. The CD spectrum exhibited a characteristic profile of an intrinsically disordered protein, with a strong negative ellipticity near 200 nm, indicative of a predominantly random coil conformation (Figure 4.3B).

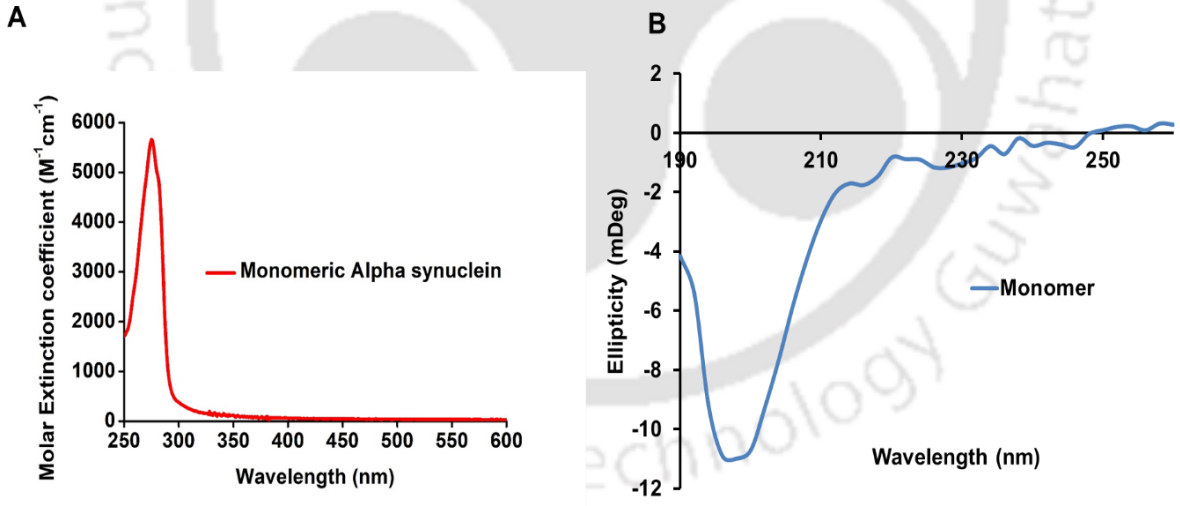

Figure 4.3: Panel A. Absorbance of 50 µM Alpha Synuclein which was purified through Anion Exchange Chromatography. Extinction coefficient of protein is 5600 M-1 cm-1 ($\lambda_{280\ nm}$). Panel B. CD spectra of 2 µM monomeric alpha synuclein protein.

These findings confirmed that the purified alpha synuclein was in a monomeric, natively unfolded state, thereby providing a well-defined starting point for subsequent aggregation studies.

4.2.3.2 CD Spectroscopy of alpha synuclein aggregation

Aggregation experiments were initiated using monomeric alpha synuclein at a concentration of 100 μM, prepared in 25 mM phosphate-buffered saline (PBS, pH 7.4) supplemented with 150 mM NaCl. The samples were incubated under constant agitation at 300 rpm and 37 °C for a period of 10 hours. Notably, the onset of aggregation was observed only after approximately 6 hours of incubation under these conditions.

As illustrated in Figure 4.4, the freshly prepared protein exhibited a circular dichroism (CD) spectrum characteristic of a predominantly random coil structure. With the progression of aggregation, a gradual decrease in ellipticity at 220 nm was recorded (Figure 4.4B), which is indicative of the transition from random coil to β-sheet-rich structures, a hallmark of early aggregation intermediates. Although slight sigmoidal decrease in ellipticity at 220 nm typically representing a structural transition was not strongly evident, the flattening trend of the curve suggested partial β-sheet formation during the monitored time frame. This likely reflects the fact that the study was restricted to the initial stages of aggregation, prior to extensive fibril maturation.

At later time points, the protein aggregates became insoluble, leading to precipitation, which complicates spectroscopic monitoring due to light scattering effects from mature fibrils. For this reason, the analysis was focused on the early aggregation phase, where soluble oligomeric species predominate and provide meaningful insights into the initial structural transitions of alpha synuclein.

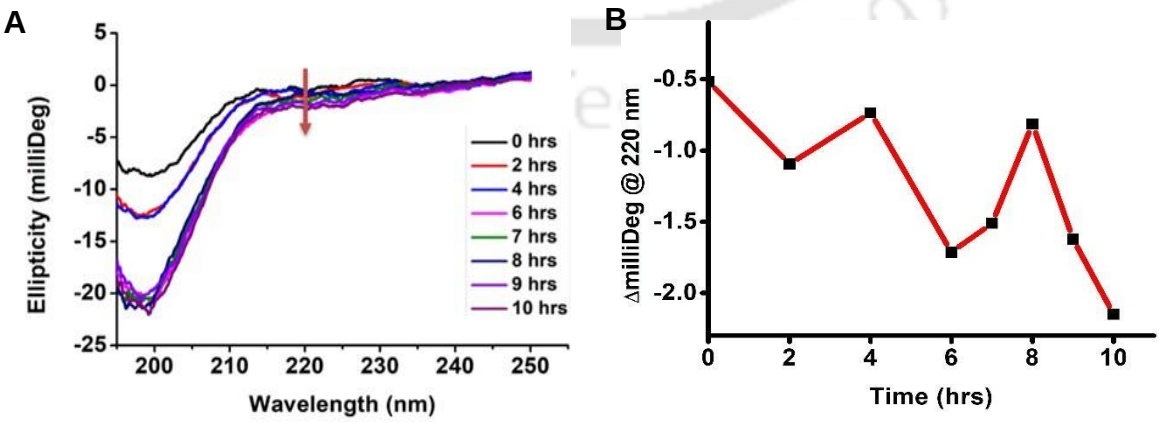

Figure 4.4: Panel A. CD spectra for alpha synuclein aggregation at different times in aggregation buffer (25 mM phosphate buffer, pH 7.4). Panel B shows the change in ellipticity

at 220 nm versus time.

In the case of CD spectra of alpha synuclein aggregates, an abrupt reduction in ellipticity at 190-200 nm between 6-9 hours was observed, suggesting that the protein had a lag phase in its aggregation mechanism till 6 hrs. A similar timeframe was used to study the alpha synuclein fibril formation using conventional fluorescence-based extrinsic probes: Thioflavin T (ThT), which is discussed in the next section.

4.2.3.3 Thioflavin T (ThT) fluorescence

When excited at 450 nm, Thioflavin-T (ThT), a well-known amyloid-specific dye, displays a significantly enhanced fluorescence emission at 480 nm when bound to fibrillar aggregates around 12 hours, in contrast to its relatively weak emission in the unbound, free state around 0 hours (Figure 4.5). This enhancement in fluorescence arises due to the restriction of ThT's rotational freedom upon binding to the repetitive β-sheet structures that are characteristic of amyloid fibrils. These observations have been previously reported and analyzed in studies such as Bhattacharya et al. (2014), where the binding-induced fluorescence changes were used as a marker for amyloid fibril formation.

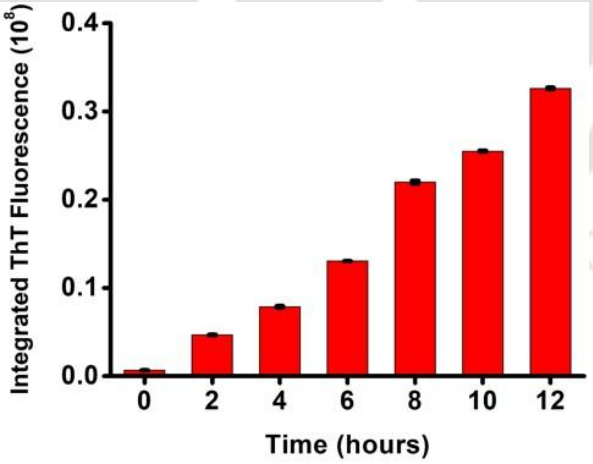

Figure 4.5: The figure shows the integrated ThT fluorescence for the alpha synuclein aggregates at different time points.

Optimization of the peptide-to-dye ratio is a critical yet challenging aspect when employing fluorescent probes such as Thioflavin T (ThT) for monitoring protein aggregation.

Experimental variability can arise from factors such as dye self-association, quenching effects, or insufficient binding sites per peptide molecule. These issues often complicate data interpretation and may result in inaccurate representation of aggregation kinetics.

To circumvent these limitations, a shift was made toward label-free strategies that do not require extrinsic probes and therefore eliminate dye-related artefacts. In the next section, the aggregation kinetics of alpha synuclein were directly monitored using Protein Charge Transfer Spectroscopy (ProCharTS). Both absorbance and luminescence measurements provided reliable, real-time insights into the structural transitions occurring during the aggregation process, offering a more robust and artifact-free alternative to dye-based assays.

4.2.3.4 ProCharTS Absorbance

ProCharTS absorbance of alpha synuclein aggregates was performed in conditions similar to that of CD. During early aggregation events, the protein molecules come close to each other. As a result, the charged residues in the flanking ends of the proteins are expected to come closer, and consequently enhanced ProCharTS is expected in aggregates as compared to monomers. Previously, the absorbance at 220 nm was used to track the early events of aggregation. The absorbance at 220 nm is characterized by the amide group in the peptide backbone. But here, we are interested in the longer wavelength region in the UV-Visible spectrum where ProCharTS primarily dominates the absorbance.

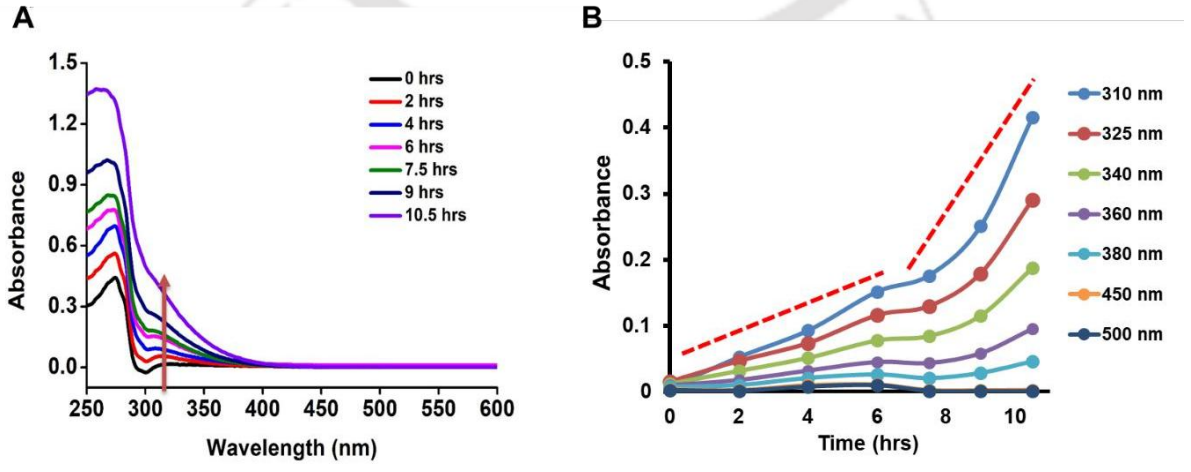

Figure 4.6: Panel A. ProCharTS spectra (250 - 600 nm) for alpha synuclein aggregation at different time points. Panel B. indicate the change with respect to 0 hours in ProCharTS

absorbance at various wavelengths versus time.

Figure 4.6A displays the ProCharTS absorbance spectra of alpha synuclein recorded in the range of 250–600 nm during the course of aggregation. As aggregation progressed, a marked and consistent increase in absorbance was observed across the entire spectral window. Apart from the characteristic tyrosine absorption peaks, no additional distinct features emerged; however, a pronounced absorbance tail extending toward longer wavelengths was evident, which is typical of ProCharTS absorption spectrum.

To quantify these spectral changes, absorbance intensities were monitored at selected wavelengths (310, 325, 340, 360, 380, 450, and 500 nm). As illustrated in Figure 4.6B, the increase in absorbance at each of these wavelengths exhibited a sigmoidal progression, reflecting the kinetics of alpha synuclein aggregation. While the overall trend remained consistent up to 500 nm, the sensitivity of detection diminished at longer wavelengths, likely due to reduced absorption in that region. All samples were centrifuged prior to measurement to remove insoluble material. This ensured that the observed increases in absorbance were attributable exclusively to ProCharTS absorption, effectively ruling out contributions from light scattering caused by larger fibrillar alpha synuclein aggregates.

4.2.3.5 ProCharTS luminescence

Building on the successful application of ProCharTS absorbance for monitoring the early stages of alpha synuclein aggregation, we next explored the use of ProCharTS luminescence to track similar events. Both approaches are based on the same fundamental principle of electron charge transfer followed by recombination of separated charges, but luminescence offers the added advantage of enhanced sensitivity to subtle structural changes.

Luminescence spectra of alpha synuclein were recorded at defined time intervals during aggregation, in parallel with other analytical measurements. Excitation was performed at three different wavelengths: 280 nm, 340 nm, and 355 nm and the resulting emission spectra were collected over the ranges 305–550 nm, 360–660 nm, and 375–600 nm, respectively.

As shown in Figure 4.7, aggregation was accompanied by a progressive increase in

luminescence intensity across all excitation wavelengths. While the trend was consistent, the overall emission yield decreased with longer excitation wavelengths, reflecting reduced excitation efficiency at higher wavelengths. A similar wavelength-dependent sensitivity was also observed in the ProCharTS absorbance experiments, supporting the complementary nature of the two approaches [Kumar et al., 2020].

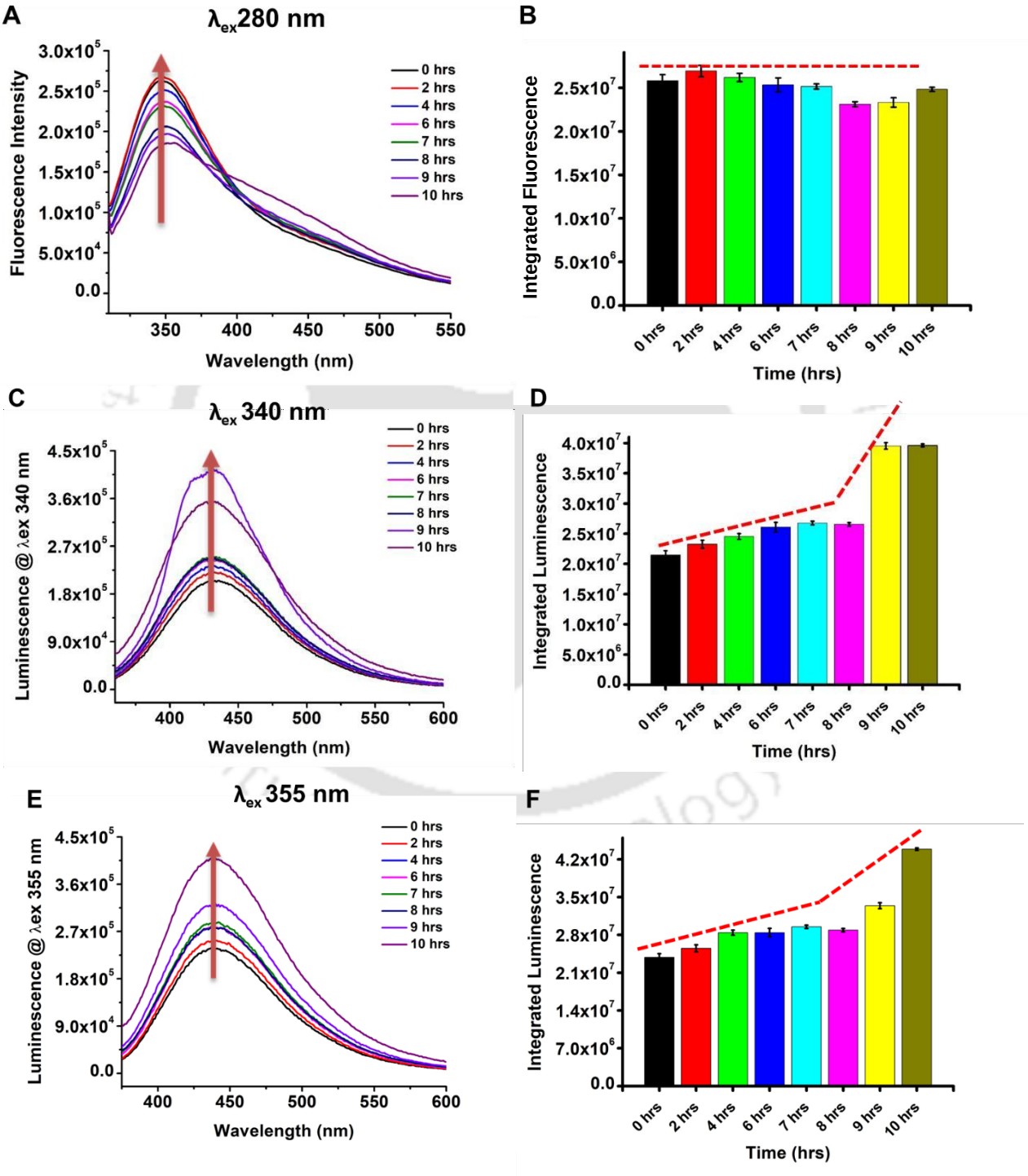

Figure 4.7: ProCharTS Luminescence Emission spectra for alpha synuclein aggregation at

different times in aggregation buffer (phosphate buffer, 25 mM pH 7.4) is shown for 3 different excitation wavelengths of 280 nm [panel A]; 340 nm [panel C]; 355 nm [panel E] and their emission collected in range of 305-550 nm; 360-600 nm; 375-600 nm respectively. Slit width (excitation/emission was kept at 2 nm/15 nm. Panel B, D, F shows the integrated ProCharTS luminescence versus aggregation time for all the above-mentioned excitation wavelengths.

In conclusion, ProCharTS luminescence proved to be a reliable method for tracking the kinetics of alpha synuclein aggregation. Its strong correlation with absorbance measurements and consistency across multiple excitation–emission windows highlight its potential as a versatile, label-free technique for studying the aggregation behavior of a wide range of proteins.

To broaden the scope of aggregation studies using ProCharTS, Human Lysozyme (HuL) was investigated under a distinct set of aggregation conditions. The results from this system are presented and discussed in the following section.

4.2.4 Detection of Human Lysozyme protein Aggregates using ProCharTS

4.2.4.1 CD spectroscopy for HuL aggregation studies

To validate the formation of aggregates, circular dichroism (CD) spectra were recorded for samples incubated under both acidic (pH 2.0) and alkaline (pH 12.2) conditions (Figure 4.8).

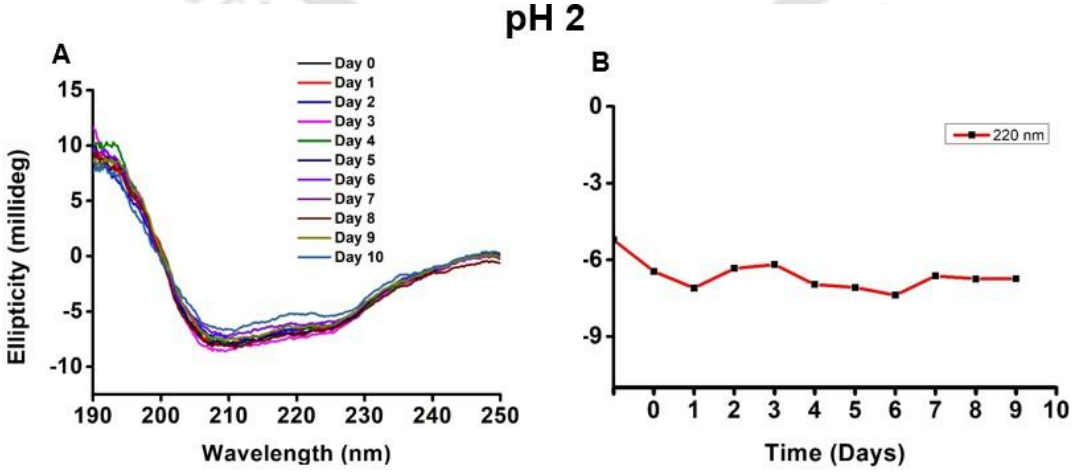

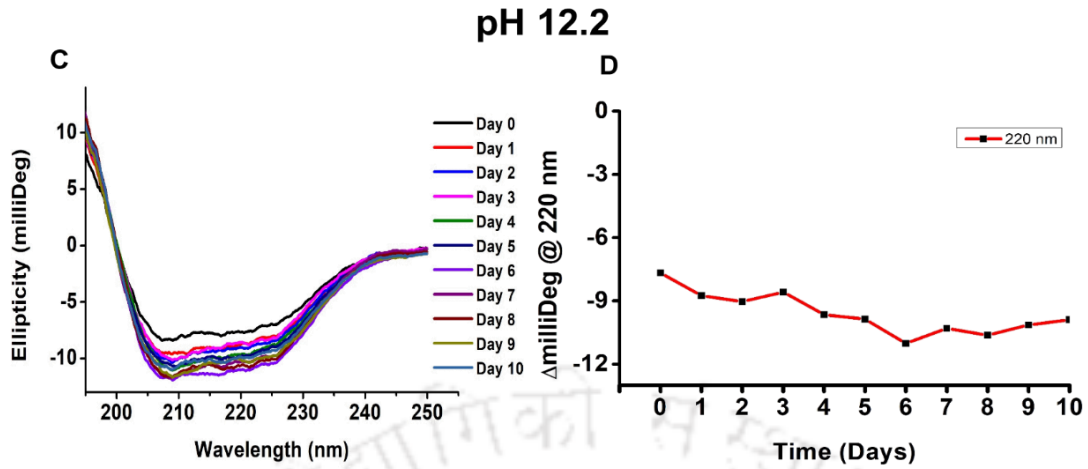

Figure 4.8: CD spectra for human lysozyme aggregation at pH 2 (panel A) and pH 12.2 (panel C) at different time points. Panel B and D shows the change in ellipticity at 220 nm versus time.

Human Lysozyme (HuL) in its native state predominantly adopts an α-helical secondary structure. During aggregation, however, it gradually undergoes a structural transition toward β-sheet formation. Since HuL aggregation is inherently a slow process, the development of a complete β-sheet-rich conformation requires extended incubation under both acidic and alkaline conditions. Once mature aggregates are formed, they become insoluble and tend to precipitate, limiting their detection by spectroscopic methods. As a result, the CD spectra primarily reflected the early stages of aggregation, capturing structural features associated with soluble oligomeric intermediates rather than fully developed fibrillar assemblies.

To further probe aggregation using an extrinsic chromophore, Thioflavin T (ThT) fluorescence assays were performed on samples incubated under both acidic (pH 2.0) and alkaline (pH 12.2) conditions.

4.2.4.2 ThT Assay for HuL aggregation studies

Thioflavin T (ThT) assays were carried out for HuL samples incubated at both pH 2 (Figure 4.9) and pH 12.2 (Figure 4.10). At pH 2, the fluorescence intensity exhibited a steady increase till Day 4 during the initial phase of incubation, reflecting progressive aggregation. However, after Day 4, the signal began to plateau, indicating that the aggregation process had reached near saturation. Between Day 4 and Day 10, only a modest further increase in

integrated intensity was observed. This pattern suggests that oligomer formation at pH 2 is initially limited, but as incubation continues, a greater number of oligomeric species accumulate until the aggregation reaction reaches saturation.

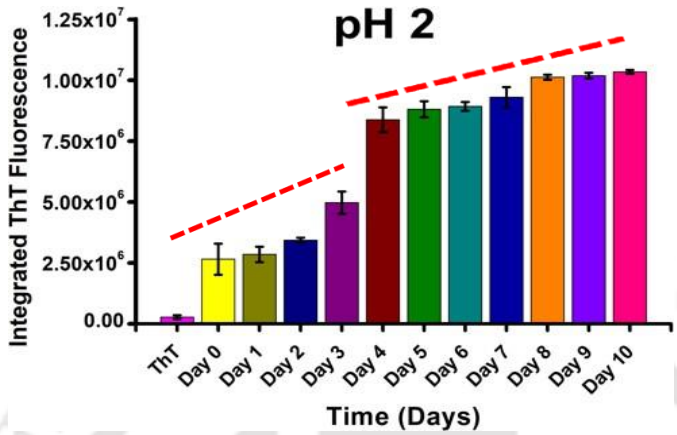

Figure 4.9: Integrated ThT fluorescence for human lysozyme aggregation at pH 2 at different time points.

In contrast, at pH 12.2 (Figure 4.10), aggregation proceeded much more slowly, with only a gradual increase in ThT signal that reached saturation by around Day 7. These results demonstrate that aggregation is faster and more pronounced at acidic pH, whereas at alkaline pH the process occurs more slowly and reaches saturation later.

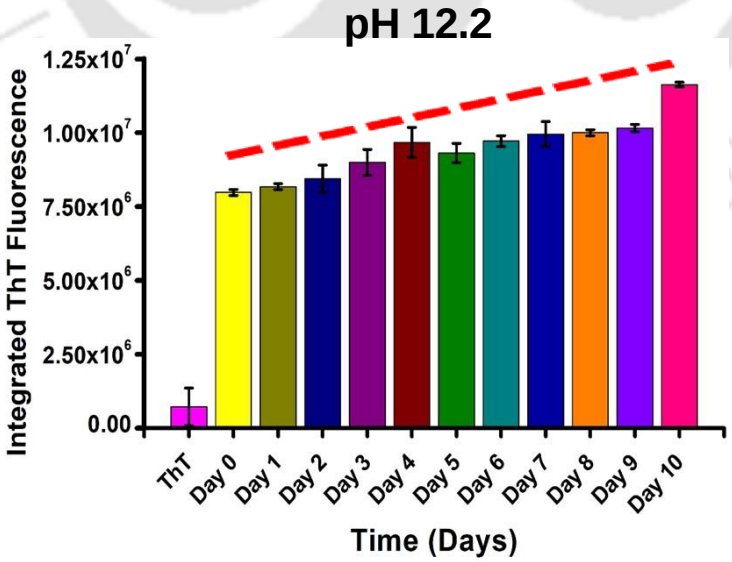

Figure 4.10: Integrated ThT fluorescence for human lysozyme aggregation at pH 12.2 at different time points.

Therefore, the ThT assay did not provide a clear or definitive representation of HuL aggregation under the tested conditions. This limitation further highlights the importance of employing intrinsic, label-free approaches such as ProCharTS, which offer a more reliable means of monitoring HuL aggregation.

4.2.4.3 ProCharTS of HuL aggregates formed at acidic pH (2)

At acidic pH, Human Lysozyme (HuL) aggregates exhibit distinctive structural characteristics (Figure 4.11 A). In particular, at pH 2.0, HuL shows a strong propensity to form fibrillar assemblies, as reflected by the increase in Thioflavin T (ThT) fluorescence intensity, a well-established marker of amyloid fibril formation. This observation is consistent with previous reports highlighting that low pH conditions promote partial unfolding of HuL, thereby facilitating β-sheet-rich fibril formation.

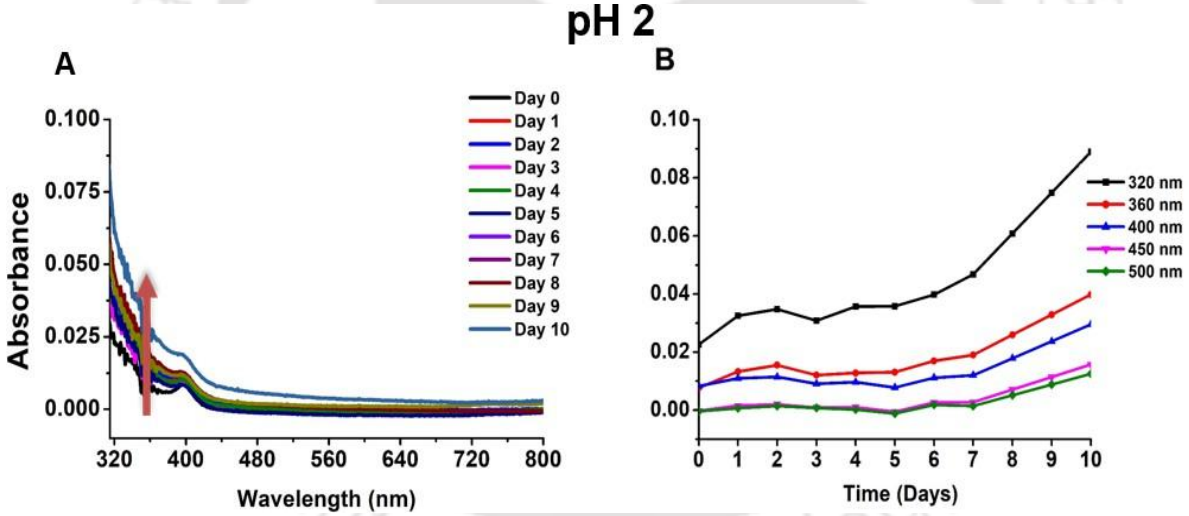

Figure 4.11: A. ProCharTS spectra (315-800 nm) for Human Lysozyme aggregation at different time points at pH 2. Subfigure B indicate the change with respect to Day 0 in ProCharTS absorbance at various wavelengths versus time.

At pH 2, Asp and Glu are protonated and uncharged and thus, diminishes ProCharTS. Only His, Arg and Lys are charged and can contribute to the ProCharTS. Time-resolved monitoring of the aggregation process using both Protein Charge Transfer Spectra (ProCharTS) (Figure 4.11 B) and ThT fluorescence (Figure 4.9) revealed a minor increase in signal intensity during the early phase of incubation. However, after Day 4, the

aggregation process appeared to accelerate, as indicated by ProCharTS signals from Day 5 through Day 10. Thus, ProCharTS absorption is the tracking the aggregation in a different way.

The fibrillar and compact morphology of HuL aggregates formed at pH 2 likely contributes to the observed spectroscopic behavior. Such structures provide extensive intermolecular contacts and increase the probability of charged residues being positioned in close proximity, thereby enhancing both ThT binding and ProCharTS signal intensity.

4.2.4.4 ProCharTS of HuL aggregates formed at alkaline pH (12.2)

At pH 12.2, Human Lysozyme (HuL) aggregates displayed a gradual increase in Protein Charge Transfer Spectra (ProCharTS) absorbance intensity (Figure 4.12 A). This slow enhancement is consistent with the progressive formation of larger aggregates at later stages of incubation, where extensive intermolecular interactions between charged side chains become more prominent. In contrast, such interactions are limited during the early stages of aggregation, resulting in relatively weaker ProCharTS signals.

When ProCharTS absorbance was plotted as a function of time, a steady, though slow, increase was observed across successive days of incubation (Figure 4.12 B). Notably, the absorbance signal at longer wavelengths gradually diminished with time, a characteristic feature of ProCharTS absorption behavior.

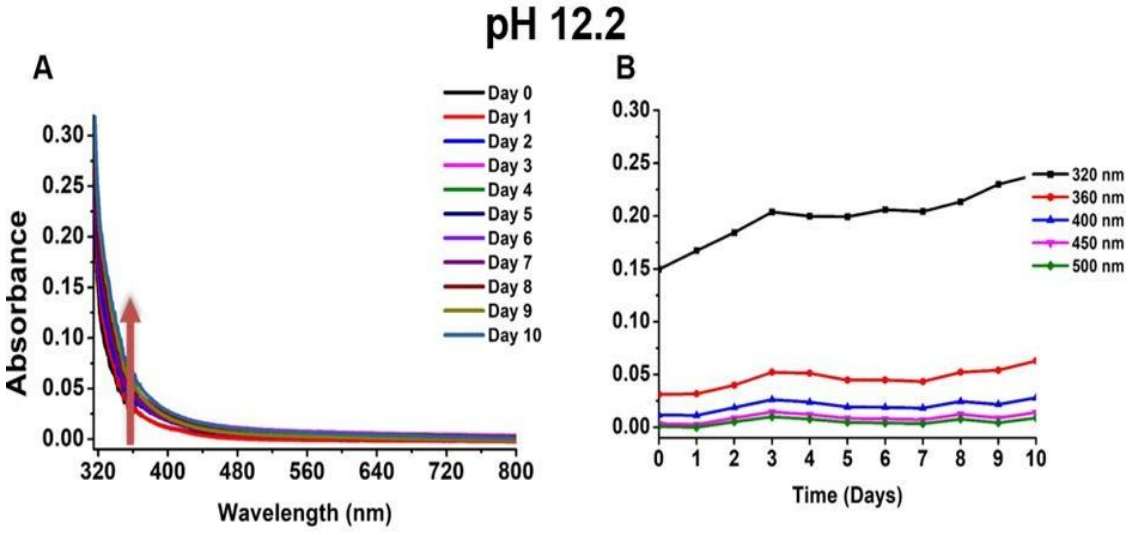

Figure 4.12: A. ProCharTS spectra (315-800 nm) for Human Lysozyme aggregation at

different time points at pH 12.2. Subfigure B indicate the change with respect to day 0 in ProCharTS absorbance at various wavelengths versus time.

The possibility of partial proteolysis at strongly alkaline pH cannot be ruled out and may contribute to the observed spectral changes. Despite the overall slow kinetics, the data clearly indicate a continuous, time-dependent progression of HuL aggregation under alkaline conditions. Moreover, at pH 12.2, Arg and many His, Lys are not protonated, thus reducing charged residue population and diminishing ProCharTS. Only Asp and Glu contribute to the ProCharTS at pH 12.2.

The parallel trends observed between ProCharTS and ThT fluorescence measurements underscore the value of ProCharTS as a complementary tool for monitoring protein aggregation. While ThT fluorescence is primarily responsive to the presence of mature, β-sheet rich fibrillar structures, ProCharTS has the potential to provide additional layers of information. In particular, it may be capable of detecting early-stage oligomeric intermediates or subtle conformational rearrangements that occur prior to the onset of fibril formation, thereby offering a broader perspective on the aggregation pathway.

4.2.4.5 Tryptophan fluorescence for HuL aggregation

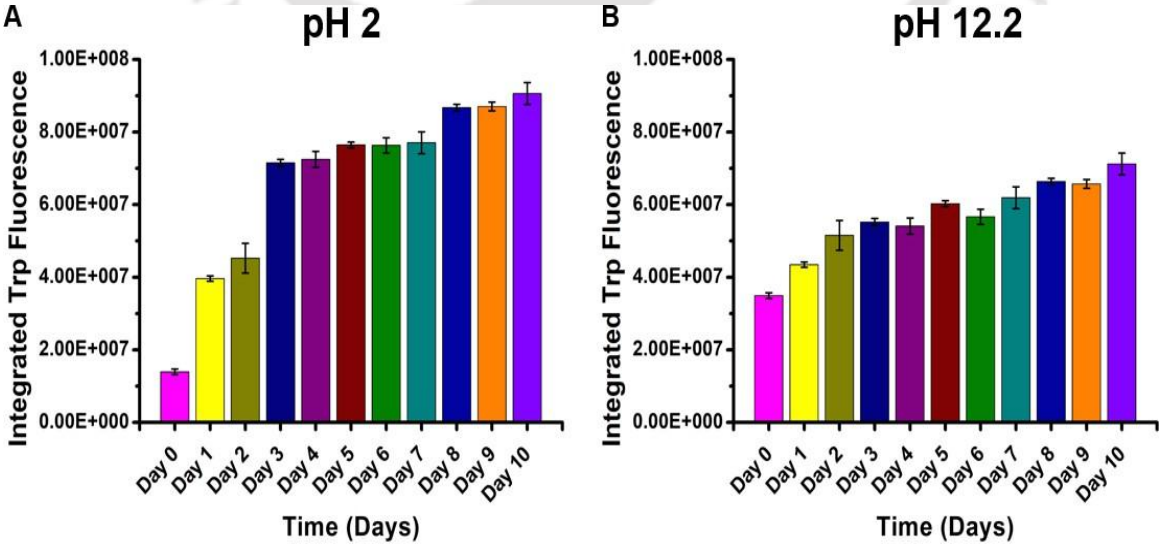

Figure 4.13: Integrated Tryptophan fluorescence for human lysozyme aggregation at pH 2 (A)and pH 12.2 (B) at different time points.

Tryptophan fluorescence spectroscopy was employed to monitor structural changes in HuL during the course of aggregation. The measurements revealed a progressive, time-dependent increase in fluorescence intensity (Figure 4.13), indicating alterations in the local environment of tryptophan residues as the protein transitioned from its native state toward aggregated forms. This increase likely reflects reduced solvent exposure or changes in quenching associated with the formation of oligomers and higher-order aggregates. At pH 2, less quenching occurs due to the protonated COOH group present. On the other hand, more quenching occurs at pH 12.2 due to the presence of COO^-. Such fluorescence behavior is consistent with the gradual reorganization of protein tertiary structure and provides complementary evidence supporting the aggregation process.

4.2.4.6 ProCharTS luminescence of HuL Aggregation

We investigated the intrinsic luminescence properties of human lysozyme (HuL) aggregates formed under both acidic and alkaline conditions. As shown in Figures 4.14 and 4.15, extending the incubation period up to 10 days at pH 2.0 and pH 12.2 resulted in a gradual and progressive increase in luminescence intensity for both environments. This enhancement in luminescence is most likely due to the development of charge-transfer states within the aggregating protein structures. Such states arise as intermolecular interactions among residues become more extensive during aggregation, suggesting a direct correlation between aggregate maturation and the emergence of intrinsic luminescent properties.

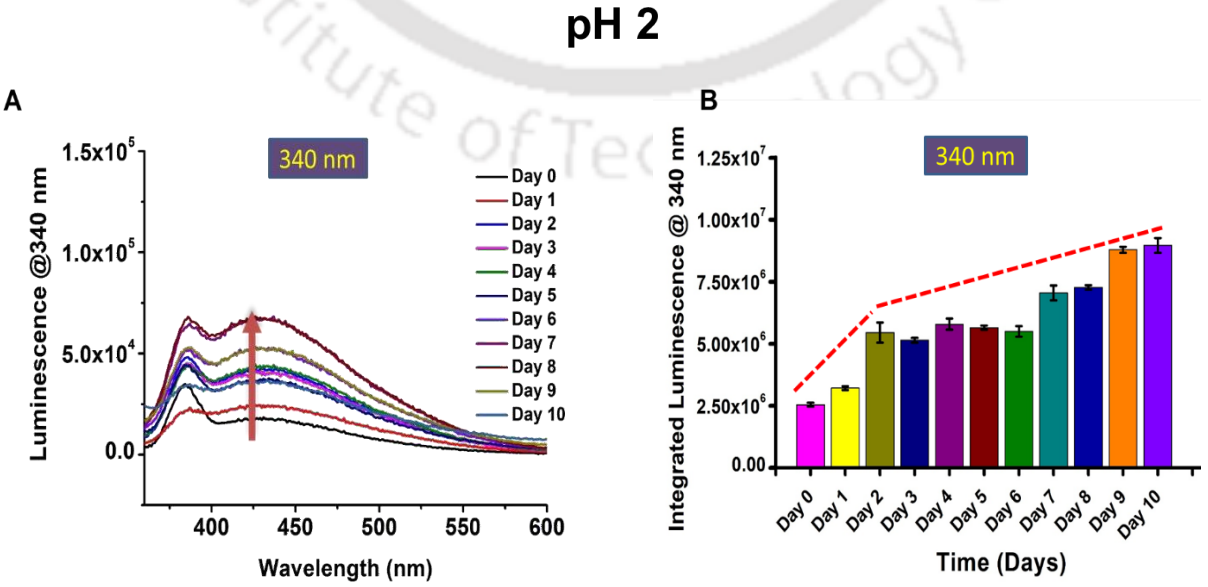

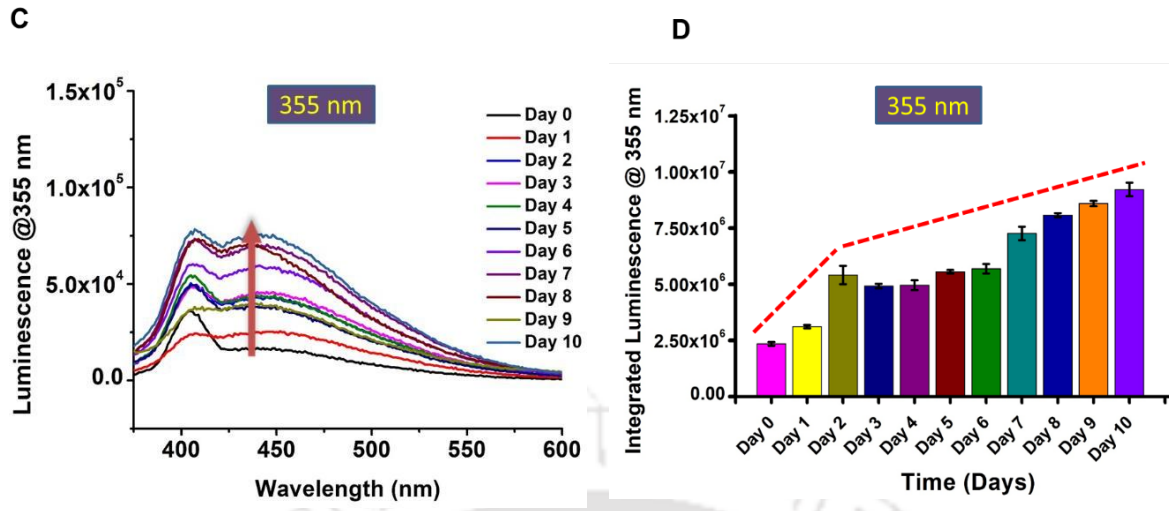

Figure 4.14: ProCharTS Luminescence Emission spectra for HuL at different times is shown for pH 2 different excitation wavelengths of 340 nm [panel A]; 355 nm [panel B] and their emission collected in range of 360-600 nm; 375-600 nm respectively. Slit width (excitation/emission was kept at 2 nm/15 nm). Panel B, D shows the integrated ProCharTS luminescence versus aggregation time for all the above-mentioned excitation wavelengths.

Interestingly, the rate and extent of luminescence enhancement differed between the two pH conditions. At pH 2.0, where fibrillar aggregates dominate, luminescence increased more rapidly, suggesting that compact, highly ordered structures favor stronger charge-transfer interactions (Figure 4.14). In contrast, at pH 12.2, the increase was slower and more gradual, consistent with the formation of less compact aggregates under alkaline conditions (Figure 4.15).

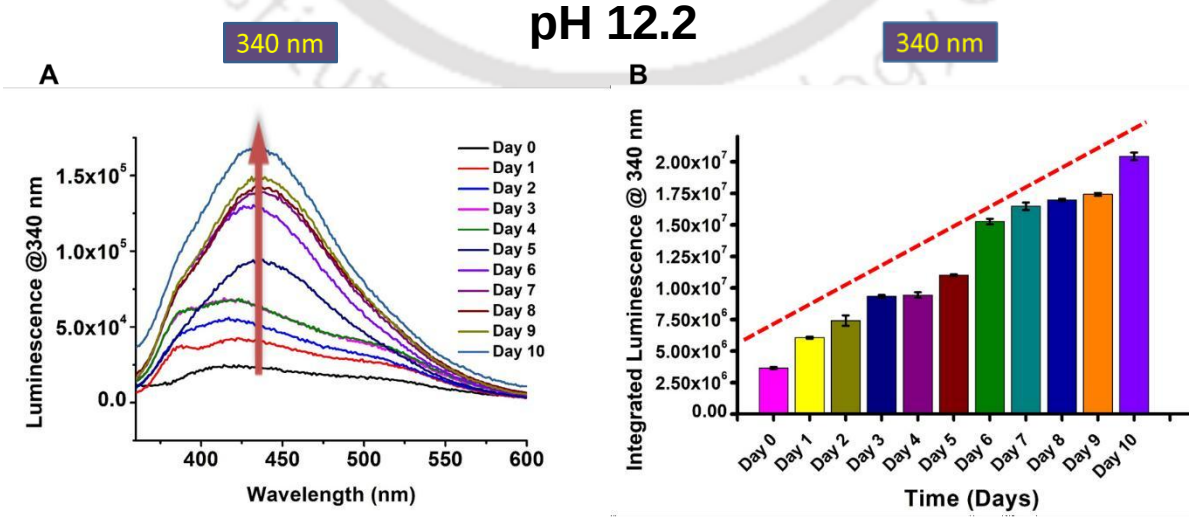

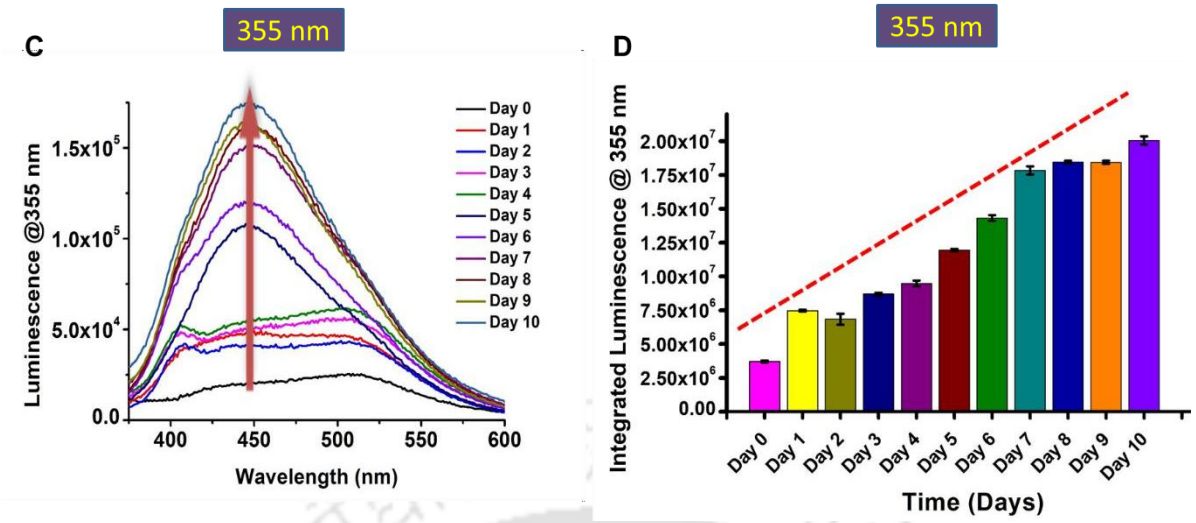

Figure 4.15: ProCharTS Luminescence Emission spectra for HuL at different times is shown for pH 12.2 different excitation wavelengths of 340 nm [panel A]; 355 nm [panel B] and their emission collected in range of 360-600 nm; 375-600 nm respectively. Slit width (excitation/emission was kept at 2 nm/15 nm). Panel B, D shows the integrated ProCharTS luminescence versus aggregation time for all the above-mentioned excitation wavelengths.

Integrated luminescence values are higher at pH 12.2 in comparison to pH 2.These differences highlight the sensitivity of intrinsic luminescence to the structural nature of aggregates, underscoring its potential as a complementary probe for distinguishing aggregation pathways.

Consistent with the ProCharTS absorption data, the intrinsic luminescence arising from charge-transfer states in HuL aggregates appears particularly sensitive to the detection of oligomeric species, while also maintaining a strong response to fibrillar aggregates. This dual sensitivity is noteworthy, as it suggests that luminescence can complement conventional fluorescence-based assays in monitoring different stages of the aggregation pathway. For example, ThT fluorescence at pH 2 shows a progressive increase over time, reflecting the accumulation of fibrillar species. Interestingly, this trend is closely paralleled by the gradual rise in intrinsic luminescence intensity (Figure 4.14), indicating that luminescence not only tracks fibril formation but also responds to earlier structural transitions. Moreover, the time-dependent increase in tryptophan fluorescence further supports this view, as it highlights changes in the local environment of aromatic residues during oligomerization and fibril growth. Taken together, these converging results emphasize that ProCharTS luminescence provides complementary and possibly earlier insights into aggregation events compared to

extrinsic probes like ThT, thereby broadening the analytical toolkit for studying protein misfolding and self-assembly.

The excitation-dependent shift in emission maxima, deviating from Kasha's rule, is a well-documented characteristic of ProCharTS luminescence and is commonly observed in monomeric proteins. In the case of HuL aggregation, a clear red-shift in emission maxima (λ_{max}) was noted with increasing excitation wavelength: ~415 nm at λ_{ex} 295 nm, ~425 nm at λ_{ex} 340 nm, and ~440 nm at λ_{ex} 370 nm. Interestingly, these emission maxima remained consistent regardless of whether the protein was in its monomeric or aggregated state, in contrast to conventional extrinsic chromophores such as ThT, which often display state-dependent spectral changes. The invariance of λ_{max} across aggregation states suggests that, although the chromophores within the system are heterogeneous, they share intrinsic similarities and exhibit uniform photophysical behavior under different structural conditions.

Intrinsic luminescence has recently been reported in amyloids [Jesus et al., 2021; Panseiri et al., 2019; Monti et al., 2021; Ziaunys et al., 2021], concentrated amino acids, monomeric proteins, and oligomeric protein/peptide systems [Chen et al., 2018]. Several studies have also demonstrated fluorescence waveguiding in amyloids through multiple absorption–reabsorption photon recycling events [Apter et al., 2020]. To explain such observations, mechanisms such as Clustering Triggered Emission (CTE) and Aggregation-Induced Emission (AIE) have been proposed, which attribute luminescence primarily to the formation of molecular aggregates or clusters as prerequisites for emissive behavior.

In contrast, we propose that the luminescence observed in our study originates from Protein Charge Transfer Spectra (ProCharTS) luminescence, which arises due to proximal charge distributions within the protein structure. This mechanism is independent of whether the protein exists in a monomeric, oligomeric, or aggregated state. Aggregation, however, can enhance the effect by bringing charged residues into closer proximity, thereby increasing the likelihood of charge recombination between photo-excited electrons and nearby holes in the peptide backbone. The progressive increase in luminescence intensity observed during aggregation can thus be interpreted as a reflection of enhanced intermolecular charge transfer interactions.

Taken together, these findings strengthen the hypothesis that ProCharTS luminescence is a robust and versatile technique. Unlike extrinsic dye-based methods, it provides an intrinsic, label-free means to monitor aggregation kinetics in proteins and peptides, making it a valuable complementary tool for studying diverse aggregation pathways.

4.2.5 Comparison of the techniques

In this chapter, the aggregation behaviour of alpha synuclein and human lysozyme was systematically monitored using a range of complementary techniques. To gain deeper insights, we next compared the performance of these techniques in detecting the early stages of alpha synuclein and HuL aggregation, with a particular focus on evaluating their relative sensitivities.

For this comparison, ProCharTS absorbance and luminescence were assessed alongside conventional approaches such as circular dichroism (CD), and ThT fluorescence. The extent of aggregation was quantified by calculating the percentage change for each method using the expression**: [(Aggregated − Monomeric) / Monomeric] × 100%.**

Here, the signal values at the beginning of the experiment (0 hour/Day) were taken as the baseline monomeric reference, while the values at the final recorded time point were used as the aggregated state. For CD analysis, ellipticity values at two characteristic wavelengths, 220 nm and 208 nm, were considered. For ProCharTS, absorption intensity values at 340 nm and integrated luminescence values at 340 nm 355 nm and 280/295 nm, were utilized. In the case of ThT, the integrated fluorescence areas under the emission curves for monomeric and aggregated samples were analysed.

A

Alpha Synuclein

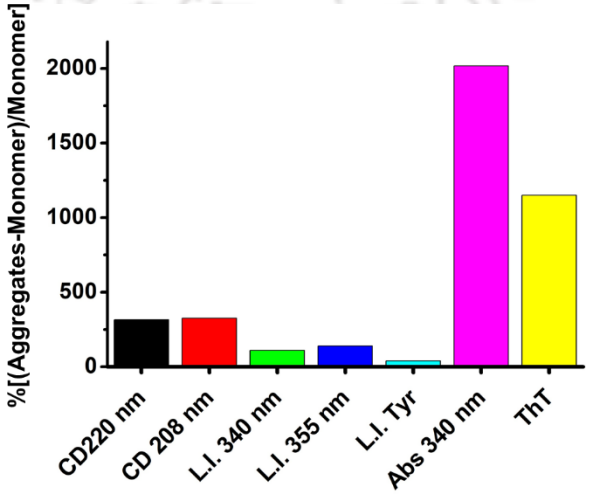

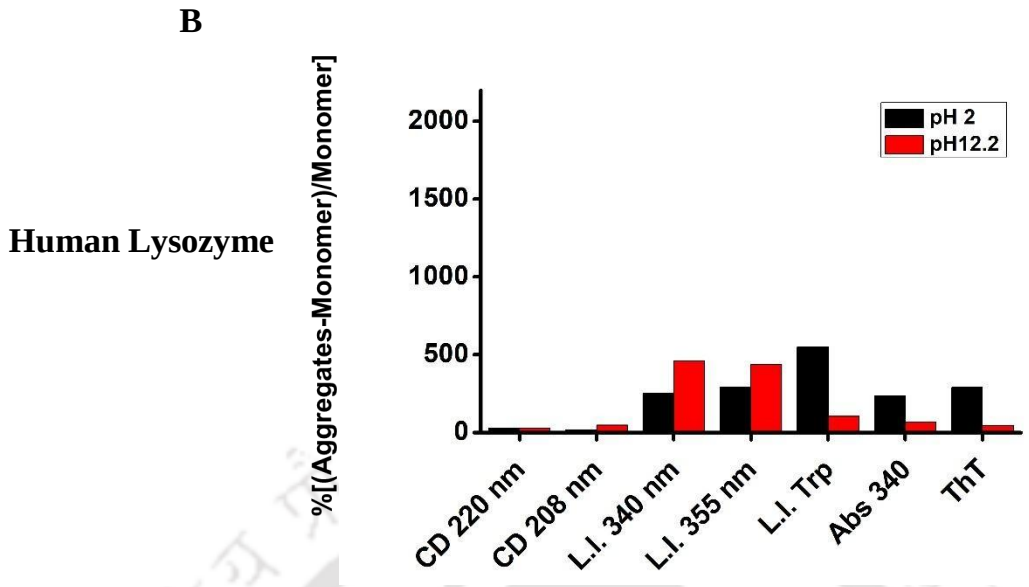

Figure 4.16: Percentage change in the aggregated state as compared to monomeric states of A. alpha synuclein and B. Human Lysozyme in the various techniques compared.

Taken together, our findings establish ProCharTS absorbance as a highly sensitive technique for monitoring protein aggregation, with performance comparable to circular dichroism (CD) spectroscopy and superior to conventional probes such as Thioflavin T (ThT). Importantly, ProCharTS not only detects early aggregation events but also provides enhanced resolution of subtle structural transitions that may be overlooked by traditional methods. These advantages position ProCharTS as a promising and potentially transformative tool in the study of amyloid aggregation kinetics. Looking forward, expanding its application across diverse amyloid systems and deepening the mechanistic understanding of its signal origins will be crucial. Such efforts could solidify ProCharTS as a versatile platform for both fundamental research and translational applications, including the screening of therapeutic interventions targeting protein aggregation.

4.3 Conclusion

- **ProCharTS enables label-free detection of protein aggregates.**

Unlike conventional aggregation assays that require external dyes or fluorophores (e.g., Thioflavin T, ANS), ProCharTS directly exploits the intrinsic photophysical properties of proteins. This label-free approach eliminates potential artifacts arising from dye binding, avoids perturbation of protein structure, and allows continuous monitoring of aggregation in its native state. Such an advantage makes ProCharTS especially useful for studying aggregation-prone systems where the presence of exogenous probes may interfere with the natural kinetics of the process.

- **ProCharTS exhibits higher sensitivity in the shorter wavelength range, making it particularly effective for early-stage aggregate identification.**

ProCharTS detects subtle changes in charge transfer interactions between amino acid side chains, which are perturbed even during the earliest stages of aggregation. These changes manifest most clearly at shorter excitation/emission wavelengths, providing enhanced sensitivity for detecting oligomeric intermediates that often remain invisible to conventional spectroscopic probes. Thus, ProCharTS serves as an early-warning system for protein misfolding, allowing researchers to capture transient intermediates that precede mature fibril formation.

- **Compared to Thioflavin T (ThT) and CD, ProCharTS shows enhanced capability in detecting early protein aggregation events.**

ThT fluorescence is widely used as a gold standard for amyloid detection but primarily responds to β-sheet–rich fibrillar structures, making it less effective in identifying prefibrillar species. Circular dichroism (CD), on the other hand, is powerful for secondary-structure analysis but often lacks sensitivity when monitoring minor structural perturbations. ProCharTS bridges these gaps by providing strong signals even when oligomeric species or partially folded intermediates form, thereby offering superior resolution during the lag phase of aggregation. This positions ProCharTS as a complementary, and in some cases superior, technique for kinetic studies of amyloidogenesis.

CHAPTER 5

MONITORING UNFOLDING OF ERK2 AND HUMAN LYSOZYME PROTEINS USING PROCHARTS

5.1 Introduction

Charge interactions plays a pivotal role in the unfolding of proteins, influencing their structural stability and folding pathways. Proteins are composed of amino acids, some of which carry charged side chains. These charged residues can form electrostatic interactions, such as salt bridges, which stabilize the protein's native conformation. During unfolding, these electrostatic interactions are disrupted, leading to conformational changes.

Research by Nandi et al. (2020) investigated the effects of substituting charged residues involved in salt bridges within ubiquitin with hydrophobic residues. They found that such substitutions can significantly influence the protein's folding dynamics and stability. Specifically, the removal of certain salt bridges led to a more stable transition state and accelerated folding rates, underscoring the pivotal role of electrostatic interactions in protein folding pathways. These findings highlight the nuanced role of electrostatic interactions in protein folding. While salt bridges can contribute to the stability of the native state, their presence may also raise the energy barrier of the transition state, potentially slowing down the folding process. By strategically modifying these interactions, it is possible to modulate protein folding kinetics and stability, offering valuable insights for protein engineering and design.

Recently, novel spectroscopic techniques, such as Protein Charge Transfer Spectra (ProCharTS), have been employed to monitor changes in the proximity of charged groups during protein unfolding. These studies reveal that disruptions in charged amino acid sidechain contacts occur at lower denaturant concentrations compared to the loss of secondary structures, underscoring the sensitivity of electrostatic interactions to unfolding conditions [Priyadarshi et al., 2023]

In summary, electrostatic interactions are integral to the protein unfolding process. They not only stabilize the native structure but also influence the pathways and intermediates during unfolding. Understanding these interactions provides valuable insights into protein folding mechanisms and can inform strategies for protein engineering and therapeutic interventions.

To probe this interplay more thoroughly, we selected two structurally distinct model proteins, human lysozyme, which contains approximately 20 % charged residues, and ERK2

(extracellular-signal-regulated kinase 2), exhibiting around 27 % charged amino acids.to examine how their unfolding influences ProCharTS signals. By subjecting these proteins to controlled denaturation, we induced structural unfolding to deliberately disrupt the spatial proximity of charged side chains. We then tracked resulting changes in the ProCharTS signals, specifically in their UV–Visible absorption and luminescence spectra, to determine how altered electrostatic environments influence charge-transfer behaviour. This approach enables us to critically evaluate ProCharTS sensitivity to the loss of charge–charge interactions as the proteins unfold, adding a layer of quantitative insight into its efficacy as an intrinsic probe of electrostatic configuration changes.

5.2 Results and Discussion

5.2.1 Expression and Purification of ERK2 protein

To experimentally investigate the unfolding behavior of ERK2 protein using Protein Charge Transfer Spectroscopy (ProCharTS), the ERK2 protein was first expressed and purified. For purification, Ni-NTA affinity chromatography was employed, taking advantage of the His-tag engineered at the N-terminus of the protein. This method enabled selective binding of the His-tagged ERK2 to the nickel-charged resin, allowing for efficient separation from other cellular proteins. The purified ERK2 was subsequently used for ProCharTS measurements to monitor conformational changes associated with protein unfolding.

The purified ERK2 protein was eluted using 350 mM imidazole in the elution buffer, which effectively displaced the His-tagged protein from the Ni-NTA resin. The purity of the eluted protein was assessed by reducing SDS-PAGE using a 15% acrylamide gel. As shown in Figure 5.1, a distinct single band corresponding to ERK2 was observed, confirming successful purification. The purified ERK2 migrated with an apparent molecular weight of approximately 42 kDa, consistent with its expected size under denaturing conditions

.

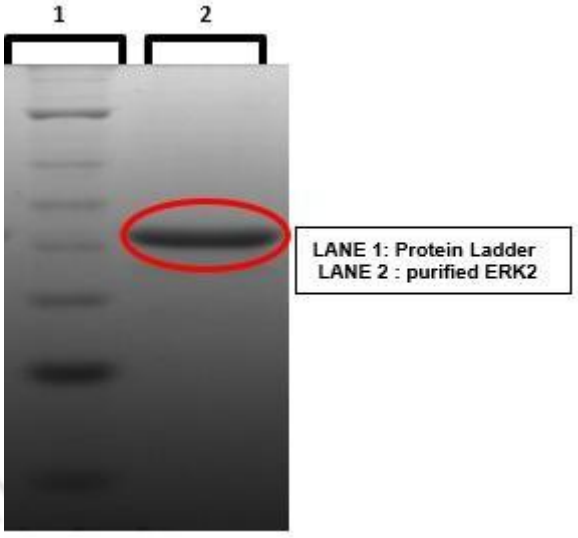

Figure 5.1: 15% reducing SDS-PAGE showing a single distinct band corresponding to purified ERK2 protein with an apparent molecular weight of approximately 42 kDa.

5.2.2 Mass Spectrometry Analysis

The molecular mass of the purified ERK2 protein was determined using Matrix-Assisted Laser Desorption/Ionization (MALDI) mass spectrometry. The analysis confirmed the presence of a single peak corresponding to the expected mass of monomeric ERK2, indicating successful purification and the absence of aggregation or degradation products.

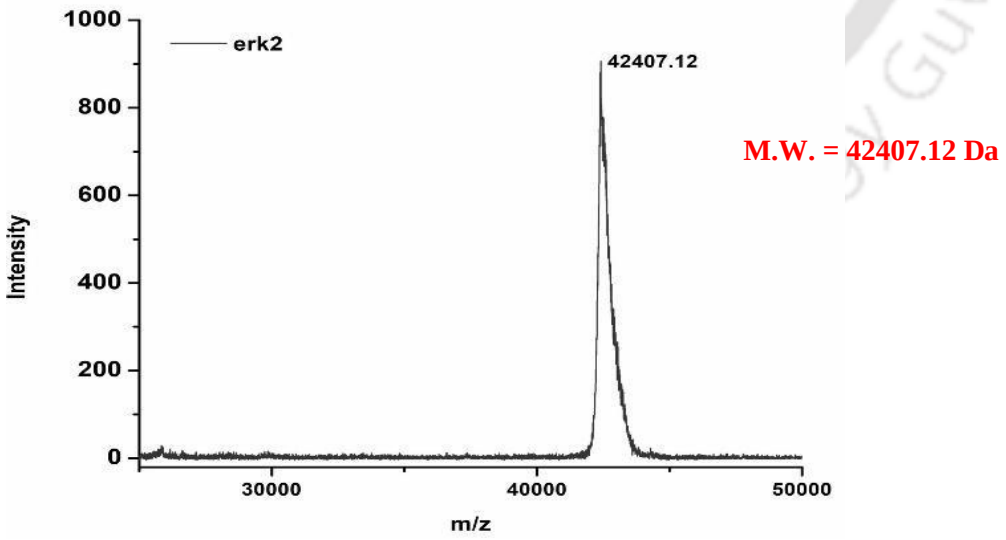

Figure 5.2: MALDI mass spectrum of purified ERK2 protein, showing a single peak corresponding to its theoretical molecular weight of approximately 42.6 kDa, confirming the monomeric and purified state of the protein.

The molecular mass obtained from the MALDI spectrum was approximately 42 kDa, which closely matches the estimated theoretical mass of ERK2 (including the His tag), thereby confirming the identity and integrity of the purified protein.

5.2.3 Detection of Protein Unfolding using ProCharTS Absorbance

Alterations in the surrounding solvent environment such as shifts in pH, temperature, or ionic strength can disturb the delicate equilibrium of intramolecular forces within a protein, ultimately triggering its unfolding. Chemical agents like guanidine hydrochloride (GdnHCl) disrupt key non-covalent interactions, including hydrogen bonds and hydrophobic contacts, thereby promoting the unfolded state. These denaturants act by stabilizing the unfolded conformation, making chemical denaturation one of the most reliable and straightforward methods for studying protein unfolding [Priyadarshi et al., 2023]. In the present study, ERK2 and Human Lysozyme (HuL) were subjected to chemical denaturation using guanidine hydrochloride (GdnHCl) across a concentration range of 0–6 M, in order to induce progressive protein unfolding. The resulting structural changes were then analyzed to assess their influence on the Protein Charge Transfer Spectra (ProCharTS). To validate that HuL and ERK2 underwent unfolding under these denaturing conditions, complementary spectroscopic techniques like far UV CD; Tryptophan fluorescence; ANS fluorescence were also employed, providing independent confirmation of the conformational transitions.

5.2.3.1 Monitoring the unfolding of HuL using ProCharTS Absorbance

In this study, the denaturation and unfolding mechanism of lysozyme has been elucidated through the application of the disulfide scrambling technique. Under strongly denaturing conditions induced by guanidinium hydrochloride (GdnHCl), lysozyme undergoes structural disruption in which its four native disulfide bonds are no longer maintained in their original configuration [Chang et al., 2002]. Instead, these covalent linkages are reshuffled, resulting in the formation of a heterogeneous population of fully oxidized scrambled isomers. This scrambling process provides valuable insight into the interplay between protein folding, stability, and the maintenance of disulfide connectivity under chemical stress.

Firstly, a slight red shift in the absorption maximum of Hul protein was observed (Figure

5.3), indicating increased exposure of these residues to the aqueous environment upon unfolding. This shift suggests that the aromatic side chains, which are typically buried within the hydrophobic core of the native protein, become more solvent-accessible as the protein unfolds [Duy et al., 2006].

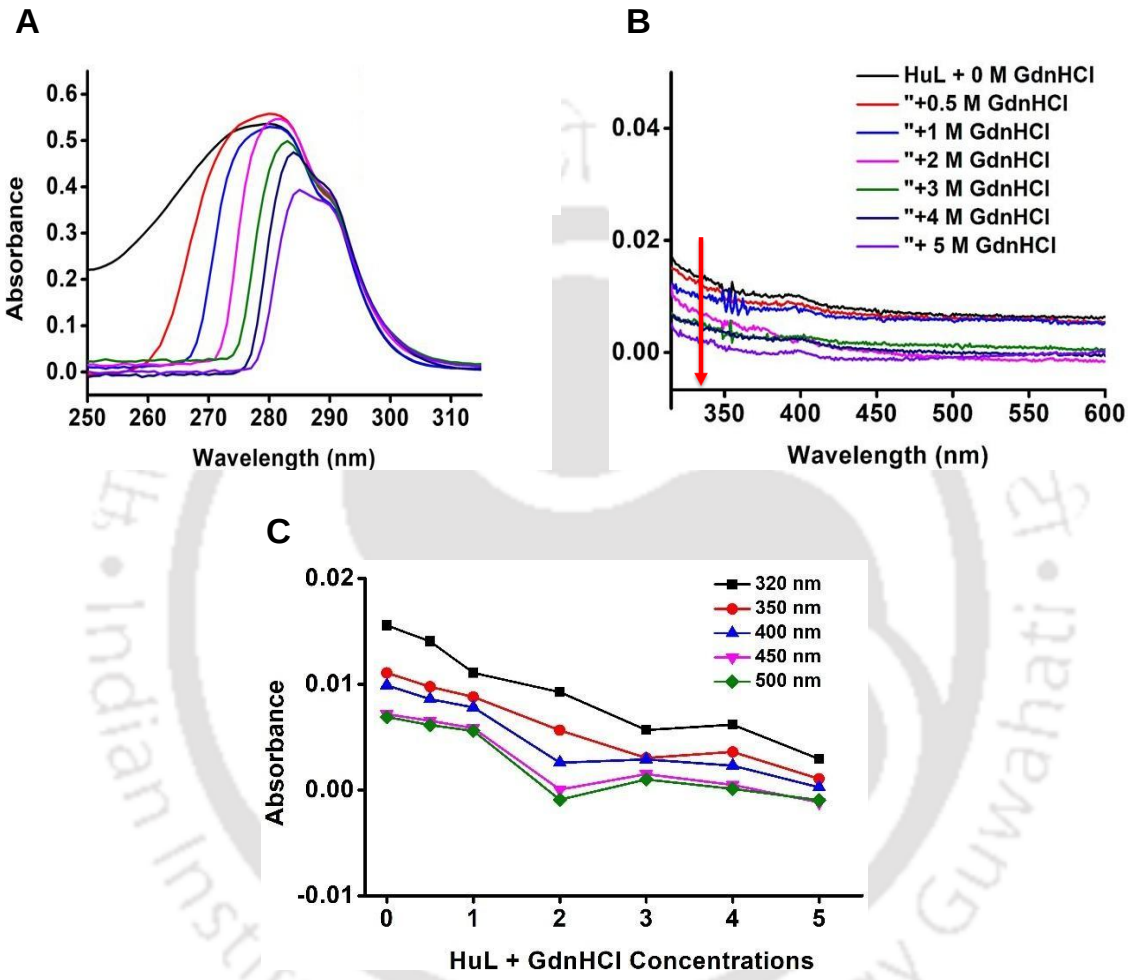

Figure 5.3: Absorbance spectra A. 250 - 315 nm and B. 315 – 600 nm for 20 µM Human Lysozyme unfolding at different GdnHCL concentrations in 20 mM phosphate buffer at pH 7.5. Subfigure C indicate the change with respect to 0 M in ProCharTS absorbance at various wavelengths versus time.

A marked reduction in the ProCharTS signal of HuL was observed at different guanidinium hydrochloride (GdnHCl) concentrations, with the absorbance reaching baseline levels at 5.5 M GdnHCl. This decline in ProCharTS was attributed to the disruption of interactions between charged amino acid side chains, resulting from protein unfolding. This disruption diminishes charge transfer across different charged groups.

5.2.3.2 Monitoring the unfolding of ERK2 using ProCharTS Absorbance

Chemical denaturation of ERK2 with guanidinium hydrochloride (GdnHCl) was carried out, and protein unfolding was tracked by monitoring ERK2 ProCharTS absorbance across multiple wavelengths (Figure 5.4). For ERK2, unfolding led to a pronounced decrease in ProCharTS, with $Abs_{340\ nm}$ dropping from 0.058 to 0.005 in the presence of 5 M GdnHCl (Figure 5.4). Similar decreases were recorded at other monitored wavelengths during unfolding. Notably, a reduction in ERK2 ProCharTS was evident even at 3 M GdnHCl, with absorbance reaching baseline at 5 M GdnHCl. This loss of ProCharTS was attributed to the disruption of charged amino acid side-chain interactions accompanying protein unfolding.

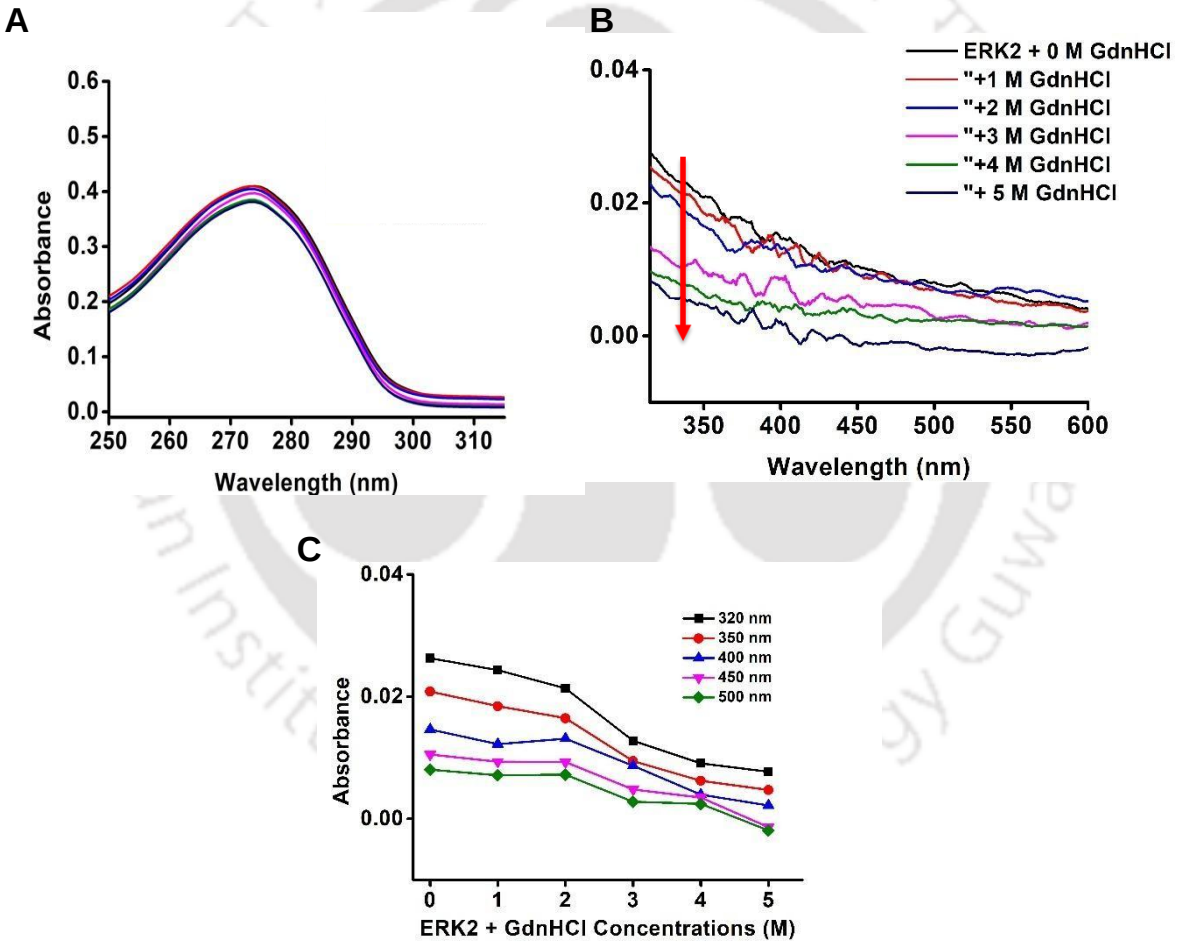

Figure 5.4: Absorbance spectra A. 250 - 315 nm and B. 315 – 600 nm for 20 µM ERK2 unfolding at different GdnHCL concentrations in 20 mM phosphate buffer at pH 7.5. Subfigure C indicate the change with respect to 0 M in ProCharTS absorbance at various wavelengths versus time.

These spectroscopic observations confirm that HuL and ERK2 undergoes significant conformational changes in the presence of GdnHCl, leading to the unfolding of its tertiary structure. The alterations in ProCharTS further suggest that the charge transfer interactions within the protein are affected by the unfolding process, providing insights into the structural dynamics of HuL and ERK2 under denaturing conditions.

The results revealed a substantial decrease in Protein Charge Transfer Spectra (ProCharTS) absorbance upon unfolding. ProCharTS absorbance arises from electronic transitions involving charged amino acid side chains, such as those of lysine, glutamate, Arginine, Aspartate and Histidine, which are sensitive to their spatial proximities within the protein's three-dimensional structure [Prasad et al., 2017; Alom et al., 2023]. As unfolding progresses, the disruption of these proximities leads to a decrease in ProCharTS absorbance. This observation underscores the utility of ProCharTS as a label-free, intrinsic probe for monitoring structural changes in proteins, particularly those rich in charged residues. The sensitivity of ProCharTS to alterations in the spatial arrangement of charged groups makes it a valuable tool for studying protein unfolding dynamics under various denaturing conditions.

To validate the findings from Protein Charge Transfer Spectra (ProCharTS) absorbance measurements, complementary biophysical techniques: circular dichroism (CD) spectroscopy [Gupta et al., 2023], intrinsic tryptophan fluorescence [Duy et al., 2006], and 8-anilinonaphthalene-1-sulfonic acid (ANS) binding assays [Hawe et al., 2008] were employed. Each of these methods offers unique insights into different aspects of protein structure and stability, thereby providing a comprehensive understanding of the unfolding process.

5.2.4 Detection of Protein Unfolding using Circular Dichroism

CD spectroscopy is a powerful tool for assessing the secondary structure of proteins. It measures the differential absorption of left- and right-circularly polarized light, which arises due to the chiral nature of protein structures. In the far-UV region (190–250 nm), CD spectra can reveal characteristic signatures of α-helices, β-sheets, and random coils. Upon unfolding,

proteins typically exhibit a decrease in α-helical content and an increase in random coil structures, leading to notable changes in the CD spectrum. This technique thus serves as a sensitive indicator of alterations in secondary structure during protein denaturation.

In the far-UV region (190–250 nm), α-helical structures exhibit characteristic negative ellipticity minima at approximately 208 nm and 222 nm. The ellipticity at 222 nm is commonly used as a quantitative measure of α-helical content in proteins [Wei et al., 2016].

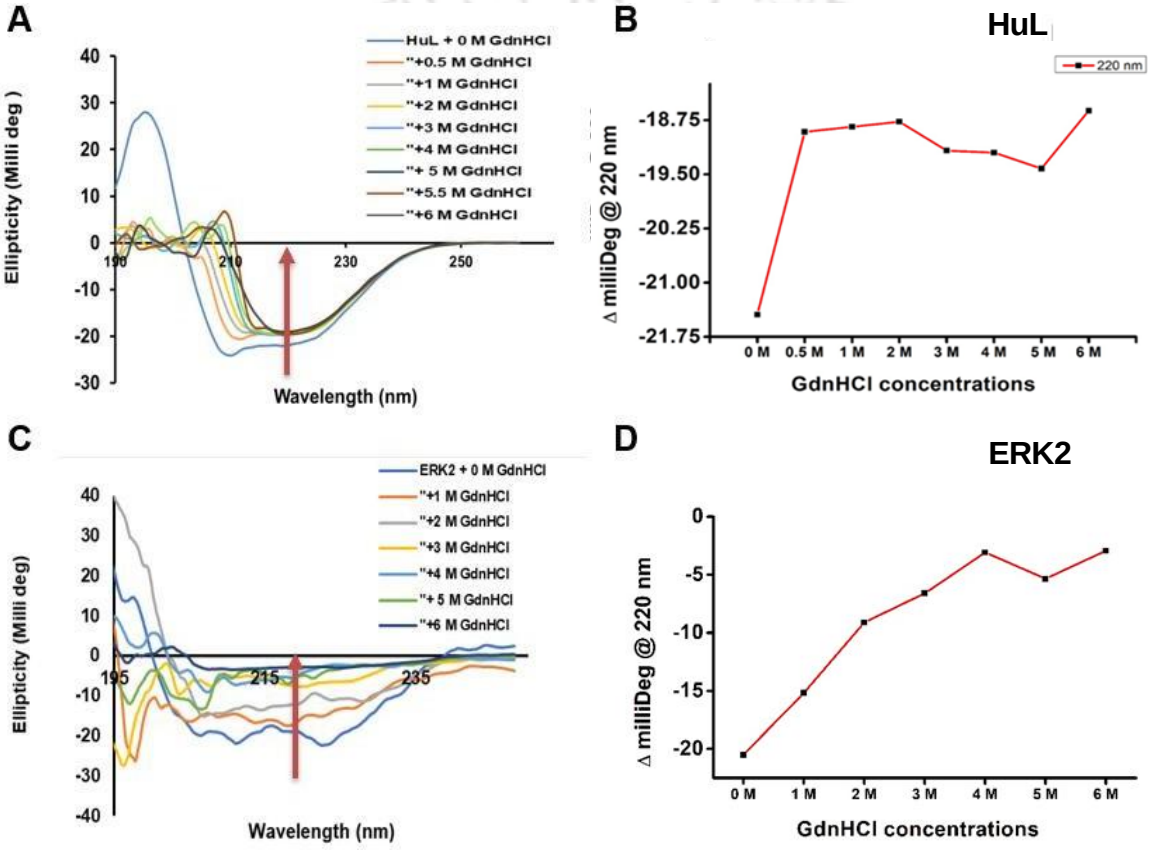

Figure 5.5: Monitoring Hul and ERK2 unfolding using CD spectroscopy. Panel A and C: CD spectra for human lysozyme unfolding (A) and ERK2 unfolding (C) at different GdnHCl concentrations. Panel B and D shows the change in ellipticity at 220 nm versus concentration of GdnHCl.

When proteins such as human lysozyme (HuL) and extracellular signal-regulated kinase 2 (ERK2) are subjected to progressively increasing concentrations of the chemical denaturant guanidinium hydrochloride (GdnHCl), their native secondary structures gradually lose stability and begin to unfold. This structural transition is readily detected using circular

dichroism (CD) spectroscopy, where a pronounced decrease in negative ellipticity at 220 nm is observed, a characteristic signal of α-helical content (Figure 5.5). The loss of negative ellipticity reflects the disruption of intramolecular hydrogen bonds that stabilize α-helices, ultimately leading to the collapse of the protein's secondary structure.

Interestingly, HuL and ERK2 exhibit distinct unfolding profiles. While both proteins experience a progressive decline in α-helical content with increasing GdnHCl concentration, the onset and steepness of this decline differ, suggesting variations in their intrinsic conformational stability. Such differences may be attributed to variations in tertiary packing density, the number and arrangement of disulfide bonds, or the distribution of hydrophobic and charged residues within each protein.

Importantly, the structural loss detected by CD spectroscopy is consistent with the ProCharTS measurements, where unfolding is accompanied by a substantial reduction in charge–charge interactions between amino acid side chains. The diminishing ProCharTS signal across multiple wavelengths parallels the loss of α-helical structure, reinforcing the conclusion that GdnHCl-induced unfolding disrupts both the secondary structure and the electrostatic interaction network that stabilizes the native fold. Together, these complementary techniques provide a cohesive picture of the denaturation process from both structural and interaction-based perspectives.

Further Extrinsic Chromophores such as ANS and intrinsic chromophores such as Trp fluorescence and ProCharTS luminescence were used to detect unfolding explained in the later sections.

5.2.5 Detection of Protein Unfolding using tryptophan fluorescence

Tryptophan steady state fluorescence within proteins are sensitive to their local environment, making their intensity a valuable probe for monitoring tertiary structure changes. In a folded protein, tryptophan residues are often buried within hydrophobic cores.

In the unfolding of human lysozyme (HuL) (Figure: 5.6 A and B), an atypical spectroscopic behaviour is observed: a decrease in tryptophan fluorescence intensity accompanied by a blue shift in the emission maximum. This phenomenon deviates from the conventional

expectation where protein unfolding leads to a red shift in tryptophan fluorescence due to increased exposure of tryptophan residues to the polar aqueous environment

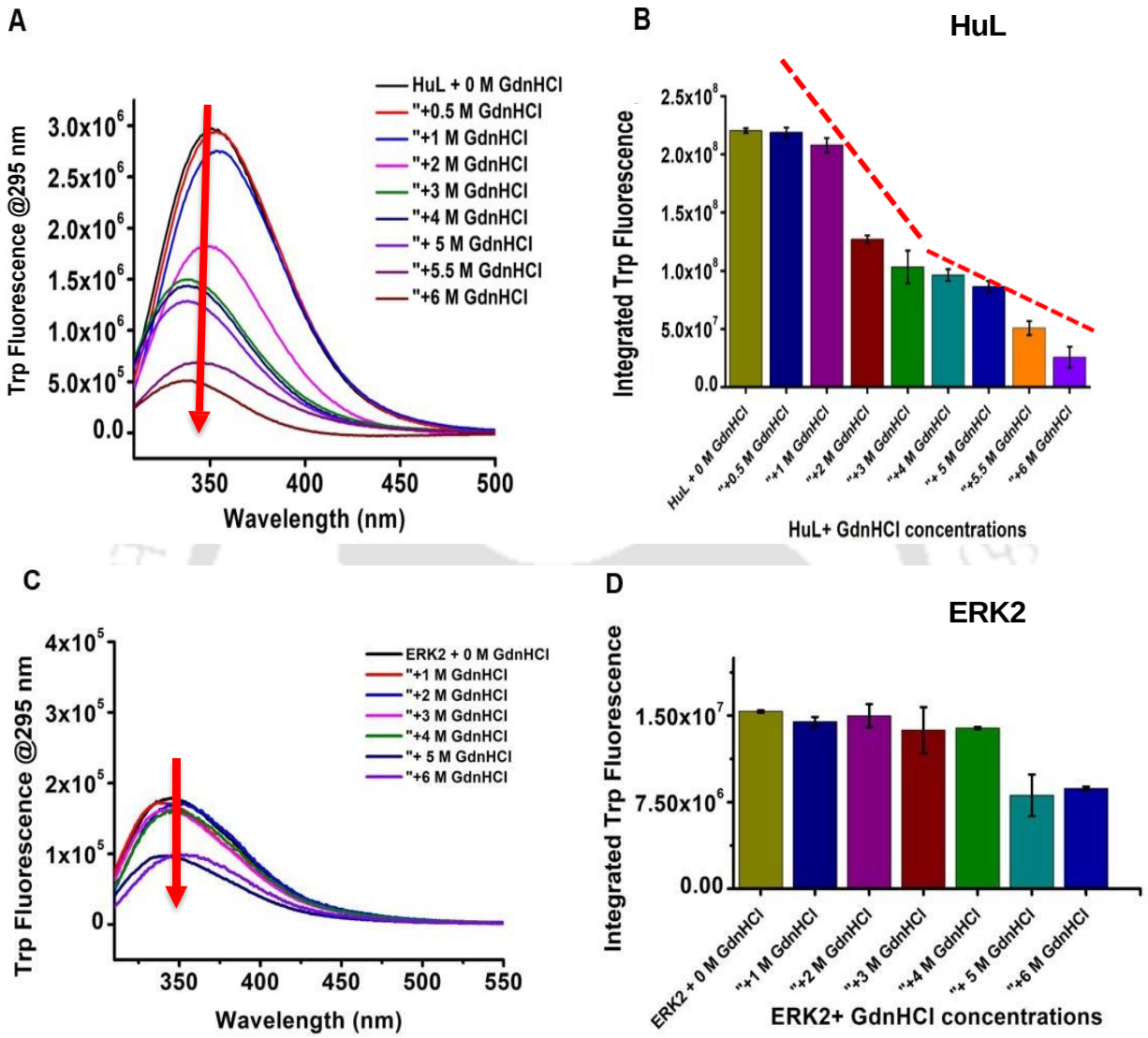

Figure 5.6: Tryptophan fluorescence spectra (λ_{ex} 295 nm) for HuL (A and B) and ERK2 (C and D) unfolding at GdnHCl concentrations. Unfolding show the decrease in Tryptophan fluorescence spectra. 15 µM of protein was used for the reaction.

The observed blue shift, characterized by a movement of the emission peak toward shorter wavelengths (~320 nm) (Figure 5.7A), indicates that Trp residues experience a more hydrophobic local environment in the unfolded state compared to the native fold [Moller et al., 2006]. This suggests that unfolding does not produce a fully extended random coil; instead, the polypeptide chains may adopt partially folded intermediates or aggregation-

prone collapsed conformations in which Trp residues are buried within non-native hydrophobic clusters.

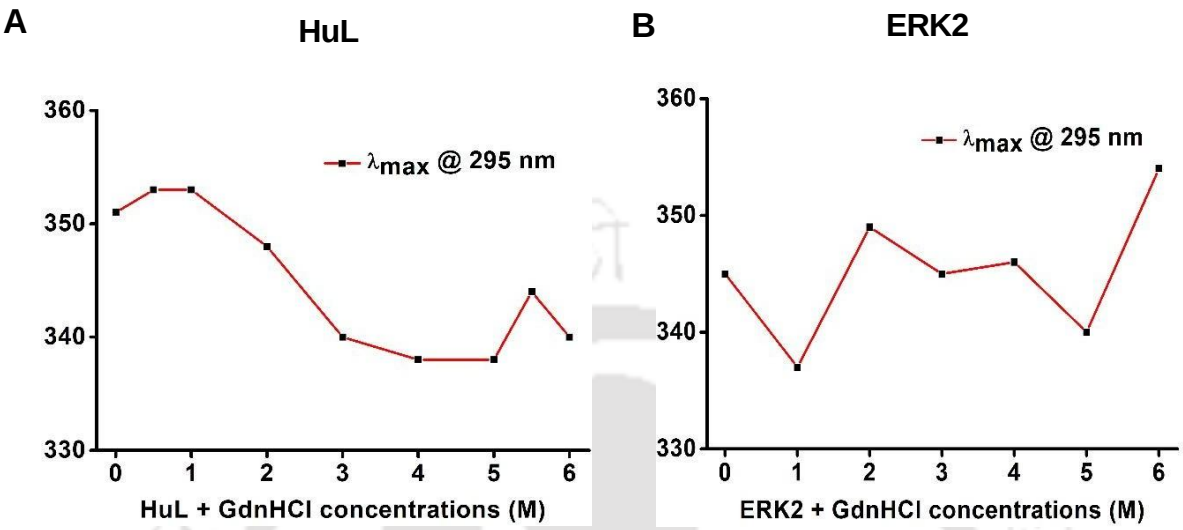

Figure 5.7: Emission maxima for Trp fluorescence in Hul (A) and ERK2 (B) proteins.

The concurrent decrease in trp fluorescence intensity can be attributed to self-quenching effects due to conformational change occurring within the protein. In densely packed environments, tryptophan residues are in close proximity, facilitating non-radiative energy transfer between them, which quenches fluorescence. Additionally, the altered microenvironment may introduce new quenching interactions, further diminishing fluorescence intensity. In the unfolded or partially folded states observed here, these quenching interactions are increased either due to rearrangement of side chains or exposure of Trp residues within hydrophobic pockets leading to lower quantum yield.

Together, the blue shift and decreased fluorescence intensity point to an unfolding pathway that involves hydrophobic collapse rather than complete chain extension, consistent with the structural and interaction-level changes detected by CD spectroscopy and ProCharTS measurements.

In the unfolding studies of ERK2 (figure 5.6 C and D), intrinsic tryptophan fluorescence measurements revealed a decrease in fluorescence intensity without a significant shift in the emission maximum wavelength (Figure 5.7B). This observation suggests that, upon denaturation, the tryptophan residues in ERK2 become more solvent-exposed, leading to

fluorescence quenching, yet their local environments do not undergo substantial polarity changes.

Typically, protein unfolding results in a red shift in tryptophan fluorescence emission due to the transition of tryptophan residues from hydrophobic cores to polar aqueous environments. However, the absence of a notable spectral shift in ERK2 (Figure 5.7B) indicates that its tryptophan residues may already reside in relatively polar or solvent-accessible regions in the native state, or that the unfolding process does not significantly alter their microenvironments. In case of ERK2, not much of a spectral shift is observed upon unfolding. Although there is decrease in the intensity of tryptophan fluorescence.

Hence, detection of protein unfolding using Tryptophan fluorescence depends on several factors such as the solvent exposure of the Tryptophan molecule and even quenching.

5.2.6 Detection of Protein Unfolding using ANS fluorescence

ANS is a fluorescent dye that exhibits increased fluorescence upon binding to hydrophobic regions of proteins. In native proteins, hydrophobic regions are typically buried; however, unfolding exposes these areas, allowing ANS to bind and fluoresce. The increase in ANS fluorescence intensity upon protein denaturation serves as an indicator of the exposure of hydrophobic patches, providing insights into the unfolding process and the formation of intermediate states.

The increase in ANS fluorescence upon protein unfolding is a well-documented phenomenon. For instance, studies have shown that ANS binds strongly to hydrophobic regions exposed during the partial unfolding of proteins, leading to enhanced fluorescence signals. This property of ANS makes it a valuable tool for monitoring conformational changes and the exposure of hydrophobic surfaces during protein folding and unfolding processes [Hagan et al., 2010].

During the unfolding of human lysozyme (HuL) and extracellular signal-regulated kinase 2 (ERK2), a notable increase in 8-anilinonaphthalene-1-sulfonic acid (ANS) fluorescence intensity is observed (Figure 5.8). This enhancement indicates the exposure of hydrophobic regions within these proteins, which are typically buried in their native conformations.

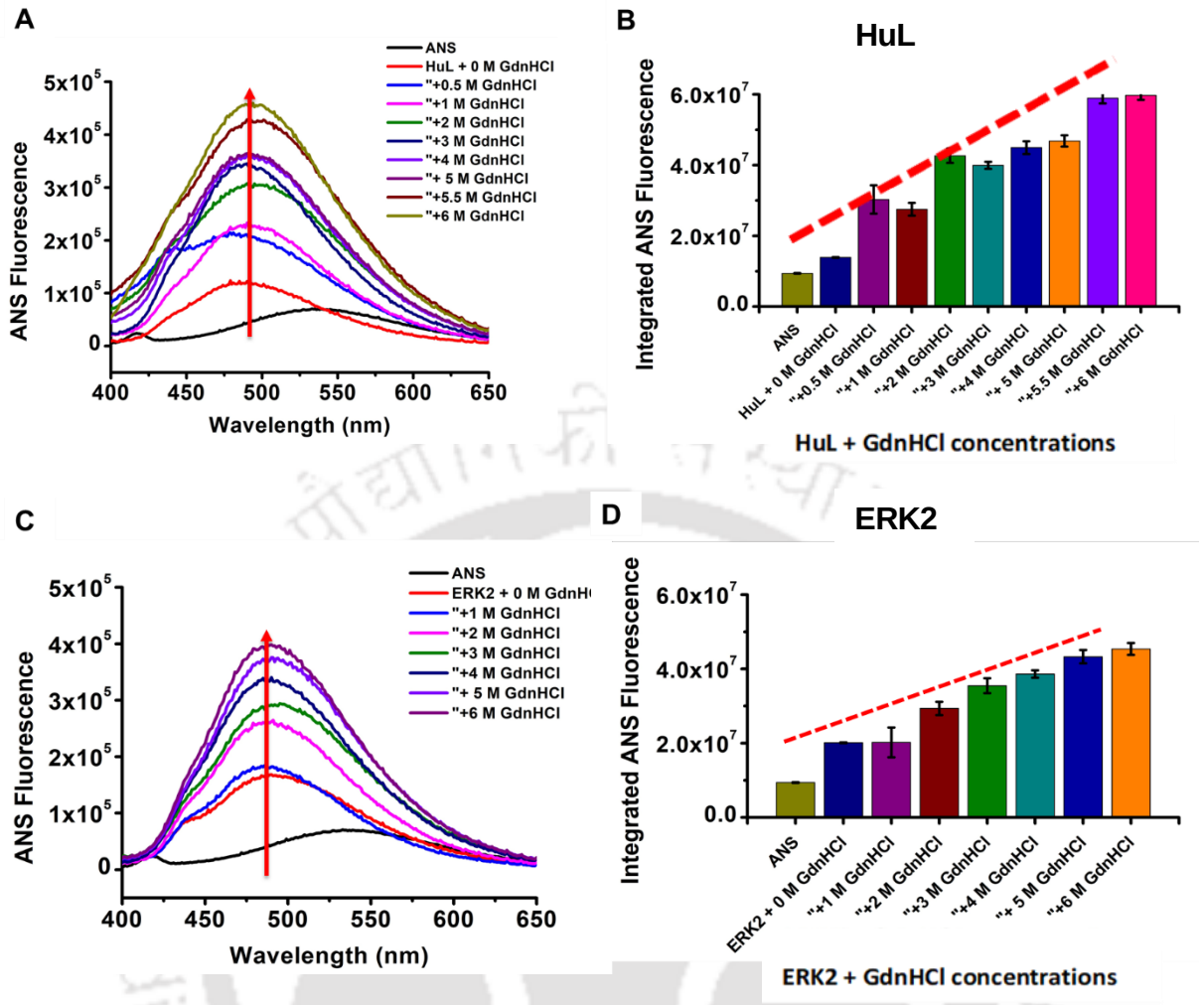

Figure 5.8: ANS Fluorescence spectra (λ_{ex} 380 nm) for Hul (Panel A and B) and ERK2 (Panel C and D) unfolding at GdnHCl concentrations. 10 µM of protein was used for the reaction.

In the context of HuL and ERK2, the observed increase in ANS fluorescence upon unfolding underscores the structural rearrangements these proteins undergo, highlighting the exposure of hydrophobic regions that were previously inaccessible in their native states. This information is crucial for understanding the folding dynamics and stability of these proteins under denaturing conditions. The increase in ANS fluorescence therefore serves as a sensitive indicator of the exposure of hydrophobic regions, complementing CD spectroscopy data (loss of secondary structure) and ProCharTS measurements (loss of electrostatic contacts).

5.2.7 Detection of Protein Unfolding using ProCharTS luminescence

In addition to absorbance measurements, ProCharTS luminescence experiment was also performed to further evaluate the effects of protein unfolding. Luminescence spectra were recorded using two excitation wavelengths: 340 nm and 355 nm. For excitation at 340 nm, emission was collected over the range of 360–600 nm, while for excitation at 355 nm, emission was monitored from 375–600 nm (Figures 5.8 and 5.9). In both cases, a gradual and consistent decrease in luminescence intensity was observed as the concentration of guanidinium hydrochloride (GdnHCl) increased, indicating progressive protein unfolding. During the unfolding of human lysozyme (HuL) and extracellular signal-regulated kinase 2 (ERK2), distinct patterns emerge in their Protein Charge Transfer Spectra (ProCharTS) luminescence responses to increasing concentrations of guanidine hydrochloride (GdnHCl), reflecting differences in their structural stability and unfolding mechanisms (Figures 5.8 and 5.9).

For HuL, ProCharTS luminescence remains relatively stable up to approximately 0.5 M GdnHCl. Beyond this concentration, a pronounced and abrupt decrease in luminescence intensity is observed (Figure 5.9). This sharp decline suggests a cooperative unfolding process, where HuL maintains its native conformation until a critical denaturant threshold is surpassed, leading to rapid structural disintegration. The sudden exposure of previously buried charged residues likely disrupt the specific charge-transfer interactions responsible for ProCharTS luminescence, resulting in the observed decrease.

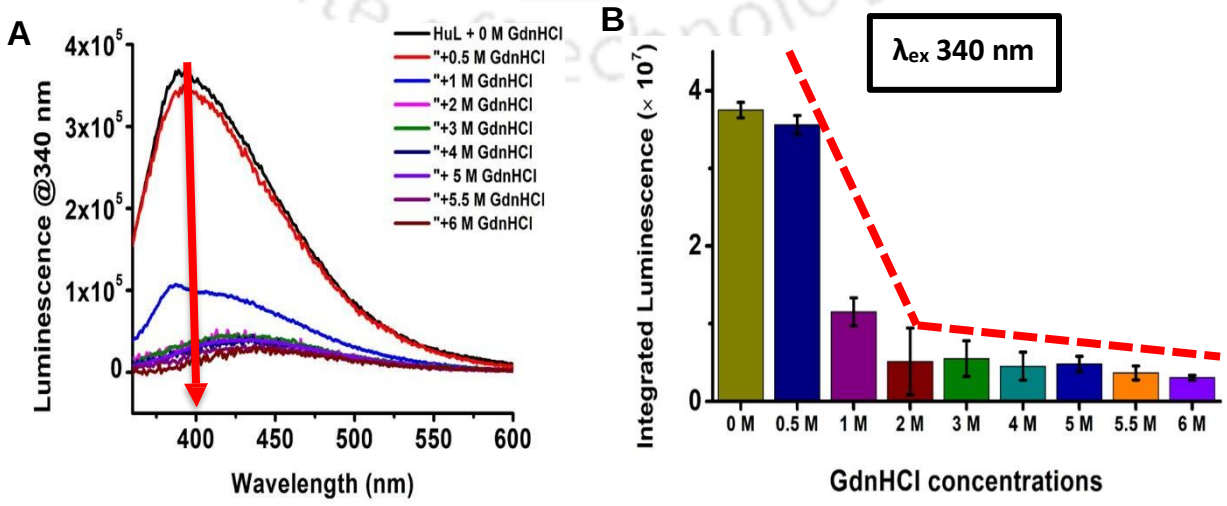

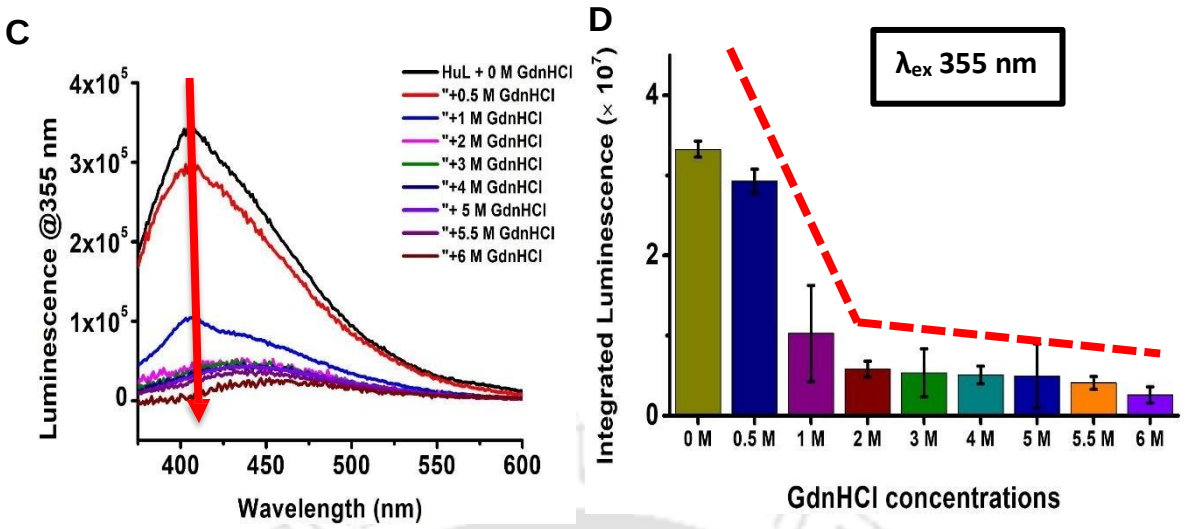

Figure 5.9: Monitoring Hul unfolding using ProCharTS luminescence at λ_{ex} 340 nm and λ_{ex} 355 nm with their emissions collected at 360 – 600 nm and 375 – 600 nm respectively.

In contrast, ERK2 exhibits a gradual decrease in ProCharTS luminescence across the entire range of 0 to 6 M GdnHCl (Figure 5.9). This continuous decline indicates a more progressive unfolding pathway, possibly involving intermediate states where partial exposure of charged residues occurs incrementally. Such a mechanism suggests that ERK2's structure unfolds in a less cooperative manner compared to HuL, with gradual disruption of charge-transferinteractions leading to a steady reduction in luminescence. The absence of a sharp transition point implies that ERK2's conformational stability is distributed across multiple structural domains, each responding differently to denaturant exposure

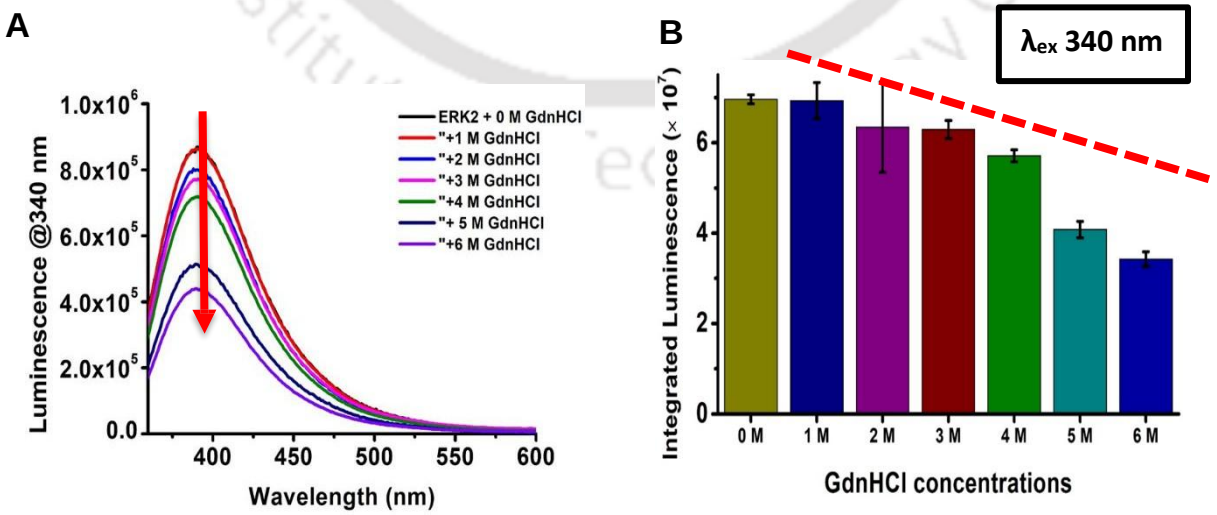

.

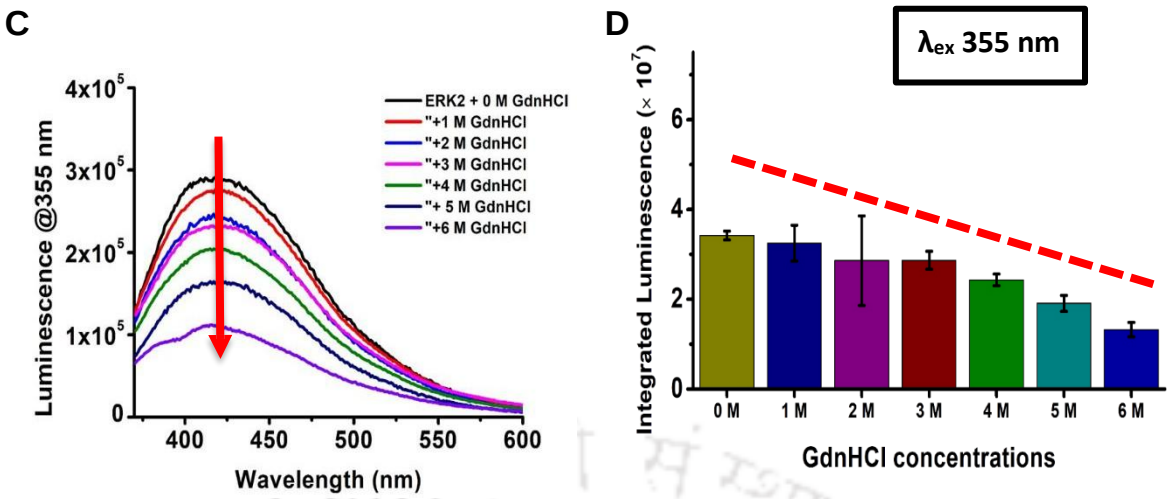

Figure 5.10: Monitoring ERK2 unfolding using ProCharTS luminescence at λ_{ex} 340 nm and λ_{ex} 355 nm with their emissions collected at 360 – 600 nm and 375 – 600 nm respectively.

These contrasting luminescence profiles underscore the utility of ProCharTS as a sensitive probe for monitoring protein unfolding. The technique effectively captures the nuances of structural transitions, providing insights into the stability and folding pathways of different proteins under denaturing conditions.

The decline in ProCharTS absorbance and luminescence suggests that the unfolding process disrupts the specific charge transfer interactions responsible for generating the luminescence. As the native structure of the protein is lost, the proximity and orientation of charged amino acid side chains critical for efficient charge transfer are altered or eliminated, leading to reduced luminescence efficiency. These observations further support the conclusion that ProCharTS is sensitive to conformational changes in proteins and can serve as an effective tool for detecting structural perturbations during the unfolding process.

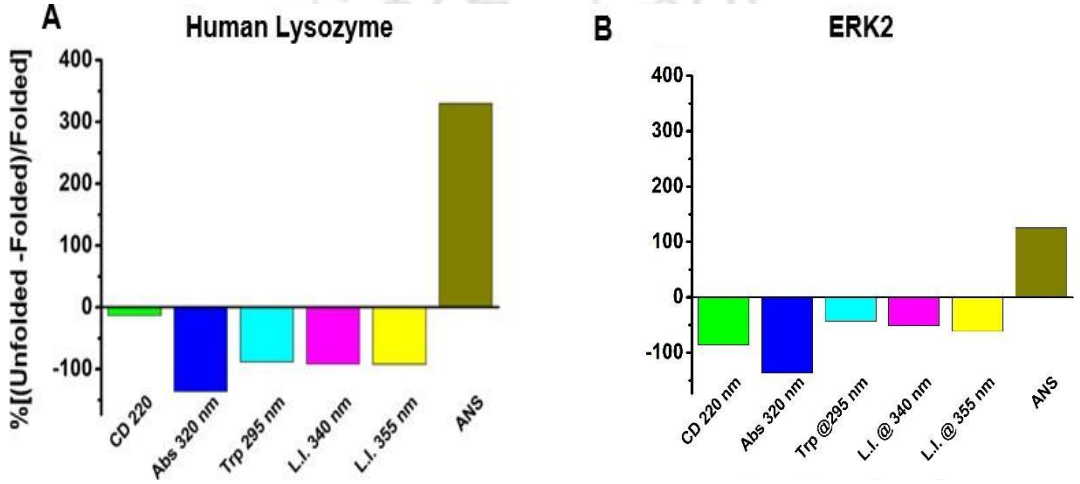

Figure 5.11: Percentage change in the unfolded states as compared to folded states of A. Human Lysozyme and B. ERK2 in the various techniques compared.

To summarize the findings, a comparative plot was generated incorporating results from various techniques used to detect unfolding, including ProCharTS absorbance and luminescence data (Figure 5.11). The analysis included the values for the lowest anhighest concentration of GdnHCl used. The analysis clearly demonstrated that Protein Charge Transfer Spectra (ProCharTS) is a comparatively efficient and sensitive method for detecting unfolding in proteins. Furthermore, these results suggest broader applicability of this technique, opening new avenues for the detection and characterization of other protein unfolding across a wide range of proteins.

5.3 Conclusions

1. **ProCharTS absorbance decreases during protein unfolding induced by guanidinium hydrochloride (GdnHCl)**

- GdnHCl disrupts the native fold by weakening stabilizing interactions, leading to a measurable drop in the ProCharTS absorbance.
- This drop is a direct optical signature of conformational changes within the protein.

2. **Reduction in ProCharTS reflects the loss of electrostatic interactions between charged amino acid side chains**

- In the folded state, charged residues are often positioned in specific orientations to form salt bridges or clustered charge networks.
- Upon unfolding, the polypeptide expands, increasing the average distance between these charges and reducing their interaction strength, which lowers the ProCharTS response.

3. **Higher sensitivity compared to CD or ANS fluorescence**

- ProCharTS absorbance detects early tertiary structure perturbations, even when secondary structure (monitored by CD) or hydrophobic exposure (monitored by ANS) remain largely unchanged.

- This allows detection of subtle unfolding events at lower denaturant concentrations.

4. **Designed to monitor changes in the spatial arrangement of charged groups**

- ProCharTS specifically responds to the relative positioning of charged side chains, making it highly sensitive to rearrangements in tertiary and quaternary protein architecture.
- This enables it to distinguish between compact partially folded states and fully unfolded conformations.

5. **Dynamic alterations in charge distribution during unfolding**

- As unfolding progresses, the movement of charged residues alters the electrostatic landscape of the protein.
- These rearrangements lead to quantifiable shifts in both ProCharTS absorbance (static readout) and luminescence (dynamic readout), reflecting progressive loss of native packing.

6. **Reliable readout of the folded state**

- Because ProCharTS responds to the integrity of electrostatic contacts, it serves as a precise indicator of whether a protein remains in a native-like conformation.
- When used alongside CD (secondary structure) and ANS fluorescence (hydrophobic exposure), ProCharTS fills a critical gap by reporting directly on tertiary electrostatic integrity, enabling a more complete mapping of the unfolding pathway.

CHAPTER 6

THESIS SUMMARY AND FUTURE DIRECTIONS

6.1 Thesis Summary

The discovery of novel intrinsic chromophores in apo-proteins that lack aromatic amino acids has attracted considerable attention in recent years, as it challenges the conventional understanding of protein photophysics. Elucidating the mechanisms underlying these unexpected optical properties has therefore become an important area of research. In this thesis, we investigate Protein Charge Transfer Spectroscopy (ProCharTS) as a potential origin of such intrinsic absorbance and luminescence phenomena, aiming to provide deeper insight into the fundamental principles governing these observations.

This thesis investigates the use of **Protein Charge Transfer Spectroscopy (ProCharTS)** as a label-free analytical approach for tracking key molecular processes, including protein phosphorylation, aggregation, and unfolding.

Chapter 3 focuses on the application of ProCharTS absorbance and luminescence to investigate phosphorylation-dependent changes in both model peptides (LG7, LG7 P, KK9, and KK9 P) and highly charged proteins, alpha casein and beta casein. The study reveals clear differences in ProCharTS signals between phosphorylated and unphosphorylated peptides, as well as between phosphorylated and dephosphorylated caseins, demonstrating the method's sensitivity to phosphorylation states. Moreover, the higher extinction coefficients observed in proteins relative to peptides suggest that proximal charged residues enhance electron transfer, independent of the specific amino acid types involved. Collectively, these results establish ProCharTS as a powerful, non-invasive, label-free technique for detecting protein phosphorylation and gaining insights into protein structural dynamics.

Chapter 4 investigates the utility of Protein Charge Transfer Spectra (ProCharTS) in tracking protein aggregation, using alpha synuclein and human lysozyme (HuL) as model systems. Aggregation involves the formation of new intermolecular contacts among charged residues, which enhances photoinduced electron transfer and leads to elevated ProCharTS absorbance and luminescence signals. A progressive increase in ProCharTS responses was observed during the aging of alpha synuclein and HuL aggregates, consistent with results from

conventional assays such as ThT fluorescence, as well as structural insights from CD spectroscopy. Notably, ProCharTS demonstrated superior sensitivity in identifying early oligomeric species compared to ThT and CD, highlighting its ability to detect aggregation at earlier stages.The substantially higher extinction coefficients of aged aggregates relative to monomers further emphasize the contribution of charged residue interactions to intrinsic luminescence. Collectively, these findings establish ProCharTS as a sensitive, label-free method for monitoring aggregation kinetics and structural transitions in proteins.

Chapter 5 examines the application of Protein Charge Transfer Spectra (ProCharTS) for monitoring protein unfolding, using human lysozyme (HuL) and extracellular signal-regulated kinase 2 (ERK2) as representative systems. Both proteins are natively folded and enriched in charged residues, making them suitable for investigating charge transfer–dependent luminescence. Unfolding perturbs the spatial arrangement of charged side chains, leading to reduced efficiency of charge transfer and a corresponding decline in ProCharTS absorbance and luminescence.

Chemical denaturation experiments confirmed this trend, showing significant decreases in absorbance across 325–800 nm and in luminescence upon excitation at 340 and 355 nm. These observations closely paralleled structural and fluorescence-based results from CD spectroscopy, tryptophan fluorescence, and ANS assays. Together, the findings underscore the ability of ProCharTS to sensitively detect unfolding events in charged proteins, reinforcing its potential as a complementary, label-free tool for probing protein stability.

Taken together, these studies establish ProCharTS as a robust and sensitive technique capable of capturing diverse molecular events in proteins without the need for external labels. Its ability to detect phosphorylation states, early aggregation intermediates, and unfolding transitions highlights its potential as both a fundamental research tool and a platform for applications in disease diagnostics and therapeutic screening.

6.2 Future Directions

The sensitivity of ProCharTS to factors such as the spatial proximity of charged side chains, the presence of counter ions, pH, and solvent polarity underscores its potential as a versatile tool for probing a wide range of molecular processes. These include protein–protein and protein–ligand interactions, detection of other post-translational modifications such as acetylation, succinylation and protein–DNA/RNA interactions, among others. Beyond these applications, ProCharTS holds promise for detecting heavy metals by exploiting proteins capable of binding metal ions and undergoing structural rearrangements. As demonstrated in this work, ProCharTS can also be applied as a label-free approach to monitor structural changes in proteins.

The ProCharTS phenomenon has been demonstrated in both monomeric proteins and aggregates, with the key role of the extinction coefficient in driving the observed signals already established. However, a major limitation that hinders the transition of ProCharTS from spectroscopic studies to in vivo applications is its intrinsically low molar absorptivity and quantum yield. Enhancing the quantum efficiency by promoting radiative recombination of the transferred electrons could significantly improve the utility of ProCharTS, enabling its development into a more powerful tool for investigating diverse protein dynamics.

Furthermore, since ProCharTS has been successfully employed to monitor the real-time kinetics of both protein aggregation and unfolding, it presents an exciting opportunity to investigate the influence of potential drug candidates that either inhibit or accelerate these processes. Utilizing ProCharTS for drug screening could greatly expand its scope, establishing it as a versatile platform for assessing therapeutic modulators of protein dynamics.

APPENDIX

1) Polyacrylamide gel electrophoresis:

Composition of resolving and stacking gels:

Components	Resolving gel (15 %)	Stacking gel (5 %)	Stock solutions
Acrylamide solution	5 mL	0.83 mL	**29 % acrylamide, 1% bisacrylamide**
Resolving gel buffer	2.5 mL	-	**1.5 M Tris.HCl (pH 8.8)**
Stacking gel buffer	-	0.63 mL	**0.5 M Tris.HCl (pH 6.8)**
SDS solution	100 µL	50 µL	**10 % (w/v) SDS**
TEMED	5 µL	5 µL	**undiluted**
APS solution#	100 µL	50 µL	**10 % (w/v) APS**
H_20	2.3 mL	3.4 mL	
Total volume	**10 mL**	**5 mL**	

#: Freshly prepared

Coomassie staining solution:

1) 0.25 % (w/v) Brilliant Blue R

2) 40 % (v/v) methanol

3) 7 % (v/v) acetic acid

Destaining solution:

1) 30 % v/v Methanol

2) 10 % v/v glacial acetic acid

5 X gel loading buffer:

1) 0.05 % bromophenol blue

2) 40 % sucrose

3) 0.1 M EDTA (pH 8.0)

4) 0.5 % SDS.

5) 4.2 % β-mercaptoethanol

10 X Tris-glycine cathode buffer:

1) 30 g Tris base

2) 144 g Glycine

3) 10 g SDS

The three components were mixed in 1 L of H_2O to get 10 X running buffer of pH ~8.3 with pH adjustment not being required.

1 X Tris-Tricine cathode buffer

1) 0.1 M Tris

2) 0.1 M Tricine

3) 0.1 % SDS

5 X anode buffer

0.2 M Tris.Cl (pH adjusted to 8.9)

LIST OF PUBLICATIONS

Publication(s) from the thesis:

1. Singh A, Gadicherela H, Swaminathan R. Monitoring Phosphorylation in Proteins Using a Novel Tool: Protein Charge Transfer Spectra. Biophysical Journal, 2023, 122(3 Suppl.), 546A–547A.
2. Singh, A.; Gadicherela, H; Swaminathan R. Near UV- Visible electronic absorption arising from charged amino acids: A probe to monitor Phosphorylation in proteins. *(Manuscript under preparation).*
3. Singh A.; Kumar, A; Swaminathan, R. Luminescence from charge transfer states among protein aggregates: A simple tool to distinguish between the nature of aggregates. *(Manuscript under preparation).*
4. Singh A; Swaminathan R. Role of conformational alteration in the the ProCharTS of biologically relevant proteins. *(Manuscript under preparation).*

Publication outside the thesis:

Alom SE, Swaminathan K, Nuzelu V, Singh A, Rocquigny HD, Swaminathan R. Label-Free Tracking of HBV Core Protein Capsid Assembly in Real-Time Using Protein Charge Transfer Spectra. Biomacromolecules 2024, 25(10), 6425–6438.

LIST OF CONFERENCES

Conferences attended:

a. Participated in international conference "67th Annual Meeting of Biophysical Society" (BPS2023), Feb 19-23, organized by BPS in San Francisco, California.
b. Participated and presented poster in "North East Research Conclave (NERC) 2022, May 20-22, organized by Government of India, Government of Assam and IIT Guwahati.
c. Participated in "National Workshop on Fluorescence and Raman Spectroscopy" (FCS2020), Oct 25-29, organized by TIFR and IIT Bombay, India
d. Participated in "National Workshop on Fluorescence and Raman Spectroscopy" (FCS2018), Nov 12-17, organized by JNU and IIT Delhi, India
e. Participated and volunteered in "National Workshop on Fluorescence and Raman Spectroscopy" (FCS2017), Dec 17-21, organized IIT Guwahati, India

REFERENCES

References

1. Agashe, V. R., & Udgaonkar, J. B. (1995). Thermodynamics of denaturation of barstar: Evidence for cold denaturation and evaluation of the interaction with guanidine hydrochloride. *Biochemistry, 34*(10), 3286–3299. https://doi.org/10.1021/bi00010a027
2. Aguzzi, A., & Calella, A. M. (2009). Prions: Protein aggregation and infectious diseases. *Physiological Reviews, 89*(4), 1105–1152. https://doi.org/10.1152/physrev.00006.2009
3. Aguzzi, A., & O'Connor, T. (2010). Protein aggregation diseases: Pathogenicity and therapeutic perspectives. *Nature Reviews Drug Discovery, 9*(3), 237–248. https://doi.org/10.1038/nrd3050
4. Ahmad, B., Ahmed, M. Z., Haq, S. K., & Khan, R. H. (2005). Guanidine hydrochloride denaturation of human serum albumin originates by local unfolding of some stable loops in domain III. *Biochimica et Biophysica Acta (BBA) - Proteins and Proteomics, 1750*(1), 93–102. https://doi.org/10.1016/j.bbapap.2005.03.010
5. Akita, S., Umezawa, N., Kato, N., & Higuchi, T. (2008). Array-based fluorescence assay for serine/threonine kinases using specific chemical reaction. *Bioorganic & Medicinal Chemistry, 16*(15), 7788–7794. https://doi.org/10.1016/j.bmc.2008.07.011
6. Alom, S. E., & Swaminathan, R. (2023). Protein charge transfer spectra in a monomeric protein with no lysine. *Physical Chemistry Chemical Physics, 25*(25), 16626–16642. https://doi.org/10.1039/D3CP01953E
7. Alom, S. E., Swaminathan, K., Nuzelu, V., Singh, A., & Swaminathan, R. (2024). Label-free tracking of Hepatitis B virus core protein capsid assembly in real time using protein charge transfer spectra. *Biomacromolecules, 25*(10), 6425–6438. https://doi.org/10.1021/acs.biomac.4c00812
8. Ansari, M. Z., Ahmad, S., Khan, R. H., Alam, P., Hassan, M. I., Bhushan, R., Kabir-ud-Din, & Swaminathan, R. (2018). Protein charge transfer absorption spectra: An intrinsic probe to monitor structural and oligomeric transitions in proteins. *Faraday Discussions, 207*, 91–113. https://doi.org/10.1039/C8FD00041E
9. Antosiewicz, J. M., & Shugar, D. (2016). UV-Vis spectroscopy of tyrosine side-groups in studies of protein structure. Part 2: Selected applications. *Biophysical Reviews, 8*(2), 163–177. https://doi.org/10.1007/s12551-016-0201-1
10. Apter, B., Volovik, Y., Kochavi, E., Lerner, E., & Rosenbluh, M. (2020). Fluorescence waveguiding in amyloidogenic fibers. In *Neurophotonics* (Vol. 11360, pp. 63–72). SPIE. https://doi.org/10.1117/12.2553182
11. Arikuma, Y., Nakayama, H., Morita, T., & Kimura, S. (2010). Electron hopping over 100 Å along an α helix. *Angewandte Chemie International Edition, 49*(10), 1800–1804. https://doi.org/10.1002/anie.200905046
12. Arnaudov, L. N., & de Vries, R. (2005). Thermally induced fibrillar aggregation of hen egg white lysozyme. *Biophysical Journal, 88*(1), 515–526. https://doi.org/10.1529/biophysj.104.051037
13. Ashraf, G. M., Greig, N. H., Khan, T. A., Hassan, I., Tabrez, S., et al. (2014). Protein misfolding and aggregation in Alzheimer's disease and type 2 diabetes mellitus. *CNS & Neurological Disorders - Drug Targets, 13*(7), 1280–1293. https://doi.org/10.2174/18715273136661409170951111
14. Balzani, V., Bergamini, G., Campagna, S., & Puntoriero, F. (2007). Photochemistry and photophysics of coordination compounds: Overview and general concepts. In V. Balzani & S. Campagna (Eds.), *Photochemistry and photophysics of coordination compounds I* (pp. 1–36). Springer. https://doi.org/10.1007/128_2007_114

15. Barron, A. R. (2015). *Physical methods in chemistry and nanoscience*. Rice University.
16. Bhattacharya, A., et al. (2017). Direct evidence of intrinsic blue fluorescence from oligomeric interfaces of human serum albumin. *Langmuir, 33*(42), 10606–10615. https://doi.org/10.1021/acs.langmuir.7b02791
17. Bhattacharya, A., Prajapati, R., Chatterjee, S., & Mukherjee, T. K. (2014). Concentration dependent reversible self-oligomerization of serum albumins through intermolecular β-sheet formation. *Langmuir, 30*(50), 14894–14904. https://doi.org/10.1021/la5034909
18. Bent, D. V., & Hayon, E. (1975). Excited state chemistry of aromatic amino acids and related peptides. I. Tyrosine. *Journal of the American Chemical Society, 97*(10), 2599–2606. https://doi.org/10.1021/ja00843a004
19. Blackburn, K., & Goshe, M. B. (2009). Challenges and strategies for targeted phosphorylation site identification and quantification using mass spectrometry analysis. *Briefings in Functional Genomics and Proteomics, 8*(2), 90–103. https://doi.org/10.1093/bfgp/eln048
20. Calabresi, P., Mechelli, A., Natale, G., et al. (2023). Alpha-synuclein in Parkinson's disease and other synucleinopathies: From overt neurodegeneration back to early synaptic dysfunction. *Cell Death & Disease, 14*(1), 176. https://doi.org/10.1038/s41419-023-05692-9
21. Calero, M., & Gasset, M. (2005). Fourier transform infrared and circular dichroism spectroscopies for amyloid studies. In M. Fändrich (Ed.), *Amyloid proteins* (pp. 129–151). Springer. https://doi.org/10.1385/1-59259-898-4:129
22. Campagna, S., Puntoriero, F., Nastasi, F., Bergamini, G., & Balzani, V. (2007). Photochemistry and photophysics of coordination compounds: Ruthenium. In V. Balzani & S. Campagna (Eds.), *Photochemistry and photophysics of coordination compounds I* (pp. 117–214). Springer. https://doi.org/10.1007/128_2007_118
23. Canfield, R. E. (1963). The amino acid sequence of egg white lysozyme. *Journal of Biological Chemistry, 238*(8), 2698–2707. https://doi.org/10.1016/S0021-9258(18)52053-4
24. Cantor, C. R., & Schimmel, P. R. (1980). *Biophysical chemistry: Part II: Techniques for the study of biological structure and function*. W. H. Freeman and Company.
25. Chaari, A., Fahy, C., Chevillot-Biraud, A., & Rholam, M. (2015). Insights into kinetics of agitation-induced aggregation of hen lysozyme under heat and acidic conditions from various spectroscopic methods. *PLOS ONE, 10*(11), e0142095. https://doi.org/10.1371/journal.pone.0142095
26. Chai, B. H., Zheng, J. M., Zhao, Q., & Pollack, G. H. (2008). Spectroscopic studies of solutes in aqueous solution. *Journal of Physical Chemistry A, 112*(11), 2242–2247. https://doi.org/10.1021/jp7101299
27. Chan, F. T. S., et al. (2013). Protein amyloids develop an intrinsic fluorescence signature during aggregation. *Analyst, 138*(7), 2156–2162. https://doi.org/10.1039/c3an36724a
28. Chang, J. Y., & Li, L. (2002). The unfolding mechanism and the disulfide structures of denatured lysozyme. *FEBS Letters, 511*(1–3), 73–78. https://doi.org/10.1016/S0014-5793(01)03291-5
29. Chang, R. (2005). *Physical chemistry for the biosciences*. University Science Books.
30. Chen, X., et al. (2018). Prevalent intrinsic emission from nonaromatic amino acids and poly (amino acids). *Science China Chemistry, 61*(3), 351–359. https://doi.org/10.1007/s11426-017-9204-7
31. Cid, M.-M., & Bravo, J. (2014). Structure elucidation in organic chemistry: The search for the right tools. John Wiley & Sons.
32. Cohen, P. (2009). Signal integration at the level of protein kinases, protein phosphatases and their substrates. Trends in Biochemical Sciences, 17(10), 408–413. https://doi.org/10.1016/0968-0004(92)90305-K

33. Creed, D. (1984). The photophysics and photochemistry of the near-UV absorbing amino acids—I. Tryptophan and its simple derivatives. Photochemistry and Photobiology, 39(4), 537–562. https://doi.org/10.1111/j.1751-1097.1984.tb03868.x
34. Crosby, G. A. (1975). Spectroscopic investigations of excited states of transition-metal complexes. Accounts of Chemical Research, 8(8), 231–238. https://doi.org/10.1021/ar50091a004
35. Darewich, M., et al. (2000). Dephosphorylation-induced structural changes in β-casein and its amphiphilic fragment in relation to emulsion properties. Biochimie, 82(3), 191–195. https://doi.org/10.1016/S0300-9084(00)00118-3
36. Del Mercato, L. L., Pompa, P. P., Maruccio, G., Torre, A. D., Sabella, S., et al. (2007). Charge transport and intrinsic fluorescence in amyloid-like fibrils. Proceedings of the National Academy of Sciences, 104(45), 18019–18024. https://doi.org/10.1073/pnas.0701822104
37. Dobson, C. M. (2003). Protein folding and misfolding. Nature, 426(6968), 884–890. https://doi.org/10.1038/nature02261
38. Duy, C., & Fitter, J. (2006). How aggregation and conformational scrambling of unfolded states govern fluorescence emission spectra. Biophysical Journal, 90(10), 3704–3711. https://doi.org/10.1529/biophysj.105.074427
39. Fink, A. L. (1998). Protein aggregation: Folding aggregates, inclusion bodies and amyloid. Folding and Design, 3(1), R9–R23. https://doi.org/10.1016/S1359-0278(98)00002-9
40. Gade Malmos, K., Blancas-Mejia, L. M., Weber, B., Buchner, J., Ramirez-Alvarado, M., et al. (2017). ThT 101: A primer on the use of thioflavin T to investigate amyloid formation. Amyloid, 24(1), 1–16. https://doi.org/10.1080/13506129.2017.1304905
41. Gomes, A. J., Lunardi, C. N., Rocha, F. S., & Patience, G. S. (2019). Experimental methods in chemical engineering: Fluorescence emission spectroscopy. Canadian Journal of Chemical Engineering, 97(8), 2168–2175. https://doi.org/10.1002/cjce.23496
42. Greenfield, N. J. (2006). Using circular dichroism spectra to estimate protein secondary structure. Nature Protocols, 1(6), 2876–2890. https://doi.org/10.1038/nprot.2006.202
43. Gregoire, S., Irwin, J., & Kwon, I. (2012). Techniques for monitoring protein misfolding and aggregation in vitro and in living cells. Korean Journal of Chemical Engineering, 29(6), 693–702. https://doi.org/10.1007/s11814-011-0239-3
44. Gupta, P., Islam, A., Ahmad, F., & Hassan, M. I. (2023). Applications of circular dichroism spectroscopy in studying protein folding, stability, and interaction. In P. Saudagar & T. Tripathi (Eds.), Protein folding dynamics and stability (pp. 1–23). Springer. https://doi.org/10.1007/978-981-99-3495-1_1
45. Guptasarma, P. (2008). Solution-state characteristics of the ultraviolet A-induced visible fluorescence from proteins. Archives of Biochemistry and Biophysics, 478(2), 127–129. https://doi.org/10.1016/j.abb.2008.07.009
46. Hagan, C., Johnson, R., Dhulesia, A., Dumoulin, M., Dumont, J., De Genst, E., Christodoulou, J., Robinson, C., Dobson, C., & Kumita, J. (2010). A non-natural variant of human lysozyme (I59T) mimics the in vitro behaviour of the I56T variant that is responsible for a form of familial amyloidosis. Protein Engineering, Design & Selection, 23(7), 499–506. https://doi.org/10.1093/protein/gzq027

47. Hameed, M., Ahmad, B., Fazili, K. M., Andrabi, K., & Khan, R. H. (2007). Different molten globule-like folding intermediates of hen egg white lysozyme induced by high pH and tertiary butanol. The Journal of Biochemistry, 141(5), 573–583. https://doi.org/10.1093/jb/mvm074
48. Hawe, A., Sutter, M., & Jiskoot, W. (2008). Extrinsic fluorescent dyes as tools for protein characterization. Pharmaceutical Research, 25(7), 1487–1499. https://doi.org/10.1007/s11095-007-9516-9
49. Hawe, A., Filipe, V., & Jiskoot, W. (2010). Fluorescent molecular rotors as dyes to characterize polysorbate-containing IgG formulations. Pharmaceutical Research, 27(2), 314–326. https://doi.org/10.1007/s11095-009-0015-1
50. Hill, S. E., Robinson, J., Matthews, G., & Muschol, M. (2009). Amyloid protofibrils of lysozyme nucleate and grow via oligomer fusion. Biophysical Journal, 96(9), 3781–3790. https://doi.org/10.1016/j.bpj.2009.01.040
51. Hof, M. (2003). Basics of optical spectroscopy. In J. Wiley & H. W. Siesler (Eds.), Handbook of spectroscopy. Wiley-VCH.
52. Homchaudhuri, L., & Swaminathan, R. (2001). Novel absorption and fluorescence characteristics of L-lysine. *Chemistry Letters*, *2001*(8), 844–845. https://doi.org/10.1246/cl.2001.844
53. Homchaudhuri, L., & Swaminathan, R. (2004). Near ultraviolet absorption arising from lysine residues in close proximity: A probe to monitor protein unfolding and aggregation in lysine-rich proteins. *Bulletin of the Chemical Society of Japan*, *77*(4), 765–769. https://doi.org/10.1246/bcsj.77.765
54. Hoyer, W., Antony, T., Cherny, D., Heim, G., Jovin, T. M., & Subramaniam, V. (2002). Dependence of α-synuclein aggregate morphology on solution conditions. *Journal of Molecular Biology*, *322*(2), 383–393. https://doi.org/10.1016/S0022-2836(02)00775-1
55. Hunter, T. (2000). Signaling—2000 and beyond. *Cell*, *100*(1), 113–127. https://doi.org/10.1016/S0092-8674(00)81688-8
56. Iyer, A., Petersen, N. O., Claessens, M. M. A. E., & Subramaniam, V. (2014). Amyloids of alpha-synuclein affect the structure and dynamics of supported lipid bilayers. *Biophysical Journal*, *106*(12), 2585–2594. https://doi.org/10.1016/j.bpj.2014.04.036
57. Jesus, C. S. H., Soares, H. T., Piedade, A. P., Cortes, L., & Serpa, C. (2021). Using amyloid autofluorescence as a biomarker for lysozyme aggregation inhibition. *Analyst*, *146*(8), 2383–2391. https://doi.org/10.1039/d0an02127h
58. Jong, K. H., Lee, J. Y., Kim, S., Cho, M., & Jeon, J. (2019). Low energy optical excitations as an indicator of structural changes initiated at the termini of amyloid proteins. *Physical Chemistry Chemical Physics*, *21*(41), 23931–23942. https://doi.org/10.1039/c9cp03764a
59. Jortner, J., Bixon, M., Langenbacher, T., & Michel-Beyerle, M. E. (1998). Charge transfer and transport in DNA. *Proceedings of the National Academy of Sciences*, *95*(22), 12759–12765. https://doi.org/10.1073/pnas.95.22.12759
60. Jun, J. V., Chenoweth, D. M., et al. (2019). A "clickable" photoconvertible small fluorescent molecule as a minimalist probe for tracking individual biomolecule complexes. *Journal of the American Chemical Society*, *141*(5), 1893–1897. https://doi.org/10.1021/jacs.8b12171
61. Kai, M., Takeda, K., Morita, T., & Kimura, S. (2008). Distance dependence of long-range electron transfer through helical peptides. *Journal of Peptide Science*, *14*(2), 192–202. https://doi.org/10.1002/psc.933
62. Karnik, A. V., & Hasan, M. (2021). *Stereochemistry: A three-dimensional insight*. Elsevier. https://doi.org/10.1016/C2019-0-05557-9

63. Karra, A. S., Stippec, S., & Cobb, M. H. (2017). Assaying protein kinase activity with radiolabeled ATP. *Journal of Visualized Experiments, 123*, e55504. https://doi.org/10.3791/55504
64. Kelly, S. M., Jess, T. J., & Price, N. C. (2005). How to study proteins by circular dichroism. *Biochimica et Biophysica Acta (BBA) - Proteins and Proteomics, 1751*(2), 119–139. https://doi.org/10.1016/j.bbapap.2005.06.005
65. Khokhlatchev, A., Xu, S., English, J., Wu, P., Schaefer, E., & Cobb, M. H. (1997). Reconstitution of mitogen-activated protein kinase phosphorylation cascades in bacteria: Efficient synthesis of active protein kinases. *Journal of Biological Chemistry, 272*(17), 11057–11062. https://doi.org/10.1074/jbc.272.17.11057
66. King, B. A., de Winter, A., McAnaney, T. B., & Boxer, S. G. (2001). Excited state energy transfer pathways in photosynthetic reaction centers: 4. Asymmetric energy transfer in the heterodimer mutant. *Journal of Physical Chemistry B, 105*(9), 1856–1862. https://doi.org/10.1021/jp0033281
67. Knowles, P. (1985). Biological spectroscopy. *Biochemical Society Transactions, 13*(3), 535–535. https://doi.org/10.1042/bst0130535
68. Konopka, M., Daly, W. H., et al. (2018). Determination of non-traditional intrinsic fluorescence (NTIF) emission sites in 1-(4-carbomethoxypyrrolidone)-PAMAM dendrimers using CNDP-based quenching studies. *Journal of Nanoparticle Research, 20*, 291. https://doi.org/10.1007/s11051-018-4437-2
69. Koudelka, T., Hoffman, P., & Carver, J. A. (2009). Dephosphorylation of αs- and β-caseins and its effect on chaperone activity: A structural and functional investigation. *Journal of Agricultural and Food Chemistry, 57*(13), 5956–5964. https://doi.org/10.1021/jf901012d
70. Kraskouskaya, D., Bancerz, M., Soor, H. S., Gardiner, J. E., & Gunning, P. T. (2014). An excimer-based, turn-on fluorescent sensor for the selective detection of diphosphorylated proteins in aqueous solution and polyacrylamide gels. *Journal of the American Chemical Society, 136*(4), 1234–1237. https://doi.org/10.1021/ja4101983
71. Krebs, M. R. H., Wilkins, D. K., Chung, E. W., Pitkeathly, M. C., Chamberlain, A. K., Zurdo, J., ... Dobson, C. M. (2000). Formation and seeding of amyloid fibrils from wild-type hen lysozyme and a peptide fragment from the β-domain. *Journal of Molecular Biology, 300*(3), 541–549. https://doi.org/10.1006/jmbi.2000.3862
72. Kumar, A., Ahari, D., Priyadarshi, A., Ansari, M. Z., & Swaminathan, R. (2020). Weak intrinsic luminescence in monomeric proteins arising from charge recombination. *The Journal of Physical Chemistry B, 124*(13), 2731–2746. https://doi.org/10.1021/acs.jpcb.0c00604
73. Kumar, A., Sharma, R., Tripathi, P., Sahu, A., Ansari, M. Z., & Swaminathan, R. (2022). Role of charged amino acids in sullying the fluorescence of tryptophan or conjugated dansyl probe in monomeric proteins. *Biochemistry, 61*(4), 339–353. https://doi.org/10.1021/acs.biochem.1c00652
74. Kumar, R., Prabhu, N. P., Yadaiah, M., & Bhuyan, A. K. (2004). Protein stiffening and entropic stabilization in the subdenaturing limit of guanidine hydrochloride. *Biophysical Journal, 87*(4), 2656–2662. https://doi.org/10.1529/biophysj.104.043752
75. Kumar, V., Sami, N., Kashav, T., Islam, A., Ahmad, F., & Hassan, M. I. (2016). Protein aggregation and neurodegenerative diseases: From theory to therapy. *European Journal of Medicinal Chemistry, 124*, 1105–1120. https://doi.org/10.1016/j.ejmech.2016.09.056
76. Ladiwala, A. R. A., Dordick, J. S., & Tessier, P. M. (2011). Aromatic small molecules remodel toxic soluble oligomers of amyloid β through three independent pathways. *Journal of Biological Chemistry, 286*(5), 3209–3218. https://doi.org/10.1074/jbc.M110.162420

77. Lakowicz, J. R. (2006). *Principles of fluorescence spectroscopy* (3rd ed., pp. 1–954). Springer. https://doi.org/10.1007/978-0-387-46312-4
78. Lakowicz, J. R. (2013). *Principles of fluorescence spectroscopy* (4th ed.). Springer Science & Business Media.
79. Lee, J., Culyba, E. K., Powers, E. T., & Kelly, J. W. (2011). Amyloid-β forms fibrils by nucleated conformational conversion of oligomers. *Nature Chemical Biology, 7*(9), 602–609. https://doi.org/10.1038/nchembio.624
80. Lindberg, D. J., Wenger, A., Sundin, E., Wesén, E., Westerlund, F., & Esbjörner, E. K. (2017). Binding of thioflavin-T to amyloid fibrils leads to fluorescence self-quenching and fibril compaction. *Biochemistry, 56*(17), 2170–2174. https://doi.org/10.1021/acs.biochem.7b00149
81. Liu, Y., Lee, J., Perez, L., Gill, A. D., Hooley, R. J., & Zhong, W. (2018). Selective sensing of phosphorylated peptides and monitoring kinase and phosphatase activity with a supramolecular tandem assay. *Journal of the American Chemical Society, 140*(42), 13869–13877. https://doi.org/10.1021/jacs.8b07554
82. Lodish, H., Berk, A., Zipursky, S. L., Matsudaira, P., Baltimore, D., & Darnell, J. (2000). *Molecular cell biology* (4th ed.). W. H. Freeman.
83. Lorient, D., & Linden, G. (1976). Dephosphorylation of bovine casein by milk alkaline phosphatase. *Journal of Dairy Research, 43*(1), 19–26. https://doi.org/10.1017/S0022029900015645
84. Lowry, O. H., Rosebrough, N. J., Farr, A. L., & Randall, R. J. (1951). Protein measurement with the Folin phenol reagent. *Journal of Biological Chemistry, 193*(1), 265–275. https://doi.org/10.1016/S0021-9258(19)52451-6
85. Maezawa, I., Hong, H.-S., Liu, R., Wu, C.-Y., Cheng, R. H., Kung, M.-P., … Jin, L.-W. (2008). Congo red and thioflavin T analogs detect Aβ oligomers. *Journal of Neurochemistry, 104*(2), 457–468. https://doi.org/10.1111/j.1471-4159.2007.04972.x
86. Mandal, I., Paul, S., & Venkatramani, R. (2018). Optical backbone-sidechain charge transfer transitions in proteins sensitive to secondary structure and modifications. *Faraday Discussions, 207*, 115–135. https://doi.org/10.1039/C8FD00043A
87. Martin, K., Steinberg, T. H., Cooley, L. A., Gee, K. R., Beechem, J. M., & Patton, W. F. (2003). Quantitative analysis of protein phosphorylation status and protein kinase activity on microarrays using a novel fluorescent phosphorylation sensor dye. *Proteomics, 3*(7), 1244–1255. https://doi.org/10.1002/pmic.200300470
88. Mishra, R., Sörgjerd, K., Nyström, S., Nordigården, A., Yu, Y.-C., & Hammarström, P. (2007). Lysozyme amyloidogenesis is accelerated by specific nicking and fragmentation but decelerated by intact protein binding and conversion. *Journal of Molecular Biology, 366*(3), 1029–1044. https://doi.org/10.1016/j.jmb.2006.11.081
89. Monti, A., D'Amico, M., D'Andrea, L., Russo, L., Salerno, D., Marasco, D., … Ruvo, M. (2021). Amyloid-like Prep1 peptides exhibit reversible blue-green-red fluorescence *in vitro* and in living cells. *Chemical Communications, 57*(30), 3720–3723. https://doi.org/10.1039/D1CC00669H
90. Mukherjee, A., Morales-Scheihing, D., Butler, P. C., & Soto, C. (2015). Type 2 diabetes as a protein misfolding disease. *Trends in Molecular Medicine, 21*(7), 439–449. https://doi.org/10.1016/j.molmed.2015.04.005
91. Mukherjee, A., & Soto, C. (2017). Prion-like protein aggregates and type 2 diabetes. *Cold Spring Harbor Perspectives in Medicine, 7*(3), a024315. https://doi.org/10.1101/cshperspect.a024315
92. Nandi, T., Desai, A., & Ainavarapu, S. R. M. (2020). The unfolding transition state of ubiquitin with charged residues has higher energy than that with hydrophobic residues. *Physical Chemistry Chemical Physics, 22*, 23158–23168. https://doi.org/10.1039/D0CP04208A

93. Nidhisha, V., Gopal, R., Chitthrambattu, A., & Neeroli, R. N. K. (2024). p-Phenylenediamine derived carbon nanodots for probing solvent interactions. *Nanoscale Advances, 6*, 1535–1547. https://doi.org/10.1039/D3NA00845K
94. Nilsson, M. R. (2004). Techniques to study amyloid fibril formation in vitro. *Methods, 34*(1), 151–160. https://doi.org/10.1016/j.ymeth.2004.03.008
95. Niyangoda, C., Miti, T., Breydo, L., Uversky, V., & Muschol, M. (2017). Carbonyl-based blue autofluorescence of proteins and amino acids. *PLOS ONE, 12*(3), e0176983. https://doi.org/10.1371/journal.pone.0176983
96. Olzscha, H., Schermann, S. M., Woerner, A. C., Pinkert, S., Hecht, M. H., et al. (2011). Amyloid-like aggregates sequester numerous metastable proteins with essential cellular functions. *Cell, 144*(1), 67–78. https://doi.org/10.1016/j.cell.2010.11.050
97. Otey, M. C., & Greenstein, J. P. (1954). Studies on polycysteine peptides and proteins. II. Apparent dissociation constants, and ultraviolet and infrared absorption spectra of isomeric cystinylcystine peptides. *Archives of Biochemistry and Biophysics, 53*(3), 501–513. https://doi.org/10.1016/0003-9861(54)90372-8
98. Pagba, C. V., et al. (2015). A tyrosine-tryptophan dyad and radical-based charge transfer in a ribonucleotide reductase-inspired maquette. *Nature Communications, 6*, 10010. https://doi.org/10.1038/ncomms10010
99. Pansieri, J., et al. (2019). Ultraviolet–visible–near-infrared optical properties of amyloid fibrils shed light on amyloidogenesis. *Nature Photonics, 13*(7), 473–479. https://doi.org/10.1038/s41566-019-0430-6
100. Pavia, D. L., Lampman, G. M., Kriz, G. S., & Vyvyan, J. R. (2009). Infrared spectroscopy. In Introduction to spectroscopy (pp. 15–30). Cengage Learning.
101. Pawson, T., Gish, G. D., & Nash, P. (2001). SH2 domains, interaction modules and cellular wiring. Trends in Cell Biology, 11(12), 504–511. https://doi.org/10.1016/S0962-8924(01)02173-6
102. Pawson, T., & Scott, J. D. (2005). Protein phosphorylation in signalling: 50 years and counting. Trends in Biochemical Sciences, 30(6), 286–290. https://doi.org/10.1016/j.tibs.2005.04.013
103. Pedersen, J. T., & Heegaard, N. H. H. (2013). Analysis of protein aggregation in neurodegenerative disease. Analytical Chemistry, 85(9), 4215–4227. https://doi.org/10.1021/ac400689x
104. Pinotsi, D., Grisanti, L., Mahou, P., Gebauer, R., Kaminski, C. F., et al. (2016). Proton transfer and structure-specific fluorescence in hydrogen bond-rich protein structures. Journal of the American Chemical Society, 138(9), 3046–3057. https://doi.org/10.1021/jacs.5b11080
105. Plaxco, K. W., & Dobson, C. M. (1996). Time-resolved biophysical methods in the study of protein folding. Current Opinion in Structural Biology, 6(5), 630–636. https://doi.org/10.1016/S0959-440X(96)80078-7
106. Polo, F., Antonello, S., Formaggio, F., Toniolo, C., & Maran, F. (2005). Evidence against the hopping mechanism as an important electron transfer pathway for conformationally constrained oligopeptides. Journal of the American Chemical Society, 127(2), 492–493. https://doi.org/10.1021/ja043621f
107. Prakash, S., & Matouschek, A. (2004). Protein unfolding in the cell. Trends in Biochemical Sciences, 29(12), 593–600. https://doi.org/10.1016/j.tibs.2004.09.003
108. Prasad, S., et al. (2017). Near UV-visible electronic absorption originating from charged amino acids in a monomeric protein. Chemical Science, 8, 5416–5433. https://doi.org/10.1039/C7SC00392A
109. Priyadarshi, A., Devi, H. M., & Swaminathan, R. (2023). Disruption of spatial proximities among charged groups in equilibrium-denatured states of proteins tracked using protein charge transfer spectra. Biochemistry, 62(11), 1643–1658. https://doi.org/10.1021/acs.biochem.3c00012

110. Priyadarshi, A., Saikia, S. B., & Swaminathan, R. (2024). Monitoring binding of protamine with DNA using protein charge transfer spectra. The Journal of Physical Chemistry B, 128(40), 9656–9668. https://doi.org/10.1021/acs.jpcb.4c05020
111. Quickenden, T. I., & Irvin, J. A. (1979). The ultraviolet absorption spectrum of liquid water. Journal of Chemical Physics, 72(10), 4416–4428. https://doi.org/10.1063/1.438420
112. Ravi, V. K., Goel, M., Kotamarthi, H. C., Ainavarapu, S. R. K., & Swaminathan, R. (2014a). Preventing disulfide bond formation weakens non-covalent forces among lysozyme aggregates. PLOS ONE, 9(4), e87012. https://doi.org/10.1371/journal.pone.0087012
113. Ravi, V. K., Swain, T., Chandra, N., & Swaminathan, R. (2014b). On the characterization of intermediates in the isodesmic aggregation pathway of hen lysozyme at alkaline pH. PLOS ONE, 9(4), e87256. https://doi.org/10.1371/journal.pone.0087256
114. Rischel, C., & Poulsen, F. M. (1995). Modification of a specific tyrosine enables tracing of the end-to-end distance during apomyoglobin folding. FEBS Letters, 374(1), 105–109. https://doi.org/10.1016/0014-5793(95)01038-1
115. Ross, C. A., & Poirier, M. A. (2005). What is the role of protein aggregation in neurodegeneration? Nature Reviews Molecular Cell Biology, 6(11), 891–898. https://doi.org/10.1038/nrm1741
116. Rothman, D. M., Shults, M. D., & Imperiali, B. (2005). Chemical approaches for investigating phosphorylation in signal transduction networks. Trends in Cell Biology, 15(10), 502–510. https://doi.org/10.1016/j.tcb.2005.07.004
117. Ryzhkina, I. S., et al. (2018). Self-organization and properties of dispersed systems based on dilute aqueous solutions of (S)- and (R)-lysine. Mendeleev Communications, 28(1), 66–69. https://doi.org/10.1016/j.mencom.2018.01.004
118. Sakamoto, T., Ojida, A., & Hamachi, I. (2009). Molecular recognition, fluorescence sensing, and biological assay of phosphate anion derivatives using artificial Zn(II)-Dpa complexes. Chemical Communications, 141–152. https://doi.org/10.1039/B812951C
119. Schweizer, T., Kubach, H., & Koch, T. (2021). Investigations to characterize the interactions of light radiation, engine operating media and fluorescence tracers for the use of qualitative light-induced fluorescence in engine systems. Automotive Engine Technology, 6, 275–287.
120. Serdyuk, I. N., Zaccai, N. R., & Zaccai, J. (2007). Methods in molecular biophysics. Cambridge University Press. https://doi.org/10.1017/CBO9780511811166
121. Serrano, A. L., Waegele, M. M., & Gai, F. (2012). Spectroscopic studies of protein folding: Linear and nonlinear methods. Protein Science, 21(2), 157–170. https://doi.org/10.1002/pro.751
122. Shahmoradian, S. H., et al. (2019). Lewy pathology in Parkinson's disease consists of crowded organelles and lipid membranes. Nature Neuroscience, 22(7), 1099–1109.
123. Shukla, A., et al. (2004). A novel UV laser-induced visible blue radiation from protein crystals and aggregates: Scattering artifacts or fluorescence transitions of peptide electrons delocalized through hydrogen bonding? *Archives of Biochemistry and Biophysics*, *428*(2), 144–153. https://doi.org/10.1016/j.abb.2004.07.019
124. Sophianopoulos, A. J., & Van Holde, K. E. (1961). Evidence for dimerization of lysozyme in alkaline solution. *Journal of Biological Chemistry*, *236*(11), PC82–PC83.
125. Sophianopoulos, A. J., & Van Holde, K. E. (1964). Physical studies of muramidase (lysozyme): II. pH-dependent dimerization. *Journal of Biological Chemistry*, *239*(7), 2516–2524.

126. Spillantini, M. G., et al. (1997). α-Synuclein in Lewy bodies. *Nature*, *388*(6645), 839–840. https://doi.org/10.1038/42166
127. Stephens, A. D., et al. (2020). Intrinsic fluorescence in non-aromatic peptide structures is induced by collective vibrations, charge reorganisation and short hydrogen bonds, as shown in a new glutamine-related structure. *bioRxiv*. https://doi.org/10.1101/2020.01.01.000000
128. Swaminathan, R., Krishnamoorthy, G., & Periasamy, N. (1994a). Similarity of fluorescence lifetime distributions for single tryptophan proteins in the random coil state. *Biophysical Journal*, *67*(6), 2013–2023. https://doi.org/10.1016/S0006-3495(94)80777-5
129. Swaminathan, R., Ravi, V. K., Kumar, S., Kumar, M. V. S., & Chandra, N. (2011). Lysozyme: A model protein for amyloid research. In R. Donev (Ed.), *Advances in Protein Chemistry and Structural Biology* (pp. 63–111). Academic Press.
130. Tang, Z., Chen, H., He, H., & Ma, C. (2019). Assays for alkaline phosphatase activity: Progress and prospects. *TrAC Trends in Analytical Chemistry*, *113*, 32–43. https://doi.org/10.1016/j.trac.2019.01.019
131. Tarrant, M. K., & Cole, P. A. (2009). The chemical biology of protein phosphorylation. *Annual Review of Biochemistry*, *78*(1), 797–825. https://doi.org/10.1146/annurev.biochem.78.070907.103047
132. Teilum, K., Maki, K., Kragelund, B. B., Poulsen, F. M., & Roder, H. (2002). Early kinetic intermediate in the folding of acyl-CoA binding protein detected by fluorescence labeling and ultrarapid mixing. *Proceedings of the National Academy of Sciences of the United States of America*, *99*(15), 9807–9812. https://doi.org/10.1073/pnas.152319399
133. Tikhonova, T. N., et al. (2018). Dissection of the deep-blue autofluorescence changes accompanying amyloid fibrillation. *Archives of Biochemistry and Biophysics*, *651*, 13–20. https://doi.org/10.1016/j.abb.2018.01.002
134. Tommos, C., Valentine, K. G., Martínez-Rivera, M. C., Liang, L., & Moorman, V. R. (2013). Reversible phenol oxidation and reduction in the structurally well-defined 2-mercaptophenol-α3C protein. *Biochemistry*, *52*(8), 1409–1418. https://doi.org/10.1021/bi301641w
135. Tremblay, M. S., Lee, M., & Sames, D. (2008). A luminescent sensor for tyrosine phosphorylation. *Organic Letters*, *10*(1), 5–8. https://doi.org/10.1021/ol702540t
136. Tsai, C.-F., Wang, Y.-T., Lin, P.-Y., & Chen, Y.-J. (2011). Phosphoproteomics by highly selective IMAC protocol. In K. W. Li (Ed.), *Neuroproteomics* (Vol. 57, pp. 181–196). Humana Press. https://doi.org/10.1007/978-1-60761-836-6_11
137. Wall, J., Murphy, C. L., & Solomon, A. (1999). In vitro immunoglobulin light chain fibrillogenesis. In *Methods in Enzymology* (Vol. 309, pp. 204–217). Academic Press. https://doi.org/10.1016/S0076- 6879(99)09014-4
138. Wei, L., & Ploss, A. (2021). Mechanism of hepatitis B virus cccDNA formation. *Viruses*, *13*(8), 1463. https://doi.org/10.3390/v13081463
139. Wetlaufer, D. B. (1963). Ultraviolet spectra of proteins and amino acids. *Advances in Protein Chemistry*, *17*, 301–390. https://doi.org/10.1016/S0065-3233(08)60391-5
140. Zaccai, N. R., Serdyuk, I. N., & Zaccai, J. (2017). *Methods in molecular biophysics: Structure, dynamics, function for biology and medicine*. Cambridge University Press. https://doi.org/10.1017/9781316673950
141. Ziaunys, M., Sneideris, T., & Smirnovas, V. (2019). Exploring the potential of deep-blue autofluorescence for monitoring amyloid fibril formation and dissociation. *PeerJ*, *7*, e6524. https://doi.org/10.7717/peerj.6524